First measurement of ϕ meson production in 30 GeV proton-nucleus reactions via di-electron decay at J-PARC

Satomi Nakasuga

Abstract

The first result of the ϕ-meson production cross section in 30 GeV proton–nucleus collisions is reported. The measurement was carried out using the newly constructed high-momentum beamline at the J-PARC Hadron Experimental Facility in 2020. The ϕ mesons were detected through the di-electron decay channel with the E16 spectrometer, which is dedicated to dielectron measurement for the J-PARC E16 experiment, the first program on the high-momentum beamline. As nuclear targets, carbon and copper were employed.

30 GeV proton-nucleus collisions corresponds to a nucleon–nucleon center-of-mass energy of $\sqrt{s} = 7.7$ GeV. This energy region has recently attracted interest in the heavy-ion community for studies of QCD phase structure at intermediate temperature and high baryon density. In particular, several experimental indications of enhanced strangeness production have been observed in this energy region, and various theoretical interpretations are actively being discussed. The ϕ meson is composed of an almost pure $\bar{s}s$ state. Since strange quarks are not present in the initial state in proton-nucleus system as valence quarks, ϕ mesons can be produced mainly through $s\bar{s}$ pair creation from the vacuum in fragmentation processes. This implies that ϕ-meson production may be sensitive to the $s\bar{s}$ pair production rate. Measuring the production cross section is therefore essential as a basis for understanding the ϕ-meson production mechanism, and it may further provide information on possible strangeness enhancement.

In the present study, the dielectron decay of the ϕ meson was successfully detected using the newly installed spectrometer, as demonstrated by a significance of $S/\sqrt{B} = 4.4$ after combining all experimental targets. This achievement establishes the technique for measuring di-electron decays of vector mesons in 30 GeV proton–nucleus collisions at J-PARC. From the obtained mass spectra, the yields were evaluated to be 11.9 $\pm$ 5.6 (stat.) $\pm$ 5.2 (syst.) ϕ mesons for the carbon target and 23.6 $\pm$ 10.2 (stat.) $\pm$ 8.5 (syst.) for the copper target. These yields were converted to total production cross sections assuming the kinematic distributions predicted by the event generator JAM. The estimated total cross sections are 2.0 $\pm$ 0.9 (stat.) $\pm$ 1.0 (syst.) mb for carbon and 10.3 $\pm$ 4.4 (stat.) $\pm$ 4.4 (syst.) mb for copper.

These results were examined through the α parametrization, defined as $\sigma \propto A^{\alpha}$, resulting in $\alpha = 0.99 \pm 0.38$ (stat.) $\pm$ 0.34 (syst.). The extrapolation of this result to $A = 1$, i.e., to proton–proton reactions, is in good agreement with results from other experiments at comparable energies, suggesting that the proton–nucleus production cross section follows a scaling of the proton–proton cross section. The result of $\alpha \sim 1$ supports a picture in which ϕ mesons are produced uniformly within the nucleus and are detected with little absorption.

The estimated total cross sections were compared with the values suggested by JAM, which gives 1.08 mb for carbon and 6.75 mb for copper. The results agree within uncertainties, supporting the production mechanism based on string fragmentation implemented in JAM. However, the experimental values tend to be systematically larger, and more detailed measurements are therefore anticipated. The present study was conducted using the pilot data of the J-PARC E16 experiment. With the upcoming physics runs, the statistics for ϕ mesons are expected to increase significantly. Importantly, the capability established in the present study to determine the production cross section provides new opportunities for studies of strangeness production at intermediate energies.

Contents

List of Tables

List of Figures

Chapter 1

Introduction

1.1 Overview

The strong interaction, one of the four fundamental interactions in nature, plays a pivotal role in forming hadrons from quarks and gluons, and for forming nuclei from nucleons. As a feature of Quantum Chromodynamics (QCD), the theory of the strong interaction, the running coupling constant leads to asymptotic freedom, in which the strength of the interaction depends on the energy scale. As a consequence, the strong interaction cannot operate over long distances, quarks become "confined," and hadrons are formed. In other words, although hadrons have an internal structure, their constituent quarks cannot be extracted as free particles; thus, we can normally observe only the degrees of freedom of the hadrons. On the other hand, in extreme environments such as high-density systems where hadrons overlap, or high-temperature systems filled with excited hadrons, the degrees of freedom of quarks and gluons are expected to dominate. In the high-temperature case, the realized phase is known as the quark-gluon plasma (QGP), whereas in high-density environments, possible phases such as "Quarkyonic Matter," "Color Superconductivity," and related states may emerge. High-temperature phases have been investigated experimentally through relativistic heavy-ion collisions, and the emergence of the quark-gluon plasma was suggested in the high-energy heavy-ion collisions conducted at RHIC in the 2000s. At present, both experimental and theoretical efforts increasingly focus on high-density systems, which are difficult to calculate even with lattice QCD, the first-principles approach to QCD.

Studies of hadrons in such extreme phases also deepen our understanding of hadrons in the low-energy hadronic phase. The masses of hadrons, which are many-body systems of quarks, are known to be far larger than the sum of the bare quark masses. The theory of the strong interaction has an approximate chiral symmetry, but this symmetry is considered to be spontaneously broken in the vacuum. The masses of hadrons (excited states of this vacuum) are thought to be generated dynamically as a consequence of nontrivial vacuum structure. The spontaneous breaking of chiral symmetry in the vacuum corresponds to the fact that the quark condensate $\langle \bar{q}q \rangle$, the order parameter of the symmetry, acquires a nonzero vacuum expectation value. The condensate $\langle \bar{q}q \rangle$ is expected to decrease at high temperature and/or high density, implying that the symmetry broken in the vacuum is restored under such extreme phases [1]. Therefore, exploring extreme phases is also essential for understanding the spontaneous breaking of chiral symmetry and its restoration.

In this study, the production cross section of ϕ mesons in 30 GeV proton-nucleus collisions was measured for the first time. The production of ϕ mesons from nucleons and nuclei has been studied for various motivations. In recent years, heavy-ion collisions at intermediate energies around 30 GeV (corresponding to a center-of-mass energy of $\sqrt{s} = 7.7$ GeV) have been actively explored due to an interest in high-density QCD matter. At high energies, where

scatterings involve large momentum transfer, the running coupling constant becomes small, and the reactions can be described within perturbative QCD (pQCD). In contrast, in the recently active intermediate-energy region, non-perturbative contributions cannot be ignored. Since the energy range where pQCD is applicable is not obvious, experimental input becomes essential.

Strangeness production in heavy-ion collisions has traditionally been considered a signal of QGP formation [2]. During the QGP searches in the 2000s, several expected and unexpected signals related to strangeness production were observed in intermediate-energy heavy-ion collision experiments: the NA49 collaboration at CERN-SPS measured the energy dependence of hadron production and observed an increase in the K^+/π^+ ratio around $\sqrt{s} = 7.7$ GeV [3, 4]. The HADES [5] collaboration at GSI observed a strong enhancement of the ϕ/K^- ratio below the ϕ production threshold around $\sqrt{s} \sim 4$ GeV. Recent STAR BES-II results at BNL-RHIC also report an enhancement of the Ω/ϕ ratio for $\sqrt{s} \geq 7.7$ GeV [6]. Regarding ϕ-meson production, the NA49 Collaboration observed an unexpectedly broad rapidity distribution [7], and further measurements with different systems have been reported in recent years [8, 9]. These strange-hadron signals in heavy-ion collisions are often discussed in comparison with proton-proton collisions, but proton-nucleus collisions have not been included in recent programs and may provide unique and valuable reference information. In addition, various theoretical interpretations of the strangeness enhancement have been proposed. Ref. [10] accounts for the strangeness enhancement by introducing a reduction of the constituent-quark masses associated with chiral-symmetry restoration in medium. In this context, measurement of proton–nucleus collisions may provide a useful probe of normal nuclear density.

A ϕ meson produced in proton-nucleus collisions is expected to interact with the nuclear medium before its decay. Because the ϕ meson and nucleons do not share valence quark flavors, their interaction is considered to be dominated by gluon exchange, which is suppressed by the OZI rule. Thus, the ϕ-nucleon interaction is expected to be weak, and the small scattering length derived from the differential cross section of ϕ photoproduction based on the VMD model supports this. However, results from the COSY-ANKE collaboration for ϕ production in 2.83 GeV proton-nucleus collisions suggest strong absorption of ϕ mesons in the nuclear medium (transparency ratio $\sim$0.5) [11]. Measurements of π-A reactions at 1.65 GeV by the HADES collaboration indicate absorption of ϕ mesons comparable to that of K^- mesons [12]. Because the ϕ meson has an extremely short lifetime, direct scattering experiments with nucleons are difficult, but recent femtoscopy approaches have been applied; measurements of final-state interactions between ϕ mesons and protons produced in high-energy proton-proton reactions suggest an attractive p-ϕ interaction [13]. Thus, the interaction between ϕ mesons and nucleons (or nuclear medium) is currently unsettled and actively studied. It is fundamentally difficult to disentangle production and absorption effects from experimental results. While the measured cross sections may contain valuable information on the unresolved ϕ-N interaction, one must carefully account for such hadronic interactions when studying the genuine production mechanism. To this end, measurement of the mass number dependence is expected to be informative.

This study was conducted using, for the first time, the newly constructed high-momentum beamline at J-PARC and the J-PARC E16 spectrometer specialized for di-electron measurements. As the first program on this beamline, the J-PARC E16 experiment has already launched, aiming to investigate the medium mass modification of the ϕ mesons with higher statistics and higher mass resolution than the precedent experiment. The present study uses pilot data from the E16 experiment. For the E16 experiment, which requires large statistics, evaluating the production cross section serves as an important benchmark for estimating future yields. In addition, as a complementary study of the E16, the J-PARC E88/SAΦRE experiment is planned to measure the K^+K^- decay branch of the ϕ meson, sharing part of the experimen-

tal setup with E16. In the future, measurements of hadronic decays will also become possible, providing additional ways to explore the QCD-matter observables discussed above.

The high-momentum beamline transports a portion of the proton beam extracted from the Main Ring of J-PARC to the Hadron Experimental Facility and directly irradiates the experimental target. In the future, there are plans to introduce a production target into the high-momentum beamline and operate it as a secondary beamline (the π-20 beamline), enabling the use of various secondary beams up to 20 GeV/c. While the existing secondary beamlines at J-PARC are limited to momenta of up to 2 GeV/c, secondary-beam operation of the high-momentum beamline will enable access to much higher-momentum beams. This capability allows spectroscopy of hadrons containing heavier quarks and of highly excited states, providing a means to study di-quark correlations inside hadrons. As a first experiment using the secondary beam, the J-PARC E95 experiment is planned, which will measure the differential cross section of ϕ production from π^--p reactions using the phase-1 of the secondary beamline. One of its objectives is the search for possible N^* states, and it will also advance understanding of the ϕ-N interaction.

In the long term, the J-PARC HI project has been proposed, in which heavy ions are accelerated in the J-PARC accelerators and extracted to the high-momentum beamline. Dilepton spectra are particularly useful as probes of thermal emission of virtual photons, providing the advantage of monitoring virtual photons emitted from each stage of the complex space-time evolution of intermediate-energy heavy-ion collisions. As Phase 1, dilepton measurements using a modified E16 spectrometer are planned, and establishing dilepton-measurement techniques through the present study is an important first step toward future programs. In addition, information on beam-related backgrounds and time structure of the beam obtained here will contribute to future beam operations.

In summary, the present study has two major implications. First, it derives for the first time the production cross section of the ϕ meson in 30-GeV proton-nucleus reactions, providing valuable input for models essential to understanding QCD physics in the intermediate-energy region, which has attracted considerable attention in recent years, as well as serving as a reference for heavy-ion collisions. Second, it establishes dilepton-measurement techniques using the newly constructed beamline and spectrometer at J-PARC, providing the direct and indirect information on the feasibility of various experiments planned for the future. The following sections of this chapter is organized as follows: Section 1.2 summarizes basic concepts related to the strong interaction. Section 1.3 discusses the production mechanisms of ϕ mesons in intermediate-energy collisions. Possible processes are reviewed, with particular reference to their treatment in event generator JAM [14], the hadronic cascade model used in this study. Section 1.4 introduces future experiments planned for the J-PARC high-momentum beamline. Finally, Section 1.5 outlines the overall structure of this thesis.

1.2 QCD Foundations

In this section, we briefly review the background knowledge related to the strong interaction.

1.2.1 QCD Lagrangian

Quantum chromodynamics (QCD), the theory that describes the strong interaction, is a gauge theory with an SU(3) symmetry associated with color charge. The dynamics of quarks and gluons, the particles that participate in the strong interaction, are described by the following

Lagrangian:

$$\mathcal{L} = \sum_q \bar{\psi}_{q,a}(i\gamma^\mu \partial_\mu \delta_{ab} - g_s \gamma^\mu t^C_{ab} \mathcal{A}^C_\mu - m_q \delta_{ab})\psi_{q,b} - \frac{1}{4} F^A_{\mu\nu} F^{\mu\nu}_A. \tag{1.1}$$

Here, ψ_q denotes the quark field, m_q the quark mass, $\mathcal{A}_\mu$ the gluon field, and g_s the coupling constant. The subscript q labels the quark flavor. t^C_{ab} are the generators of the SU(3) group and are given by $t^C_{ab} = \lambda^C/2$, where λ^C are the Gell-Mann matrices. The index C runs from 1 to $N_c^2 - 1 = 8$ for $N_c = 3$. The field tensor $F^A_{\mu\nu}$ is defined as follows:

$$F^A_{\mu\nu} = \partial_\mu \mathcal{A}^A_\nu - \partial_\nu \mathcal{A}^A_\mu - g_s f_{ABC} \mathcal{A}^B_\mu \mathcal{A}^C_\nu. \tag{1.2}$$

Here, f_{ABC} are the structure constants of the SU(3) group, which satisfy the commutation relation $[t^A, t^B] = i f_{ABC} t^C$.

In Eq. 1.1, the first term represents the kinetic term of free quarks, the second term describes the quark-gluon interaction, and the third term corresponds to the mass term. Furthermore, the third term in Eq. 1.2 gives rise to gluon self-interactions.

To solve such a Lagrangian approximately, one performs perturbative calculations in which the interaction terms are treated as perturbations. The results of perturbation calculation are expanded in powers of the coupling constant g_s. The problems of ultraviolet divergences are handled by renormalizing physical quantities such as masses, coupling constants, and field normalization factors. Through this procedure, the coupling $\alpha_s = g_s^2/4\pi$ acquires a dependence on the renormalization scale μ_R. Although the renormalization scale μ_R can be chosen arbitrarily, it is typically taken to be the characteristic momentum scale Q^2 of the process. Consequently, as shown in the following expression, the coupling α_s varies with the momentum transfer and is therefore referred to as the "running coupling constant."

$$\alpha_s(Q^2) \propto \frac{4\pi}{\ln(Q^2/\Lambda^2)} \tag{1.3}$$

Reactions with larger momentum transfer correspond to smaller values of the coupling constant, meaning that the interaction becomes weaker. This property is known as "asymptotic freedom." As shown in Fig. 1.1, asymptotic freedom has been quantitatively confirmed by many experimental evaluations.

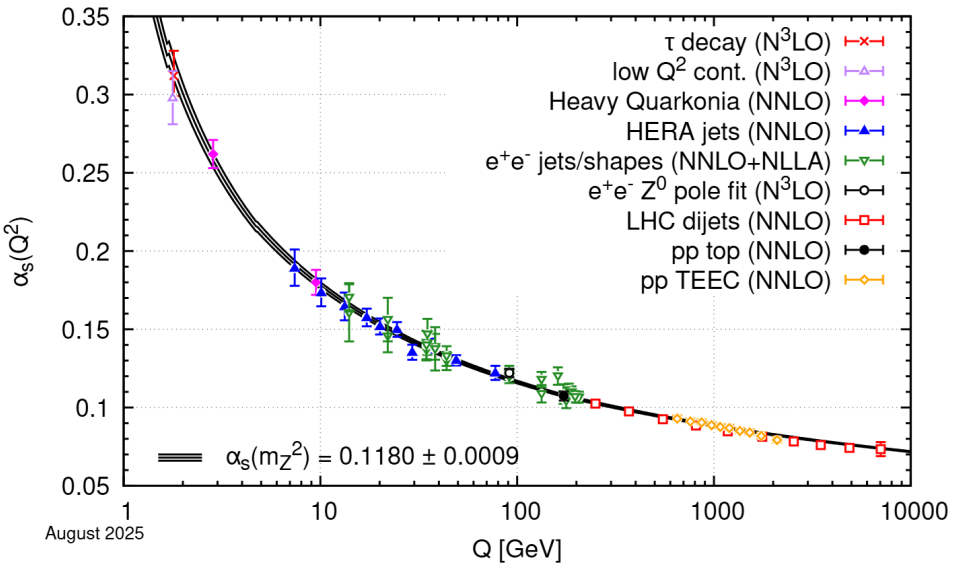

Figure 1.1: Running coupling constant of QCD. [15]

In general, reactions with typical energy scales sufficiently above $\Lambda_{\mathrm{QCD}} \sim 200\ \mathrm{MeV}/c^2$ can be treated perturbatively, whereas the low-energy, non-perturbative regime is difficult to handle. In such regions, phenomenological models and lattice-QCD simulations play an essential role.

1.2.2 Quark-antiquark Potential

Figure 1.2 shows the static quark-antiquark potential calculated using lattice QCD in Ref. [16]. The red solid curve represents the result of fitting the calculation with the following functional

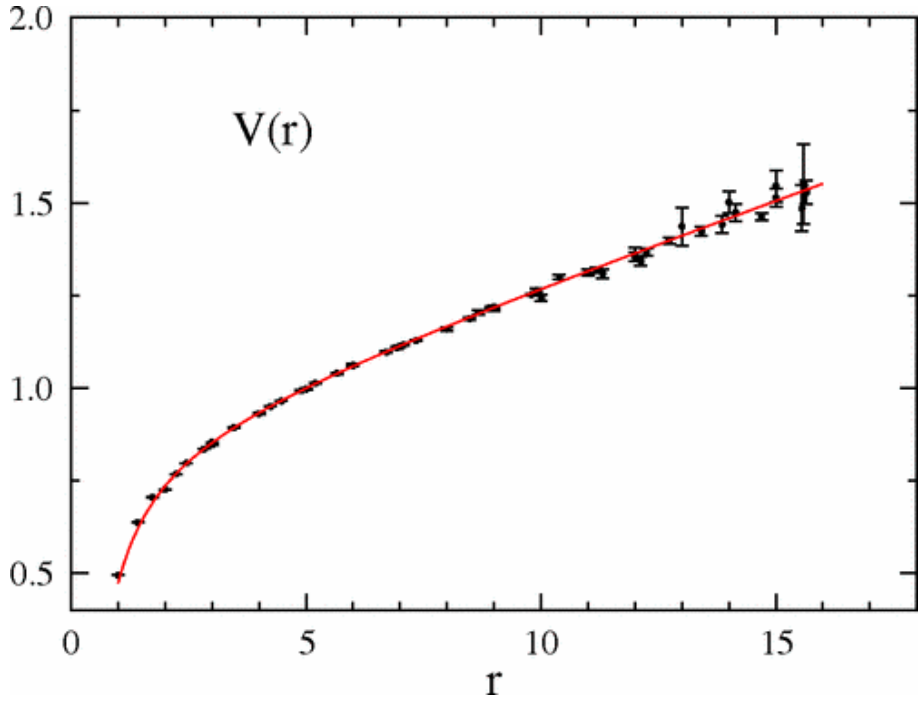

Figure 1.2: Static quark-antiquark potential calculated from lattice QCD [16].

form:

$$V(r) = V_0 - \frac{a}{r} + Kr. \tag{1.4}$$

Here, V_0, a, and K are fitting parameters. The fit successfully describes the lattice results, demonstrating that in QCD the quark-antiquark potential behaves as $\propto 1/r$ at short distances and $\propto r$ at long distances. Since an infinite amount of energy is required to separate quarks to an infinite distance ($r \to \infty$), quarks cannot be isolated; in other words, they are confined. K in Eq. 1.4 means the string tension representing the strength of the quark confinement force.

Experimentally, the quark-antiquark potential in QCD is extracted from the excitation spectra of charmonium and bottomonium. Given the function in Eq. 1.4, the parameters can be quantitatively determined from fitting, and the string tension K is obtained as

$$K \simeq (0.42\ \mathrm{GeV})^2 = 0.9\ \mathrm{GeV/fm} \tag{1.5}$$

as reported in Ref. [17].

1.2.3 String Fragmentation

When the distance between a quark and an antiquark increases, the string breaks and particle–antiparticle pairs are created. This mechanism is described in analogy with the Schwinger

mechanism. The pair-creation rate in a string with tension K is given by

$$P(q\bar{q}) \propto \exp\left(-\pi \frac{{m_q}^2}{2K}\right) \tag{1.6}$$

where m_q is the constituent quark mass [18]. Because the pair-creation rate depends on the mass of the produced quark, strange quarks and light quarks (u, d) are produced with different probabilities, as expressed by

$$\frac{P(s\bar{s})}{P(u\bar{u})} = \frac{P(s\bar{s})}{P(d\bar{d})} = \gamma_s = \exp\left(-\pi \frac{{m_s}^2 - {m_{u,d}}^2}{2K}\right) \tag{1.7}$$

Here, γ_s is called the strangeness suppression factor. Using constituent quark masses $m_u \approx 0.35$ GeV and $m_s \approx 0.5$ GeV, one obtains $\gamma_s \approx 0.3$. This mechanism is implemented in the Lund string model [18], which is widely used in currently active simulations of hadron production at intermediate and high energies. On the other hand, it has been suggested that $\gamma_s \sim 0.4$ is more suitable for reproducing strange hadron production at intermediate energies such as those at BNL-AGS[19], and the underlying physical picture remains under discussion.

1.3 Strangeness Production

1.3.1 Reaction Mechanisms in Different Energy Regimes

In general, the reaction picture of the protons or nuclei collisions depends on the collision energy, because the relevant degrees of freedom and effective coupling strengths vary with the energy scale. At high-energies, scattering with large momentum transfer probes finer structures of the nucleon, requiring the contributions of partons other than valence quarks to be taken into account. Although the number and types of particles involved in the reaction increase, the interactions themselves become simpler and can be treated within perturbative QCD. In contrast, in the low-energy regime, hadronic degrees of freedom become relevant, but the interactions themselves become complicated due to non-perturbative QCD effects.

To extract a physical picture from the experimental results, simulation approaches that implement the microscopic reaction process, constructed to reproduce the data phenomenologically, are instrumental. In the present study, we employ the simulation code JAM [14], which has been developed to cover a wide energy range from low-energy hadronic interactions up to relativistic high-energy collisions. In the following, we review the expected reaction mechanisms from low to high energies, comparing them with the implementations in JAM.

Low-energy regime

We begin with low-energy collisions, where hadronic degrees of freedom become dominant. In JAM, resonance production is considered for a nucleon-nucleon center-of-mass energy $\sqrt{s} < 4$ GeV. Hadron production in this region arises from inelastic hadron-hadron scatterings that form resonance states (and their subsequent decays), constituent-quark exchange processes, and annihilation channels. The s-channel resonances are produced according to the Breit-Wigner formula

$$\sigma(E) = \frac{\pi(\hbar c)^2}{p_{CM}^2} \cdot \frac{(2s_R + 1)}{(2s_i + 1)(2s_f + 1)} \cdot \frac{\Gamma_i \Gamma_f}{(E - E_0)^2 + \Gamma_{tot}^2/4} \tag{1.8}$$

where E_0 is the resonance energy, s_i and s_f are the spins of the initial and final states, and s_R is the spin of the resonance. Although the primary reaction at 30 GeV is expected to follow the string mechanism described below, secondary hadron production in this low-energy region may occur through hadronic scatterings.

Transition to higher energies

In the region $\sqrt{s} > 4$–5 GeV, the resonance picture breaks down because the resonance widths become large and the discrete levels begin to overlap. In such an energy region, processes in which partons undergo "soft" scatterings with small momentum transfer are taken into account. In JAM, this process is implemented as "soft string excitation": An excited string stretched between valence quarks (quark and diquark for baryons, quark and antiquark for mesons) undergoes fragmentation according to the Lund string model (see Sec. 1.2.3), producing hadrons. In JAM, this string process is applied in the range $4 < \sqrt{s} < 50$ GeV. The collision energy of the present study corresponds to $\sqrt{s} = 7.7$ GeV, therefore, this process is applicable to the first collision in the reactions studied here.

High-energy regime

In the relativistic high-energy collisions, it is a reasonable picture that quarks and gluons confined inside nucleons behave almost freely, according to QCD asymptotic freedom. The free partons, distributed according to parton distribution functions, interact through elementary processes calculated in perturbative QCD under impulse approximation, and hadronize via string fragmentation and are ultimately observed as hadrons. It successfully describes, in particular, the high-p_T hadron production spectra in high-energy proton-proton collisions [20]. However, as the energy decreases, the pQCD calculation of elementary scatterings becomes invalid. Indeed, the transverse-momentum spectra in the low-p_T region ($p_T <\sim 1$ GeV/c) of hadron production deviate from the power-law behavior predicted by pQCD, as confirmed by data. Although the lower limit of pQCD applicability is not known, model calculation incorporate phenomenologically determined thresholds to reproduce various experimental results. In JAM, minijet production from hard parton-parton scattering is included when the center-of-mass energy of the two-body system exceeds $\sqrt{s} > 10$ GeV.

The energy of $\sqrt{s} = 7.7$ GeV is near the lower boundary of pQCD applicability, where different models adopt different physical pictures. Although distinguishing between different physical pictures is difficult, experimental inputs provide essential information for understanding the hadron-production mechanisms in this energy region. In particular, testing whether perturbative descriptions remain valid at J-PARC energies may offer important guidance for future physics programs.

ϕ-meson production in intermediate energies

The ϕ meson is a nearly pure $s\bar{s}$ state, and due to the OZI rule, its production is naively expected to be sensitive to s-quark production. Since nucleons and nuclei do not contain valence s quarks, their production mechanisms include contributions from sea quarks, pair creation from the vacuum, and weak decays of heavier flavors. Respecting the phenomenological pQCD applicability threshold of $\sqrt{s} \sim 10$ GeV in JAM, the contribution from sea quarks is expected to be small at the present energy ($\sqrt{s} = 7.7$ GeV). Thus, ϕ production is considered to be dominated by $s\bar{s}$ creation via string breaking. As discussed in Sec. 1.2.3, the $s\bar{s}$ production fraction still carries uncertainties, making the measurement of ϕ-meson production an important input. In JAM, string fragmentation is implemented based on the PYTHIA [21], and a strangeness suppression factor of $\gamma_s = 0.3$ is employed.

1.3.2 Observed Strangeness Enhancement and Theoretical Interpretations

As introduced in Sec. 1.1, the behavior in which the yield of strange hadrons increases relative to that of hadrons composed of u and d quarks in the intermediate-energy heavy-ion collisions has been confirmed across several observables. The CERN-SPS NA49 experiment measured the production of charged pions and kaons in central Pb+Pb collisions at 20, 30, 40, 80, and 158 GeV [3, 4]. As a result, particularly in the K^+/π^+ ratio, a "horn" structure was observed around 30 GeV, as shown in Fig. 1.3, indicating that the production of hadrons containing $\bar{s}$ quarks exceeds that of hadrons composed of light quarks. NA49 interpreted this energy dependence observed in heavy-ion collisions as a signal of the onset of deconfinement using the Statistical Model of the Early Stage (SMES) [4]. Currently, the NA61/SHINE experiment is investigating nuclear collisions of intermediate system size between proton–proton and Pb+Pb collisions[22].

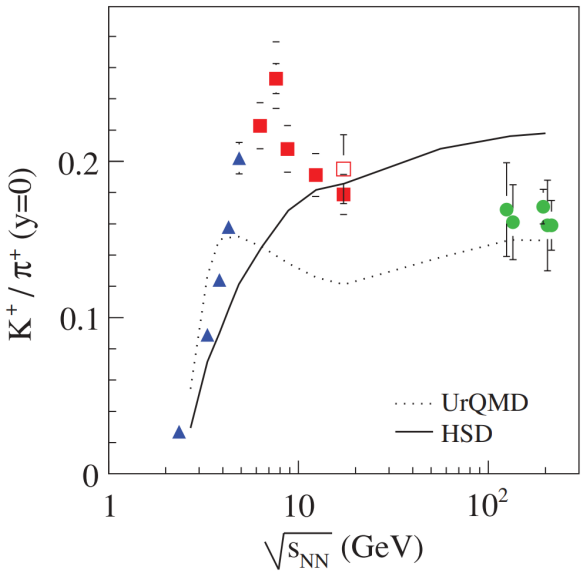

Figure 1.3: Energy dependence of the K^+/π^+ ratio measured by several experiments [4]. The red filled squares show NA49, the red open squares NA44, the blue triangles AGS, and the green circles RHIC results.

The nontrivial behavior of strangeness production at intermediate energies has triggered various theoretical interpretations. In the dynamical transport-model approach of Ref. [10], in addition to the effect of the onset of deconfinement, the restoration of chiral symmetry is proposed to play an essential role in forming the horn structure. As referred in Sec. 1.2.3, the probability of quark–antiquark pair creation from the vacuum depends on the constituent quark mass of the produced pair in Lund model. Ref. [10] introduces effective quark masses m_q^*, m_s^* (where q denotes u, d flavors) that incorporate chiral symmetry restoration, defined as

$$m_s^* = m_s^0 + (m_s^V - m_s^0)\frac{\langle\bar{q}q\rangle}{\langle\bar{q}q\rangle_V}, \tag{1.9}$$

$$m_q^* = m_q^0 + (m_q^V - m_q^0)\frac{\langle\bar{q}q\rangle}{\langle\bar{q}q\rangle_V}. \tag{1.10}$$

Here, the subscript V denotes vacuum, and the constituent quark masses are taken as $m_q^V = 0.35$ GeV and $m_s^V = 0.5$ GeV, while the bare quark masses are $m_q^0 \approx 7$ MeV and $m_s^0 \approx 100$ MeV. $\langle\bar{q}q\rangle$ represents the scalar quark condensate, which serves as the order parameter of chiral

symmetry; it approaches zero as the symmetry is restored. In this work, chiral symmetry restoration is described based on the nonlinear σ-ω model, and the in-medium behavior of $\langle\bar{q}q\rangle$ is constrained by the world-average pion-nucleon sigma term $\Sigma_\pi \approx 45$ MeV. As chiral symmetry is restored, the effective quark masses decrease, reducing the value of ${m_s}^2 - {m_{u,d}}^2$ in Eq. 1.7, which in turn is expected to increase the strangeness suppression factor γ_s.

Figure 1.4 shows the nucleon scalar density ρ_s, the quark condensate, the effective quark masses, and γ_s obtained in Ref. [10] using the transport model Parton-Hadron-String Dynamics (PHSD) at $T = 0$. Even at normal nuclear density $\rho_0 \sim 0.17$ /fm^3, an enhancement of γ_s is expected due to chiral symmetry restoration.

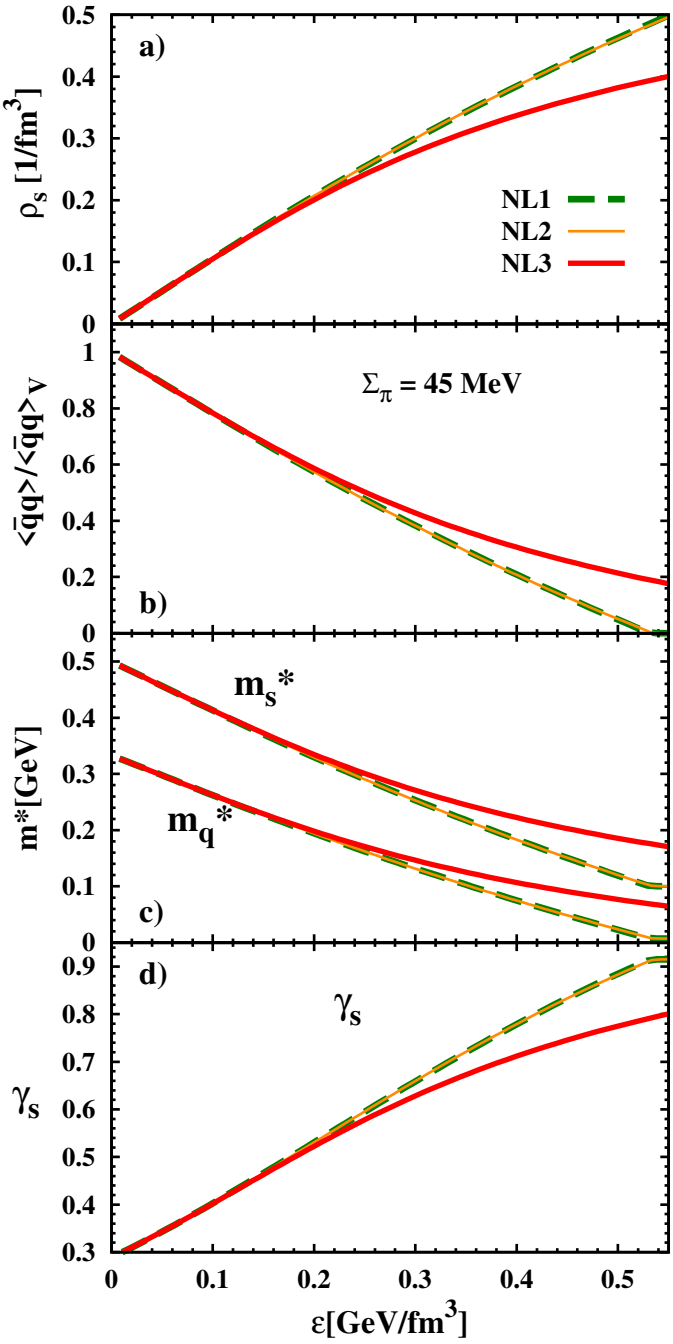

Figure 1.4: Energy-density dependence of the nucleon scalar density ρ_s, scalar quark condensate, effective quark masses, and γ_s. The three curves, NL1, NL2, and NL3, compare results obtained with different parameter sets of the nonlinear σ-ω model (ratios of effective to bare masses m^*/m and compression modulus). See Ref. [10] for details.

In this subsection, one example related to the restoration of chiral symmetry is presented. The behavior of strangeness production–including not only the enhancement at intermediate energies but also the decrease observed at higher energies–has been the subject of a wide range of theoretical interpretations. The present study evaluates the production cross sections, which is a general and broadly applicable observable. The present results provide information that can be utilized across different interpretations.

1.3.3 Mass Number Dependence

To investigate the production mechanism, the mass-number dependence of the production cross section is traditionally parameterized using α in the following form:

$$\sigma_{pA}(A) \propto A^{\alpha}. \tag{1.11}$$

$\alpha = 1$ indicates that the production cross section scales with the mass number, corresponding to a picture in which the ϕ meson is produced uniformly inside the nucleus. $\alpha < 1$ support a soft production process; in particular, $\alpha = 2/3$ corresponds to production occurring predominantly on the surface of the target nucleus. Conversely, $\alpha > 1$ indicates an enhancement of the production yield, possibly suggesting multiple collisions within nucleus, such as the Cronin effect [23].

Hadronic effects on the measured cross section

The produced ϕ mesons interact with spectator nucleons before being detected. Thus, the production cross section extracted from the measurement reflects not only the production mechanism but also these additional effects. In the context of focusing on such "absorption," the mass-number dependence is parameterized using the so-called transparency ratio:

$$T_A = \frac{\sigma_{pA}}{A\sigma_{pp}}. \tag{1.12}$$

A value of $T_A = 1$ implies that there is no absorption effect from the nuclear medium (corresponding to $\alpha = 1$ in Eq. 1.11).

For ϕ-meson production, several experiments using photon-induced [24, 25] and proton-induced [11] reactions have observed that absorption becomes stronger (i.e., T_A becomes smaller) for larger mass number A. This behavior has been discussed in relation to cold nuclear matter effects, in particular the in-medium width of the ϕ meson. The COSY-ANKE collaboration measured the momentum dependence of the transparency ratio, as shown in Fig. 1.5, using 2.83 GeV proton beams on C, Cu, Ag, and Au targets. For these results, various interpretations have been proposed, including a possible contribution from an N^* state [26] and in-medium effects [27]. It should be noted that they measured the K^+K^- decay branch of the ϕ meson. Due to the strong $\bar{K}N$ interaction, the observed signal may be affected by mechanisms other than the direct interaction between the ϕ meson and the nuclear medium.

Thus, the production cross section does not reflect the production mechanism alone; rather, it is a quantity influenced by various surrounding physical processes, and a careful discussion is required.

1.4 Experiments Planned in the High-momentum Beamline

At the high-momentum beamline constructed in 2020, 30-GeV proton beams accelerated by the J-PARC Main Ring synchrotron are extracted and directly delivered to the experimental

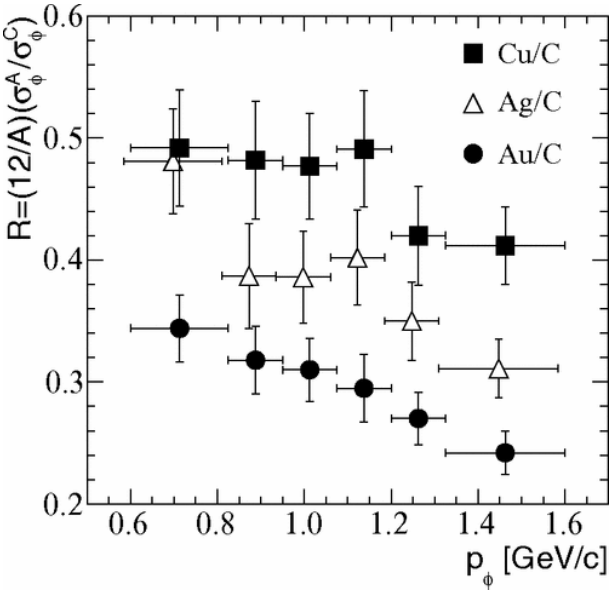

Figure 1.5: Momentum dependence of the transparency ratio measured by the COSY-ANKE collaboration [11].

target as a primary beam. In the future, a production target and beamline detectors will be installed at the high-momentum beamline to provide secondary beams up to 20 GeV/c (the π20 beamline). In addition, the J-PARC Heavy Ion (HI) project is planned, in which the accelerator will be upgraded to accelerate heavy ions and extract them to the high-momentum beamline. Details of the high-momentum beamline are described in Chapter 2. In this section, we review the physics programs of the first two experiments planned at the high-momentum beamline.

1.4.1 J-PARC E16 experiment

As the first program at the high-momentum beamline, the J-PARC E16 experiment is planned to investigate the restoration of chiral symmetry in a nuclear medium by measuring the in-medium spectral shape of the ϕ meson. The spontaneous breaking of chiral symmetry in the QCD vacuum is one of the mechanisms proposed to explain the origin of hadron masses. Although the restoration of chiral symmetry in nuclear matter has long been predicted theoretically, clear experimental signatures have not yet been established. Light vector mesons, $\rho/\omega/\phi$, serve as suitable probes for studying chiral symmetry restoration in a medium: their spectral shapes, typically masses and widths, are expected to be modified in nuclear matter [28, 29]. The vector mesons have dilepton decay channels that do not suffer the final state interaction in nuclei. In particular, the ϕ meson, unlike the ρ and ω, can be cleanly observed due to the absence of spectral overlap.

As a precedent, the KEK-PS E325 experiment [30] measured the invariant-mass spectrum of ϕ mesons via di-electron decays and suggested the spectral modification of ϕ mesons in nuclear matter. Figure 1.6 shows the ϕ-meson mass spectra measured in E325. The spectra are presented for different $\beta\gamma$ regions of the ϕ meson and for different target nuclei, and the excess over the in-vacuum spectrum was observed under the conditions most favorable for in-medium decay, namely low $\beta\gamma$ and heavier target nuclei. The observed modification was parameterized in terms of changes in mass and width within the Breit-Wigner formalism, resulting in a 3.4% mass reduction and a width increase by a factor of 3.6.

The J-PARC E16 experiment aims to investigate the modification suggested by the E325 experiment with much higher statistics and improved mass resolution, and to establish the spectral modification of the ϕ meson in nuclear matter. Figure 1.7 shows the simulated mass

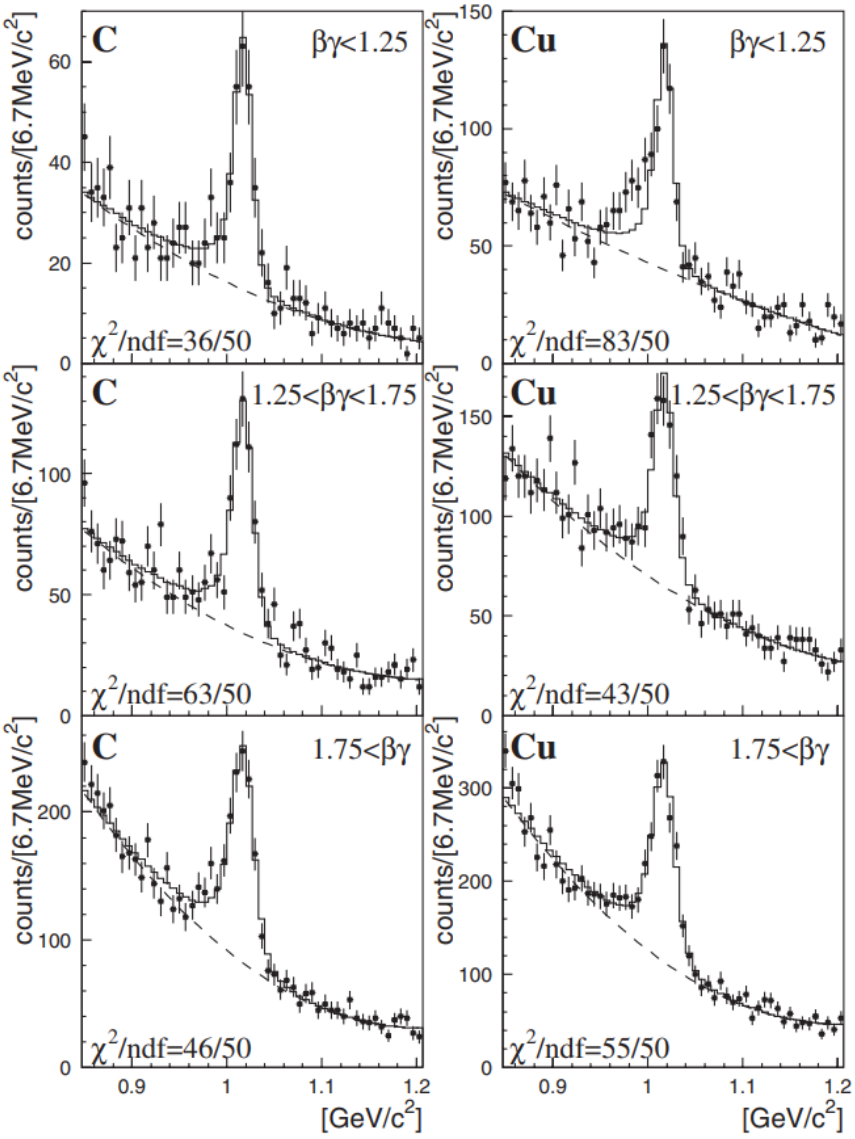

Figure 1.6: e^+e^- invariant mass spectra observed by the KEK-PS E325 experiment [30].

spectra expected in the first phase (Run 1) of E16. In this simulation, the collection of 15,000 ϕ-meson events is assumed, together with the mass-decreasing and width-broadening parameters reported by E325. As shown in Fig. 1.7, statistically significant excesses are expected to be established in all $\beta\gamma$ regions. The $\beta\gamma$-dependent yield of this excess would provide strong evidence for in-medium mass modification of the ϕ meson inside nuclei.

The present study was conducted using the dielectron spectrometer developed for the E16 experiment, as well as the commissioning data obtained in E16. A detailed description of the experimental setup of E16 is provided in Chapter 2.

1.4.2 J-PARC E88/SAΦRE experiment

Complementary to the E16 experiment, which aims to observe spectral modification of the ϕ meson through its dielectron decay, the J-PARC E88/SAΦRE experiment has been proposed to measure the $\phi \to K^+K^-$ decay. In addition to the advantage of a larger branching ratio, the measurement of the K^+K^- decay channel allows one to study the polarization dependence of the ϕ-meson dispersion relation in nuclear medium [32]. As shown in Fig. 1.8, the in-medium properties of the ϕ meson are theoretically expected to follow distinct dispersion relations

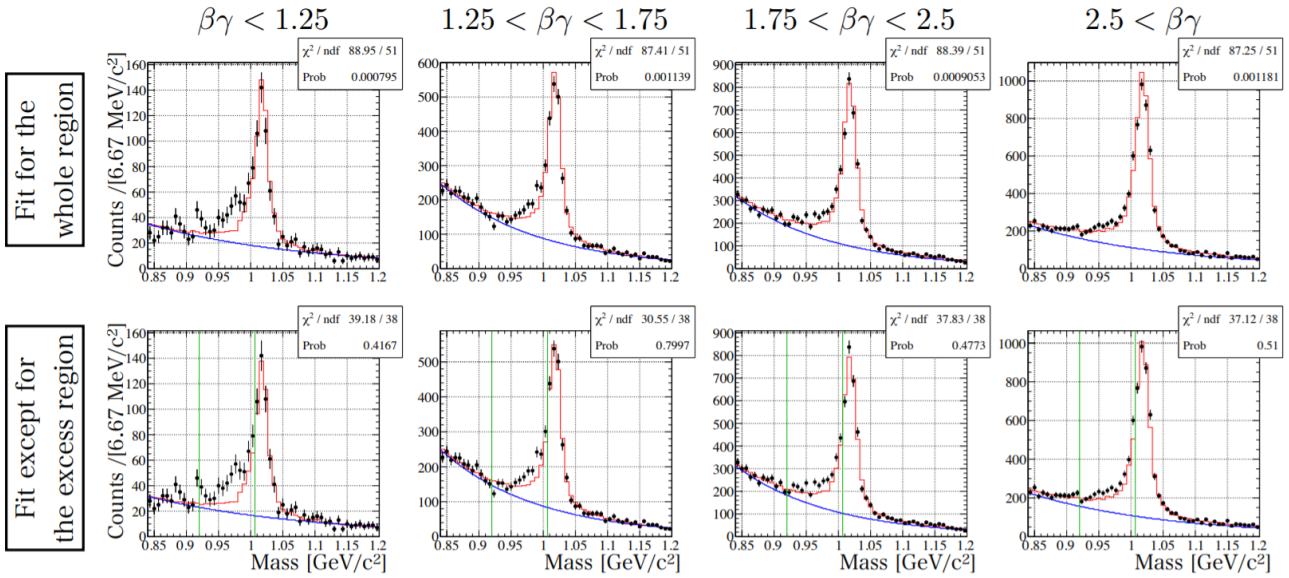

Figure 1.7: Expected e^+e^- mass spectra in the E16 Run-1 [31].

for the transverse and longitudinal components [33]. The polarization is correlated with the emission angle θ of the decay products in the ϕ-meson rest frame. Unlike the e^+e^- decay, the K^+K^- decay allows a clean separation of the parent ϕ-meson polarization at $\cos\theta = 0$ and $\cos\theta = \pm 1$ [32]. This feature provides a possibility to access the polarization dependence of the dispersion relation. The experimental significance of this measurement is discussed in Ref. [31].

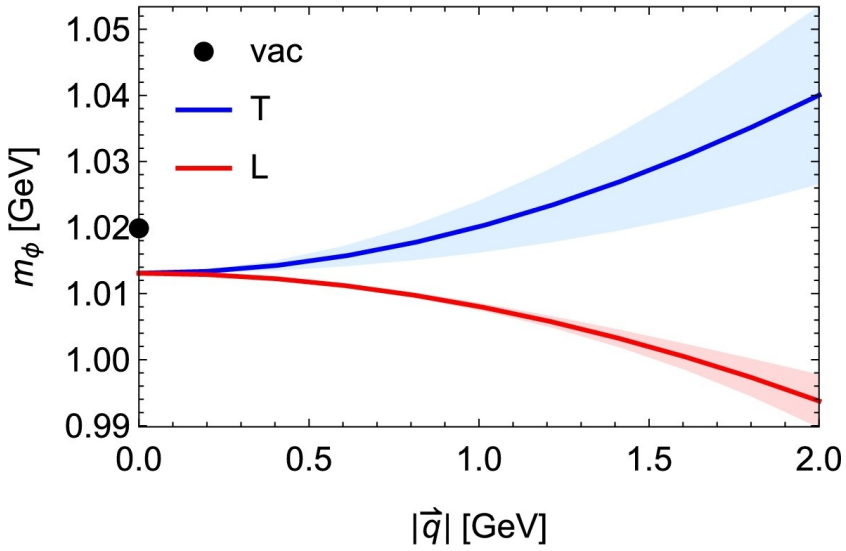

Figure 1.8: Dispersion relation of the in-medium ϕ meson derived from the QCD sum rule approach [33].

In the E88 experiment, a Multi-gap Resistive Plate Chamber (MRPC) and an aerogel Cherenkov counter will be installed within a part of the E16 spectrometer acceptance to enable kaon identification. The tracking devices are shared with the E16 experiment. With the capability to identify π, K, and p, the experiment can access to a wide variety of hadrons in addition to vector mesons. This not only opens the possibility of measuring hadron-production ratios, as mentioned in Sec. 1.1, but also enables a femtoscopy program using this setup, which is currently under development [34].

1.5 Structure of This Thesis

The structure of this thesis is outlined below. Chapter 2 describes the experimental setup used in this study. This chapter also introduces the high-momentum beamline at the J-PARC Hadron Experimental Facility, which was utilized for physics data acquisition for the first time by the present work. Chapter 3 details the analysis procedure. After describing the calibration of the detector signals, the method of event reconstruction is presented. The detection efficiency of the ϕ meson is then evaluated, followed by an estimation of the number of incident protons that contributed to ϕ-meson production in this measurement. Chapter 4 presents the invariant-mass distributions reconstructed from the momenta of e^+e^- pairs and describes the extraction of the ϕ-meson yield. The total ϕ-meson production cross section is estimated using the event generator JAM, and the obtained results are discussed. Finally, Chapter 5 summarizes the conclusions of this thesis.

Chapter 2

Experimental setup

This chapter describes the experimental setup used in the present measurement, including the experimental facility, beamline, detectors, trigger system, and DAQ system. Since this study was conducted using the pilot data of the J-PARC E16 experiment, the setup of the E16 experiment is presented here.

2.1 J-PARC and Hadron Experimental Facility

Japan Proton Accelerator Research Complex (J-PARC) was constructed by the High Energy Accelerator Research Organization (KEK) and the Japan Atomic Energy Agency (JAEA) as the successor to the KEK Proton Synchrotron, which finished operation in 2005. Figure 2.1 shows an overview of J-PARC. The acceleration is performed with three stages: negative hydrogen ions generated at the ion source are accelerated to 400 MeV by the linear accelerator (LINAC), then converted into a proton beam by stripping electrons in a carbon foil. The protons are subsequently accelerated to 3 GeV by the Rapid Cycling Synchrotron (RCS) and further to 30 GeV by the Main Ring (MR) synchrotron. In the synchrotrons, the bunched beam is accelerated as it passes through the RF cavity. Each bunch contains approximately 10^{13} protons. The accelerated beam is extracted and transported to the Hadron Experimental Facility (HEF) or the Neutrino Experimental Facility (NEF). In experiments at the HEF, it is essential to detect individual reaction events, so slow extraction (SX), in which the beam is extracted continuously with a low instantaneous intensity, is preferred over fast extraction (FX) for the NEF, where the entire bunched beam is extracted at once. During the present data-taking period, the beam was extracted to the HEF over a 2-second length interval within a 4.24-second cycle.

2.2 High-momentum Beamline

Figure 2.2 shows the beamline from the MR to the HEF. Most of the extracted beam is transported to the "T1 target" in the HEF (A-line) to produce secondary beams, while 0.02% of the beam is branched and transported to the high-momentum beamline (B-line), which is approximately 150 m long. This beam is delivered directly to the experimental target without passing through a production target. After passing through the experimental target, the beam intensity is monitored by two ion chambers. One is for precise measurement of intensity and the other is for the time-dependent information as shown in Fig. 2.4. Absolute beam intensity is calibrated using the activation method based on the production of ^{24}Na in aluminum and copper foils [36, 37].

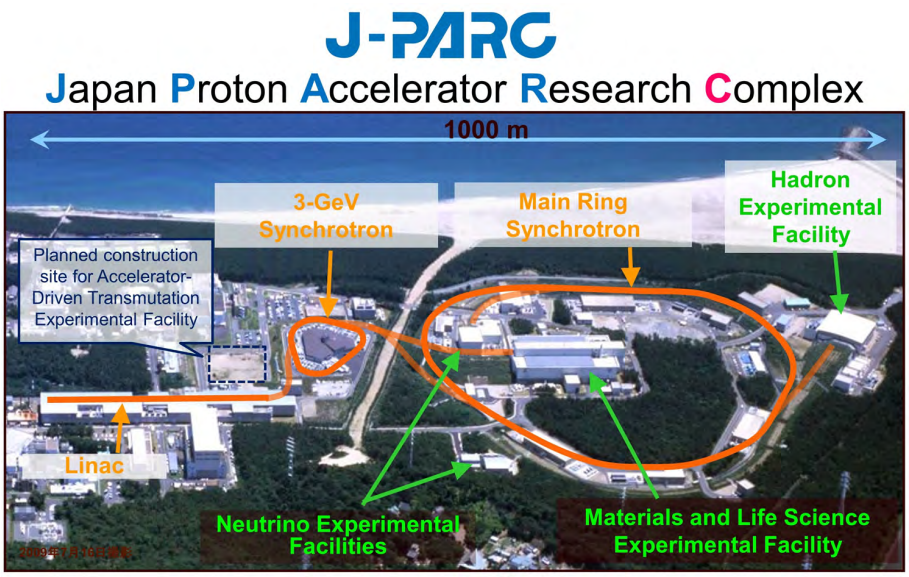

Figure 2.1: Bird's-eye view of the J-PARC [35].

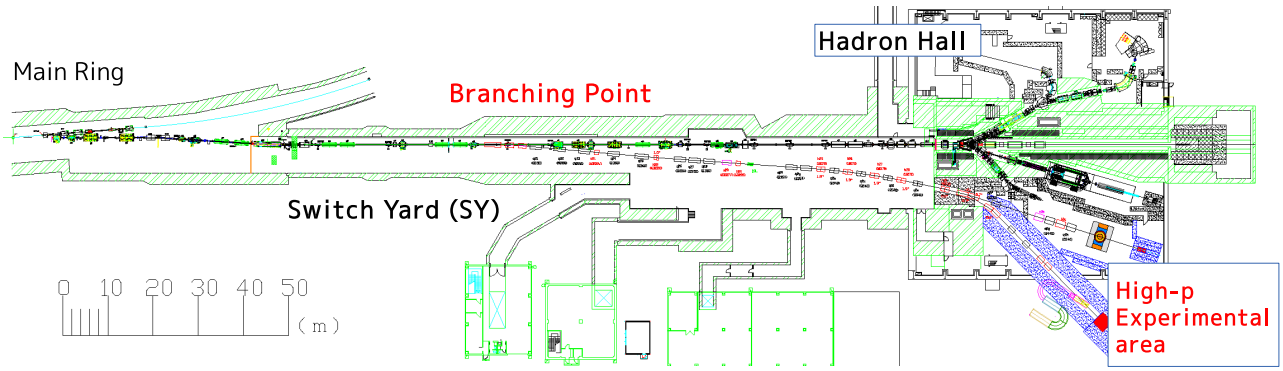

Figure 2.2: Beamline layout from the MR to the HEF.

Figure 2.3 illustrates the mechanism by which the beam is branched into the high-momentum beamline. A Lambertson magnet is used for the branching. While most of the beam passes straight through the field-free gap, only a small fraction of 0.02% traverses the magnetic-field region, where its trajectory is bent and directed into the high-momentum beamline. The beam intensity in the high-momentum beamline is adjusted by controlling the beam position in vertical direction at the Lambertson magnet. During the physics data taking of the present measurement, the beam intensity was approximately $1\times\ 10^{10}$ protons/spill. Typical deviation of intensity is ± 10 % in rms in an hour. For the calibration data, two nominal beam intensities 1×10^{9} and 5×10^{9} were also used.

Although a constant beam intensity is ideal in slow extraction, in practice, a time structure appears due to various factors. First, we observed the large-intensity beam that appears during the first $\sim$0.1 sec. of the 2-sec. extraction period. To deal with it, a "ramp control" was applied, in which the current of five vertical bending magnets is dynamically controlled during a spill. Figure 2.4 shows the time structure of the beam measured with the ion chamber after applying the ramp control.

Furthermore, two kinds of time microstructures of the beam had already been investigated during the commissioning prior to the present measurement. In the commissioning performed in February 2021, it was observed that the trigger accept rate was extremely low compared to the trigger request rate (DAQ efficiency of 15%). This suggested that the timing of the requests was

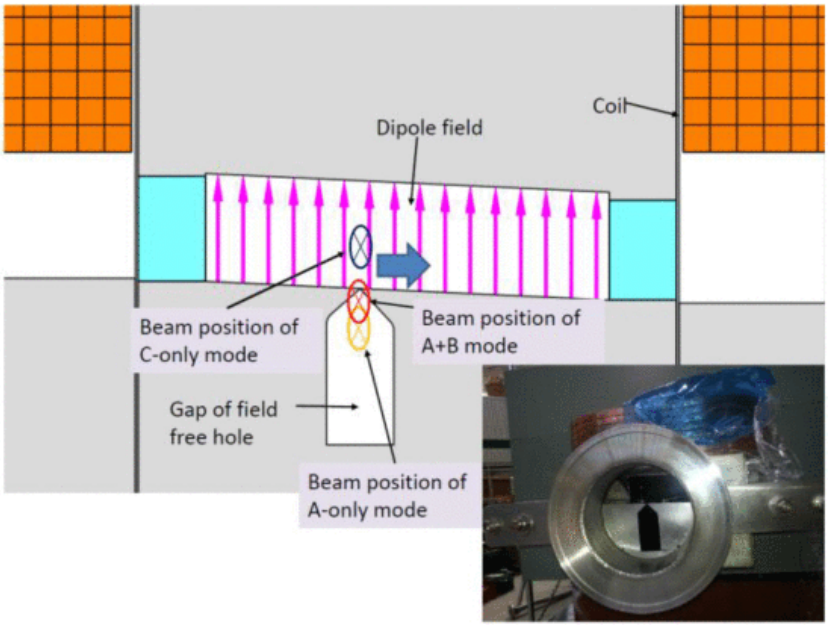

Figure 2.3: Cross-sectional view of the Lambertson magnet used for branching the beam into the high-momentum beamline [38].

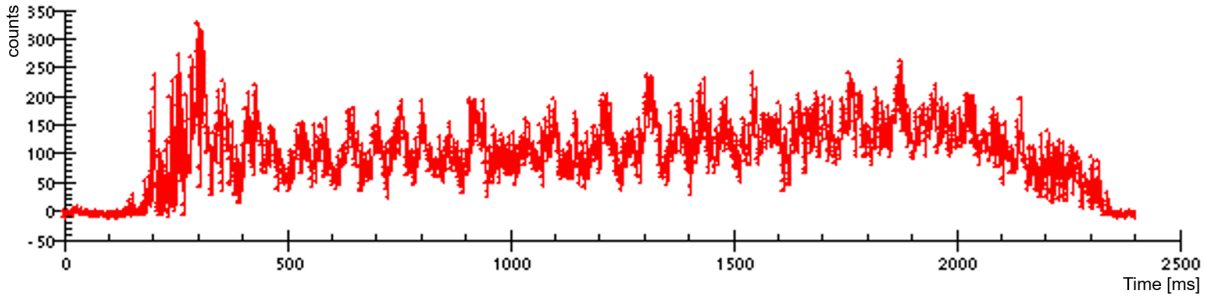

Figure 2.4: Time structure for a single spill measured with an ion chamber. Ramp control is applied.

highly localized, being strongly affected by the busy time. To investigate this issue, streaming TDC data using the Hadron Universal Logic Module (HUL) were acquired during the beam time in May-June 2021. Although the ion chamber directly measures the beam intensity, its response is slow; therefore, the single rates of several LG channels were monitored instead. As a result, two types of beam microstructures were observed, and their origins are guessed to be as follows:

- A time structure with a 5 msec period, corresponding to the current ripple of the MR power supply.
- A time structure with a 5.2 μsec period, corresponding to the MR cycle (191 kHz), which is considered to be related to the optical dispersion at the Lambertson magnet.

Due to the presence of these beam structures, in addition to the aforementioned reduction in DAQ efficiency, another issue arose: collision-overlapping events were frequently triggered, leading to high hit and track multiplicity and making the analysis difficult. As one of the countermeasures, a trigger veto was introduced during periods in which the hit multiplicity of the trigger signals was high. Although this reduces the effective beam intensity, improvements in both DAQ efficiency and analysis efficiency are expected to be more than make up for the possible reduction of beam intensity due to the veto. Details are described in Sec. 2.5.1.

2.3 Experimental Targets and Target Chamber

To measure the mass number dependence, two types of nuclear targets (carbon and copper) were employed as the experimental targets. We adopted thin targets because e^+e^- production from γ rays generated by the energy loss in the target becomes a source of background, and therefore must be minimized. The specific target configuration is summarized in Table 2.1. Figure 2.5(a) illustrates the scheamtic view of the experimental targets.

Table 2.1: Configuration of experimental targets. The z-axis is aligned with the beam direction. The origin is defined at the center of the dipole magnet.

Target	Position z (mm)	Nominal thickness (mm)	Thickness (mg/cm^2)	Interaction length (%)	Radiation length (%)	Width (mm)
Cu	+20, −20	0.08	70.8	0.052	0.55	10
C	0	0.5	89.6	0.102	0.21	10

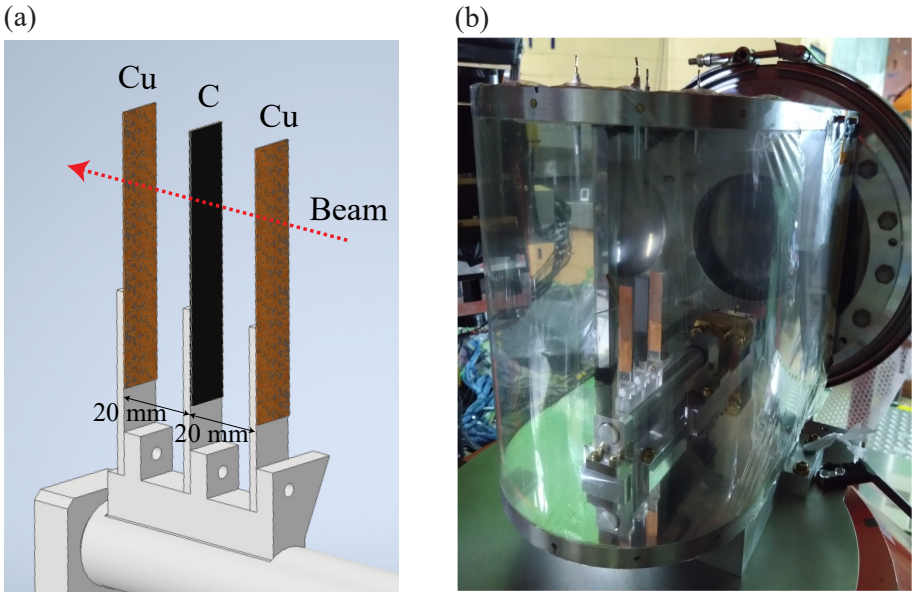

Figure 2.5: (a) Schematic view of the three experimental targets. (b) Photograph of the target chamber installed in the pole gap of the spectrometer magnet. The end window of the beam pipe is also seen.

The beam is transported through the high-momentum beamline, which is kept under vacuum, to the experimental targets. The window of the beam pipe is located at ∼60 mm upstream of the center of the dipole magnet, and downstream of that point a target chamber filled with helium is installed, to suppress the energy loss of the beam. A photograph of the target chamber is shown in Fig. 2.5(b). A lever allows switching between the experimental targets, a rod for beam-profile measurements, and an empty state. Helium bags are placed downstream of the target chamber up to the position of the ion chamber to reduce activation of the experimental hall by the transmitted beam.

2.4 J-PARC E16 Spectrometer

The E16 spectrometer consists of a large-aperture dipole magnet and four types of detectors. As tracking detectors, a single layer of Silicon Strip Detector (STS) and three layers of GEM

Trackers (GTR) are used. For electron identification, a two-stage system is employed: the Hadron Blind Detector (HBD), which is a gas Cherenkov detector, and the lead-glass calorimeter (LG). A horizontal cross-sectional view of the detectors inside the spectrometer is shown in Fig. 2.6. The series of detectors indicated by the magenta lines in Fig. 2.6 is referred to as a module. Eight modules were installed during the present measurement.

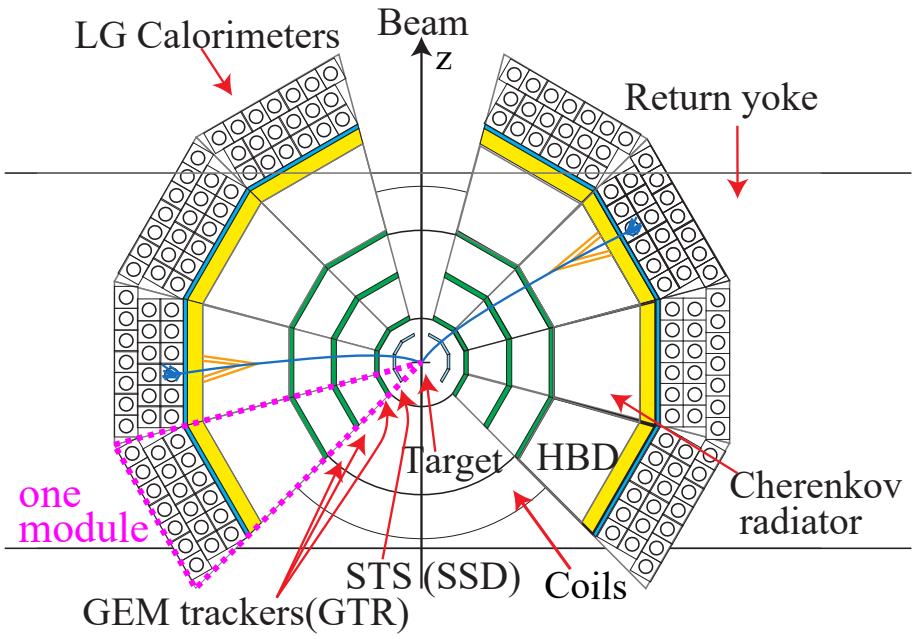

Figure 2.6: Horizontal cross-sectional view of the E16 spectrometer.

2.4.1 FM Magnet

Figure 2.7 shows a photograph of the FM magnet. The inner height is 3240 mm and the pole gap is 400 mm. A magnetic field of 1.77 T is generated at the center of the pole gap when a current of 2450 A is applied. The target chamber is placed inside this pole gap. The pole pieces of the FM magnet are shaped conically to detect particles produced at the target with a wide acceptance. As a result, the magnetic field spreads widely, and the region where the tracking devices are installed (defined by $R < 600$ mm in cylindrical coordinates) is affected by a non-uniform magnetic field.

The trajectories of charged particles are reconstructed by numerically solving the equations of motion in the magnetic field using the Runge–Kutta method, with the hit positions measured by the tracking devices and the magnetic field at each spatial point (the field map) as constraints. The field map is based mainly on calculations performed with the TOSCA software [39]. Its absolute values are corrected using the measured values, which can be attributed to differences in the BH curve of the actual magnet. The measurements were carried out using a Hall probe (Group3 MPT-132) with an accuracy of $\pm 0.1\%$. The uncertainty of the measurement was evaluated to be 0.13% from repeated measurements at the same points. The measured values were found to be up to 1.4% larger than the calculated values. Therefore, the ratio of the measured to calculated B_y values was used as a scale factor, and an R-dependent scale factor was applied to all components (B_x, B_y, B_z) of the calculated field to obtain the field map used in this analysis. This correction reduced the discrepancy between the calculated and measured fields to 0.2% at most, in the field integral in the tracking region, namely, from $R = 0$ mm to 600 mm. In the field-map calculation, the presence of the surrounding SKS magnet and iron shielding was taken into account.

During data taking, the stability of the magnetic field was monitored using a Hall probe mounted on the top of the target chamber. The variation during the data taking was within 0.1%, confirming stable operation.

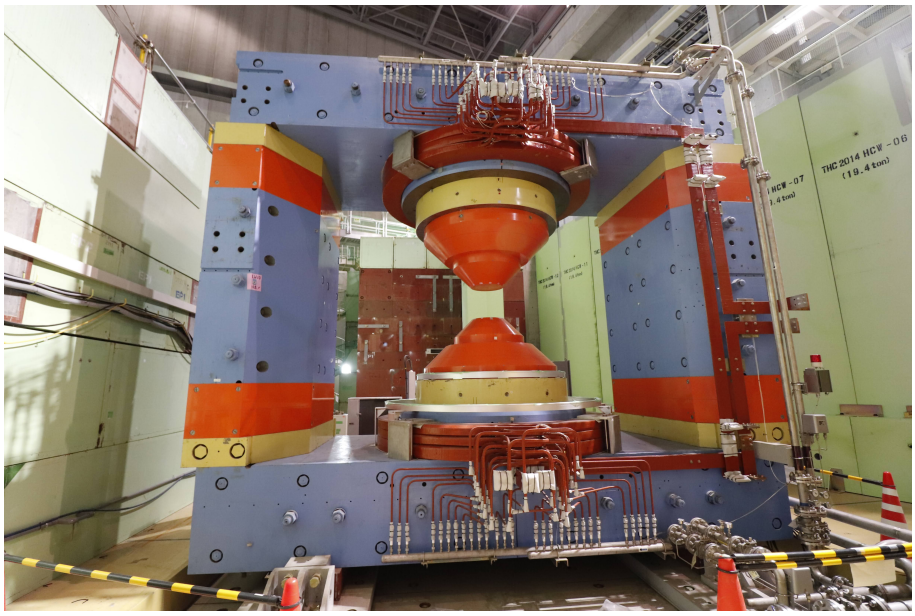

Figure 2.7: Photograph of the FM magnet.

2.4.2 Silicon Tracking System (STS)

As the innermost tracking device, a single layer of Silicon Strip Detector (SSD) is used. In this experimental setup, the SSD provides higher time resolution and higher channel granularity than the GTR, which helps distinguish overlapping tracks in a high-multiplicity environment. Quantitatively, a position resolution of 25 μm, a time resolution of 6 nsec, and a detection efficiency above 95% are required for the E16. To satisfy these requirements, the sensors and front-end electronics developed for the FAIR CBM experiment, to be constructed in Darmstadt, Germany, were adopted for the E16 experiment. This system is called the Silicon Tracking System (STS). The performance of the sensors are summarized in Table 2.2.

Table 2.2: Basic specification of the silicon sensor developed by the CBM experiment.

Parameter	value
Size	62×62 mm^2
Sensitive area	60×60 mm^2
Thickness	320 μm (0.37%X_0)
Strip pitch	50 μm
Stereo angle	7.5 deg.
Number of Strips	1024
Position resolution	(x) 15 μm, (y) 110 μm
Time resolution	∼6 nsec.

Figure 2.8 shows the readout chain developed for the E16 experiment. Signals induced on the sensors are transferred via microcables to the FEB-8 (Front End Board). The FEB-8 is equipped with the STS-MUCH XYTERv2 (SMX), a self-triggered, continuous readout ASIC developed for the CBM experiment. In the SMX, the signal is split into two processing paths: one through a fast shaper for the TDC, and the other through a slow shaper for the ADC. The

fast signal passes through a 320 MHz, 14-bit discriminator logic and is transferred downstream with a timestamp. The slow signal is processed by a 5-bit ADC with a dynamic range of 0–14 fC and then sent downstream.

In the subsequent GBTxEMU board, data from the FEB-8 are aggregated and transferred to the GERI board. Because this board cannot operate in a magnetic field, an LVDS repeater was inserted between the FEB-8 and the GBTxEMU to make the system suitable for the E16 environment. Although the original STS for the CBM experiment was designed to operate in a self-trigger mode, an online hit-selection system was implemented for the E16 experiment: the GBTxEMU board receives the trigger signal, and the GERI board transfers only the data around the trigger timing to the PC.

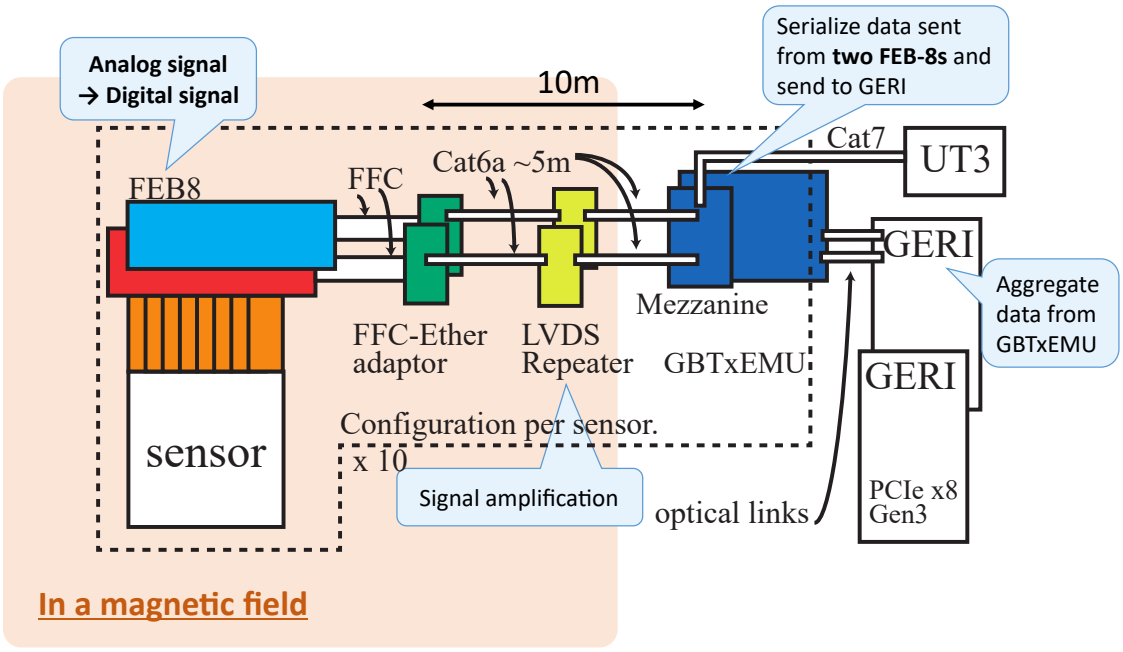

Figure 2.8: Schematic diagram of the STS readout chain.

Figure 2.9 shows the sensors, microcables, and FEB-8 modules installed on the aluminum support designed for the E16 experiment. The all STS modules, together with this support, is placed in the gap between the poles of the FM magnet. The target chamber is installed inside the inner region of the STS sensor.

2.4.3 GEM Tracker (GTR)

The GEM tracker (GTR) is a detector for the position detection, by amplifying ionized electrons from the incident particles using a gas electron multiplier [40], and detecting the amplified signals on strip-shaped electrodes. In the E16 experiment, tracking is performed using three layers of GTRs together with one layer of the STS.

A schematic view of the GTR is shown in Fig. 2.10. As illustrated in Fig. 2.10(a), the chamber is constructed by stacking a mesh electrode for applying the drift voltage, three GEM foils, a readout strip foil at the bottom, and a Mylar layer at the top, all fixed to an aluminum frame using PEEK (Poly Ether Ether Ketone) bolts. Figure 2.10(b) shows the chamber after assembly, and Fig. 2.11 summarizes the distances between the foils.

For amplification, a gas mixture of Ar and CO_2 in 7:3 is used, continuously flowed at 20 ml/min throughout the experiment.

One chamber constitutes a single tracking layer. Three layers of GTRs are used in the E16 experiment, with active areas of 100×100 mm^2, 200×200 mm^2, and 300×300 mm^2, respectively.

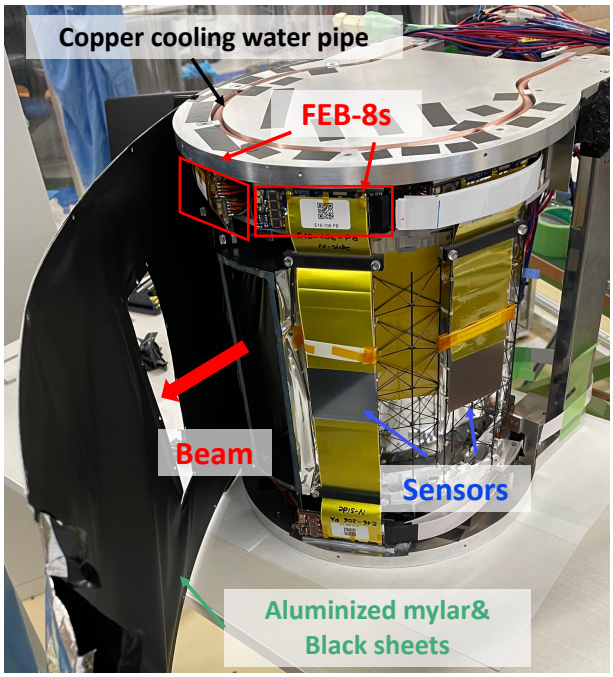

Figure 2.9: Sensors, microcables, FEB-8 boards installed on the aluminum support.

The three chambers are mounted on a Carbon Fiber Reinforced Plastics (CFRP) frame. The CFRP frame is fixed inside the FM magnet via an aluminum base. Figure 2.12 shows the GTR chambers installed on the CFRP frame.

A GEM consists of a thin insulating foil coated with electrodes on both sides and perforated with microscopic holes. By applying a voltage to the electrodes in an amplification gas, an electric field is formed inside each hole, where an avalanche is initiated and the electrons are multiplied. The GEM foils used in the E16 experiment were manufactured by the domestic company RAYTECH Inc.[1] using a chemical-etching technique. Polyimide is used as the insulator and copper as the electrode material. The GEM holes are biconical in shape, with a diameter of 70 μm on the electrode surfaces. The holes are arranged in a triangular lattice across the entire foil, with a pitch of 140 μm.

The total material budget of the GEM chamber is designed to be below 1% of a radiation length. The readout plane consists of strip electrodes segmented in two orthogonal directions: horizontal (local x) and vertical (local y). The pitch is 350 μm for the x-strips and 1400 μm for the y-strips.

Signals detected on the readout strips are processed by the APV25-s1 chip and the SRS system, both developed by the CERN RD51 collaboration. This is the same readout scheme used for the HBD, described in the next section. The APV25-s1 chip contains a 192-cell analog pipeline, from which data are read out upon receiving a trigger signal. Each chip can receive 128-channel input. The maximum latency, determined by the pipeline depth, is 4 μs. In the present measurement, the APV system was operated with a sampling frequency of 31.25 MHz and 15 recorded cells per event. For the HBD, the APV25-Hybrid card developed by the RD51 collaboration is used. For the GTR, due to constraints on the installation space inside the spectrometer, the TRK-APV board developed for the E16 experiment [41] is used together with a repeater. The signals are then sent to the SRS-ATCA system, where they are digitized [42].

[1]Formerly known as RAYTECH Inc. `http://raytech-inc.co.jp`: The current name of the company is 'TRENG F Products Inc.'

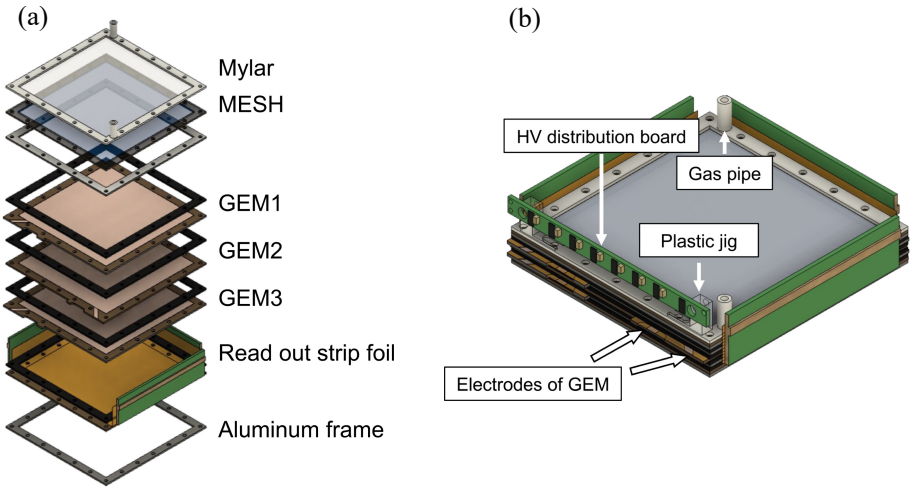

Figure 2.10: Schematic view of the parts and assembled shape of a GTR chamber, taken from Ref. [41].

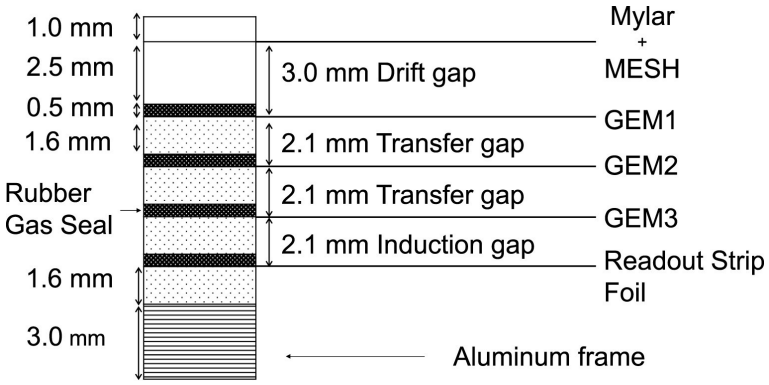

Figure 2.11: Vertical cross-sectional view of the GTR [41].

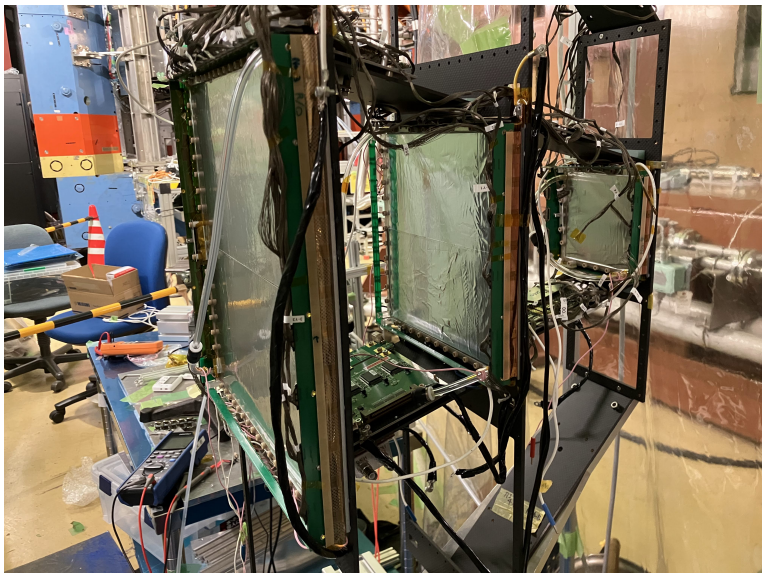

Figure 2.12: Photograph of the three GTR chambers mounted on the CFRP frame.

2.4.4 Hadron Blind Detector (HBD)

The HBD is one of the two electron identification detectors in the E16 experiment, and it is a gas Cherenkov detector. It was originally proposed by Y. Giomataris and G. Charpak [43] and was first implemented in the PHENIX experiment at BNL RHIC [44]. Figure 2.13 illustrates the electron-identification mechanism of the HBD. The detector consists of a CF_4 radiator, a stack of three GEM foils, a mesh electrode placed above the GEM stack, and a CsI photocathode evaporated onto the surface of the top GEM. Cherenkov photons emitted by incident electrons are converted into photoelectrons at the CsI photocathode, amplified in the GEM stack, and detected on the readout pads. Thus, CF_4 serves also as the amplification gas.

Hadrons, which have larger masses than electrons, do not emit Cherenkov photons. However, they ionize the gas and produce ionized electrons. To prevent these ionized electrons from being amplified in the GEMs, an electric field is applied to the mesh electrode in a configuration known as "reverse bias," which directs the electrons away from the GEM stack. As a result, in principle, only electrons originating from Cherenkov photons are amplified and detected.

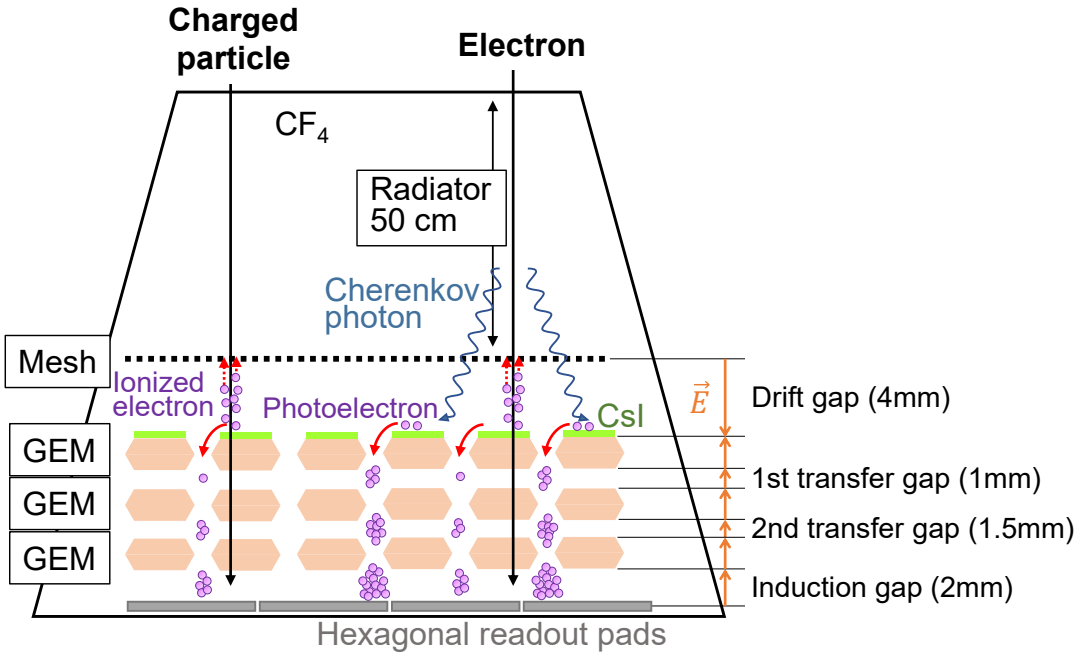

Figure 2.13: Schematic view working principle of HBD.

The thickness of the E16 HBD radiator is 50 cm for perpendicular incidence. The distance of the drift gap (defined by the top GEM and the mesh electrode) is 4 mm, and the gaps between the GEM foils are 1 mm and 1.5 mm, and the induction gap is 2 mm (between the bottom GEM and the readout pads), respectively. Ionization electrons produced in the drift gap can be absorbed by the mesh electrode, whereas those generated between the first and second GEMs would otherwise pass directly into the subsequent amplification stages, degrading the hadron-rejection performance. For this reason, the gap between the first and second GEMs is set to 1 mm, narrower than the others. The GEM foils for the HBD are also manufactured by RAYTECH.

The HBD readout plane is located at approximately $R \sim 1200$ mm inside the spectrometer, which is roughly twice the size of the outermost GTR layer (300×300 mm^2). Accordingly, one HBD module consists of four GEM stacks, each of size 300×300 mm^2, arranged to cover the acceptance. Unlike the GTR, the HBD uses GEM foils with smaller hole diameters and pitches–55 μm and 110 μm, respectively–since smaller holes generally provide higher gain.

Figure 2.14 shows a photograph of the internal view of the HBD vessel. The vessel is con-

structed as a pair of connected modules so that Cherenkov photons produced at the boundary between modules can be detected.

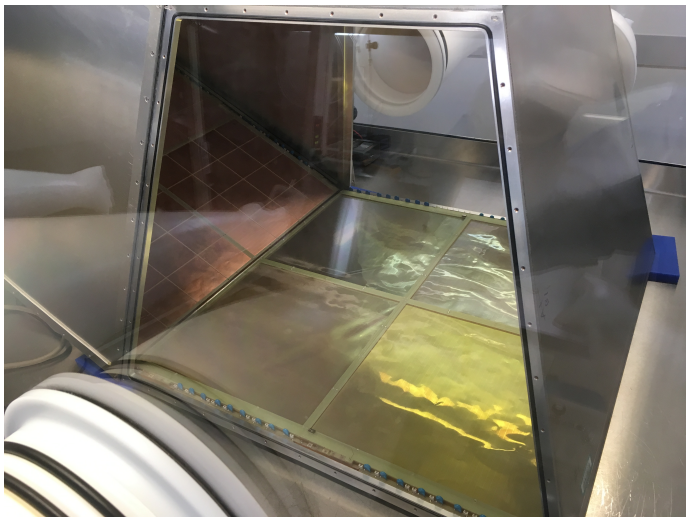

Figure 2.14: Photograph of the vessel and internal view of the HBD.

The refractive index of CF_4 at atmospheric pressure is approximately $1 + 6.20 \times 10^{-4}$, with some wavelength dependence. Under this condition, the Cherenkov threshold for π mesons is 4.2 GeV/c, which is sufficiently higher than the momentum range of electrons targeted in the E16 experiment. The wavelength range of Cherenkov photons detectable by the HBD is determined by the work function of the CsI photocathode and the cutoff of the CF_4 gas, covering roughly 100–200 nm, corresponding to photon energies of 6.2–12.4 eV. Photons in this wavelength region are absorbed by moisture and oxygen impurities in the gas, which affects the electron-detection efficiency of the HBD [44]. Therefore, during operation, the gas is continuously flowed at a typical rate of 1 L/min between two modules, and the moisture and oxygen contamination are monitored. To ensure gas-tightness, the HBD vessel is fabricated by welding aluminum plates.

The HBD readout plane consists of hexagonal pads with a side length of 10 mm, as shown in Fig. 2.15, providing 1400 readout channels per module. The diameter of the circular area where the Cherenkov photons distributed is 34 mm for the 50 cm CF_4 radiator. Consequently, electron signals typically spread over multiple pads, whereas hadron-induced signals are localized in a small number of pads. In offline analysis, clustering is performed, and clusters with large cluster sizes are selected to enhance hadron rejection performance. Hexagonal pads are used so that each pad shares only three vertices with its neighbors, preventing excessive charge sharing that would otherwise degrade the signal-to-noise ratio.

Figure 2.16 shows the cluster-size distributions for electrons and background particles [45]. These data were obtained during the 2024 commissioning run of the E16 experiment, where particle identification was performed using the LG, the other electron-identification detector.

As described in the previous section, the readout electronics consist of the APV25-s1 chips mounted on the APV-Hybrid boards, together with the SRS-ATCA system.

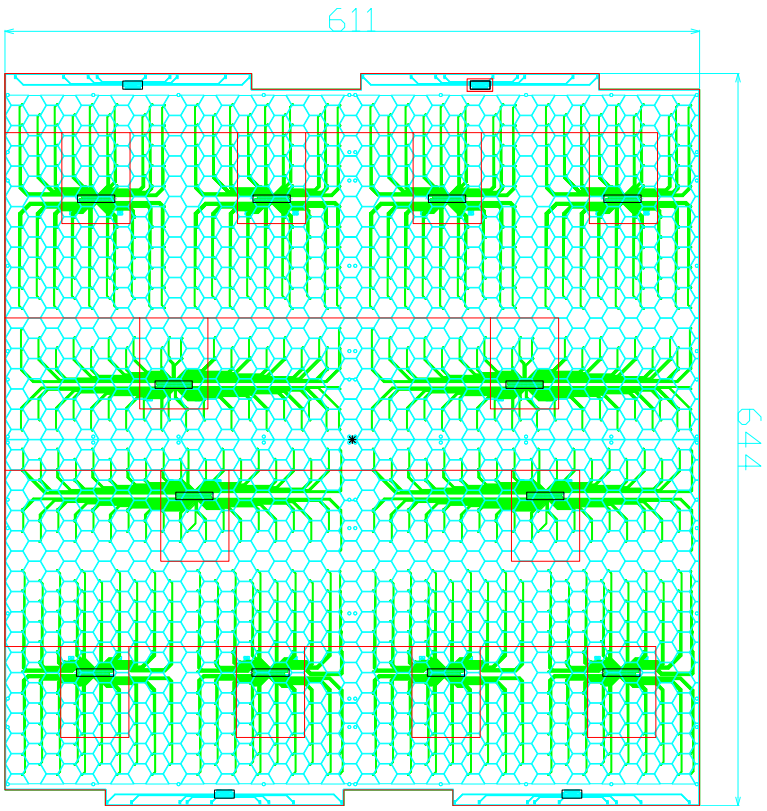

Figure 2.15: Schematic of the HBD readout pads, consisting of hexagonal pads with a side length of 10 mm.

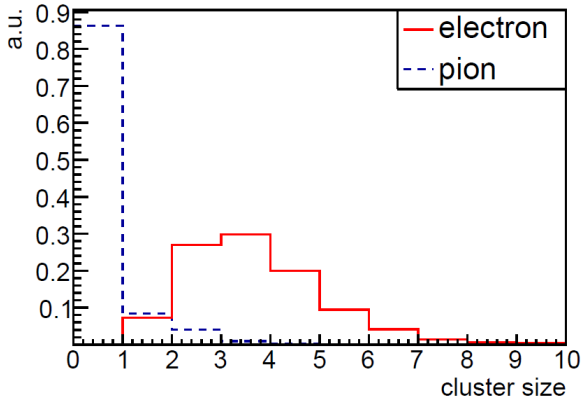

Figure 2.16: Cluster size distribution for the electron and pion samples [45].

2.4.5 Lead-glass Calorimeter (LG)

The lead-glass calorimeter, an electromagnetic calorimeter, is used in the E16 experiment for electron identification. Electrons entering the lead glass produce an electromagnetic shower through bremsstrahlung and pair production. Cherenkov photons emitted by the shower in the lead glass are detected by photomultiplier tubes. In contrast, hadrons such as pions, being much heavier than electrons, produce almost no shower.

The E16 experiment uses the lead-glass material SF6W [46]. Its properties are summarized in Table 2.3. Lead glass material is recycled from the TOPAZ LG calorimeter[46], as KEK-PS E325 experiment did. The lead-glass blocks used in E16 have dimensions of 122 × 154 × 135 mm^3 (width × height × depth), corresponding to a thickness of 8 radiation lengths. Although this thickness is insufficient to detect the complete energy loss of electrons with energies in the GeV range, the response has been confirmed to be linear for incident electron momenta between 0.5 and 4 GeV/c, based on measurements using the electron beam at the KEK PF-AR test-beam line. The setup of the measurement and the LG response to the electron beam are explained in Fig. 2.17.

Table 2.3: Specifications of the lead glass SF6W [46].

Parameter	value
Radiation length (X_0)	1.7 cm
Refractive index	1.8
Density	5.2 g/cm^3
Critical energy	12.6 MeV
Moriele radius	$1.7X_0$

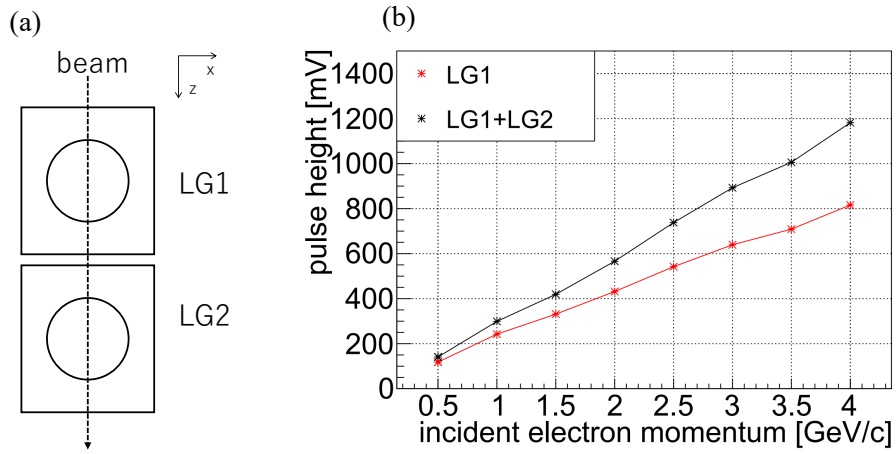

Figure 2.17: (a) The configuration of the LG for the electron beam. (b) The LG response to the electron beam. The momentum dependence of the mean of the charge distribution is plotted.

Pions, which are the dominant background particles, do not generate electromagnetic showers in the lead glass; however, they do emit Cherenkov photons corresponding to the length they traverse. In the LG calorimeter for the E16, the signal from such pions corresponds to approximately 0.15 GeV in electron energy. Therefore, electrons can be distinguished from pions with momenta above 0.4 GeV/c. On the other hand, incident pions may experience nuclear interactions in the lead glass, producing π^0 mesons whose decay photons can generate electron-positron pairs. As a result, unlike threshold-type detectors such as the HBD, raising the threshold cannot completely eliminate pion contamination. Quantitatively, at a threshold

corresponding to a 90% detection efficiency for 0.4 GeV/c electrons, the pion-rejection factor is evaluated to be 90% [47].

The Cherenkov photons are detected by photomultiplier tubes with a 3-inch photocathode diameter, specifically fine-mesh type PMT Hamamatsu R6683, positive-bias type, recycled from Belle Aerogel counter. Because the E16 spectrometer has a surrounding magnetic field (approximately 200 mT at the LG location), fine-mesh PMTs are employed for their magnetic field tolerance.

Figure 2.18(a) shows the lead-glass calorimeter installed inside the FM magnet. Each module is segmented into 38 lead-glass blocks, each coupled to a photomultiplier tube. To prevent gain degradation of the PMTs under high-rate conditions, the calorimeter is segmented such that the single rate per channel remains below 1 MHz. Figure 2.18(b) shows a cross-sectional view of an LG module. To suppress signals from background pions, the photocathode of the PMTs are parallel to the particle-incidence direction.

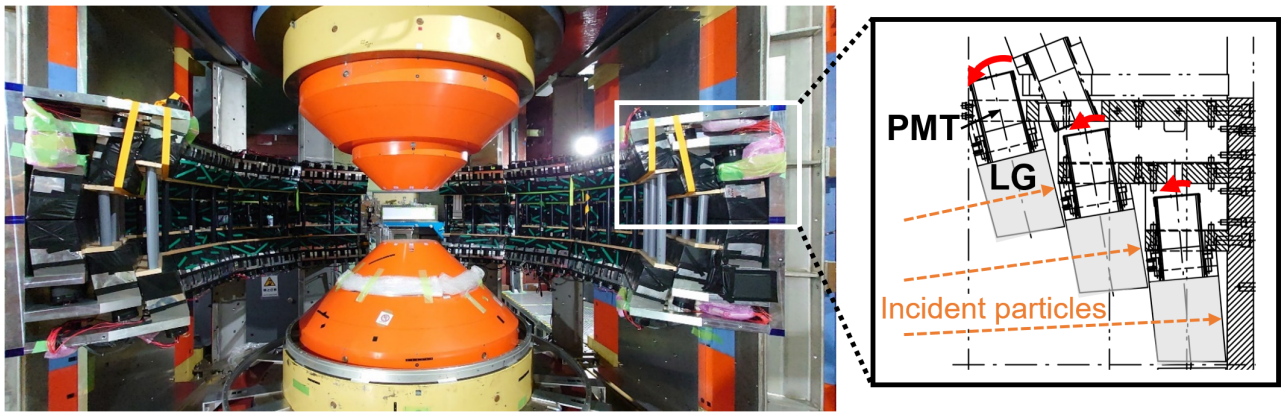

Figure 2.18: (a) Photograph of the LG calorimeter installed in the FM magnet. (b) Vertical cross-sectional view of the LG module.

The signals detected by the PMTs are processed by the DRS4QDC module [42]. The DRS4QDC module is powered through a KEK-VME crate and accepts 16 input channels. The input signals are stored for up to 2 μs in the analog memory of the DRS4 chip after amplification and shaping, and subsequently digitized. The data are then transferred to a PC via SiTCP[48] at 100 Mbps. In addition, the amplified signals are divided and sent to comparators to generate discriminator outputs. As described in Sec. 2.5.1, the LG signals are used as triggers in the E16 experiment, and these discriminator outputs are sent to the trigger electronics for generating triggers.

The DRS4 chip, developed at the Paul Scherrer Institute (PSI), contains eight channels of high-speed switched-capacitor arrays with 1024 cells each. In the DRS4QDC module, two channels are cascaded for a maximum depth of 2048 cells, which are sampled at 960 MHz. This sampling rate is sufficient to record the fast PMT signals, whose time resolution is much higher than that of gas detectors (GTR and HBD). In the present data-taking period, 200 ADC cells around the trigger timing were recorded. Although this window is relatively wide, the overall busy time of the system was dominated by other front-end electronics in this measurement, leaving sufficient margin in the processing time of the DRS4.

2.5 Trigger

2.5.1 Trigger Logic

As trigger signals, the E16 uses the signals from the electron-identification detectors HBD and LG, as well as the signals from the outermost chamber of the three-layer GTR. This is because the STS and the inner GTR layers are expected to suffer from large single rates caused by the beam halo and therefore will not be effective for electron-track selection at the trigger level.

The concept of the trigger conditions is as follows:

- Timing coincidence and coarse position matching among the GTR, HBD, and LG trigger signals are required to construct an "online track."
- Two or more online tracks are constructed, and a opening angle between them is large.
- A multiplicity veto is applied to suppress events during instantaneous high-intensity beam (as mentioned in Sec. 2.2).

The main backgrounds for the vector-meson dielectron decays are electron pairs from the gamma conversions following π^0 decays, as well as π^0 Dalitz decays. Since the opening angles of these electron pairs are smaller than those from vector-meson decays, they are rejected by the second condition above.

As described earlier, the DRS4QDC modules used for LG readout provide discriminator outputs, which are directly used for the trigger. The APV25 system used for GTR and HBD readout does not provide trigger outputs. Moreover, unlike the LG, both the GTR and HBD have many readout channels, making it difficult to construct online tracks within the limited buffering time when we use the strip or pad redout for trigger decision. Therefore, in the E16 experiment, signals induced on the electrodes of the bottom side of the bottom GEM (the final amplification stage) are used as trigger signals, independently of the readout strips or pads. Figure 2.19 shows the segmentation of the trigger signals for one module of the GTR, HBD, and LG. The GTR is divided into 24 segments in the vertical direction, the HBD into 36 segments, and the LG uses the same segmentation as its readout channels.

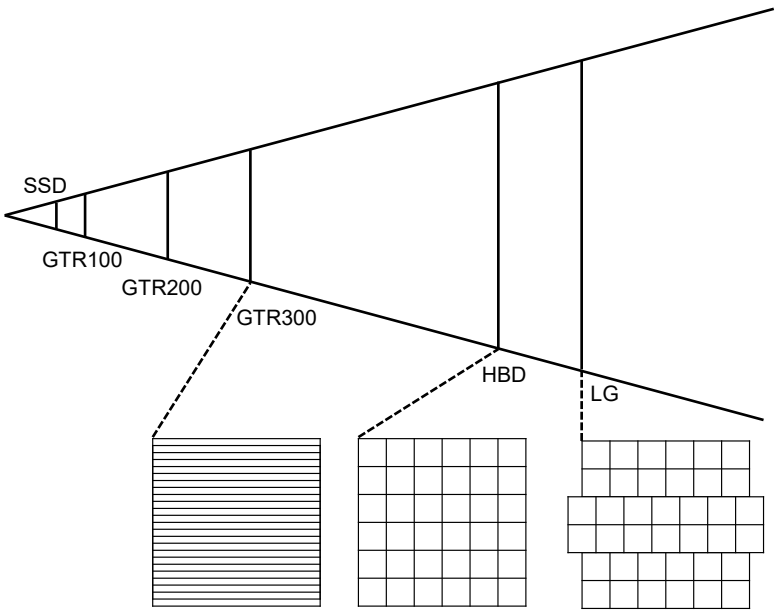

Figure 2.19: Schematic view of the trigger segments in each trigger detectors.

The opening angle of an online track pair is calculated from the relative positions of their LG trigger channels. One-channel distance corresponds to an opening angle of approximately 5 degrees. In the present data-taking period, the horizontal channel difference was defined as x [ch] and the vertical difference as y [ch], and events satisfying $x^2 + y^2 > 75$ were selected.

For the multiplicity veto, the trigger signals from the GTR were used. This choice was made to ensure a stable reference during long-term operation, as the thresholds of the electron-identification detectors could be adjusted frequently to optimize their efficiencies. The multiplicity is determined by counting the number of GTR trigger hits among all eight modules that fall within the coincidence window. A veto is applied to events with multiplicity > 15.

2.5.2 Trigger Electronics

The trigger signals of the GTR and HBD are read out from the electrodes on the bottom side of the bottom GEM via AC coupling. For this purpose, Amplifier-Shaper-Discriminator (ASD) boards are developed for the GTR and HBD, respectively. For both detectors, the trigger signals are obtained through a different path from the readout signals. When the induced signal is read out from the bottom electrode of the GEM, the detector capacitance between the top and bottom GEM electrodes must be taken into account, unlike the case of strip or pad readout. This additional capacitance degrades the S/N ratio and consequently affects the trigger efficiency.

To determine the trigger based on the conditions described in the previous section, the Universal Trigger Board 3 (UT3), a general-purpose trigger logic module developed for Belle II, is employed. The trigger generated by the UT3 is distributed to each front-end electronics through the Frontend Timing SWitch (FTSW), also developed for Belle II.

All discriminator outputs from E16 detectors amount to 792 channels across eight modules. To deal with them, a dedicated Trigger Merging Module (TRG-MRG) [49] was developed for the E16 experiment to aggregate these signals and transmit them to the UT3. The TRG-MRG converts 256 channels of discriminator signals into serial data, converts them to optical signals, and sends them to the UT3 via optical fibers. It also functions as a TDC by detecting the rising edges of the discriminator signals. In addition, it serves as scaler information to count the number of hits in each channel.

Figure 2.20 summarizes the overall structure of the trigger system.

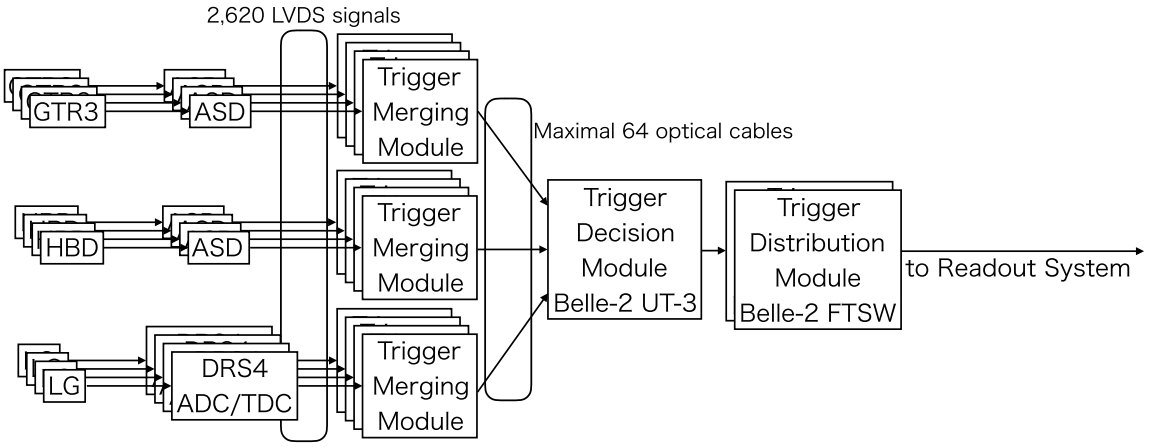

Figure 2.20: Schematic diagram of the E16 trigger system.

2.6 Data Acquisition System (DAQ)

An overview of the entire DAQ system of the E16 experiment, including the trigger system, is shown in Fig. 2.21. In the present data-taking period, online-event building for all detectors was not performed. DAQ processes to handle the data flow for four-types of front-end (SRS/STS/DRS4 and TRG) are run independently, while the common trigger signal was used in the data-taking run. TRG-DAQ collects the data from TRG-MRG and UT3 and wrote to a disk on a PC, after the event-build.

All DAQ systems operate using a common trigger signal: the trigger generated by the UT3 is distributed to each front-end modules by the B2TT protocol, with "trigger-tag" information which includes time stamp and trigger ID to help the event building. The trigger signal is distributed via the FTSW module and giga-bit Ethernet to the GBTxEMU, the SRS, and the RPV260. And from RPV260 to DRS4 modules via VME bus. The TRG-DAQ records the TRG-MRG output and the UT3 output with online-event building. Figure 2.22 shows the online monitor of the TRG-DAQ system.

The SRS-DAQ operated on two separate DAQ PCs. The GTR and HBD data were sent to different PCs, where event building was performed independently. To avoid bottlenecks from data writing, three data-writing processes for HBD and six for GTR were operated simultaneously using different disks.

For the LG data, 22 DRS4QDC modules were used in total, and DRS4-DAQ processes were operated for each modules without event building.

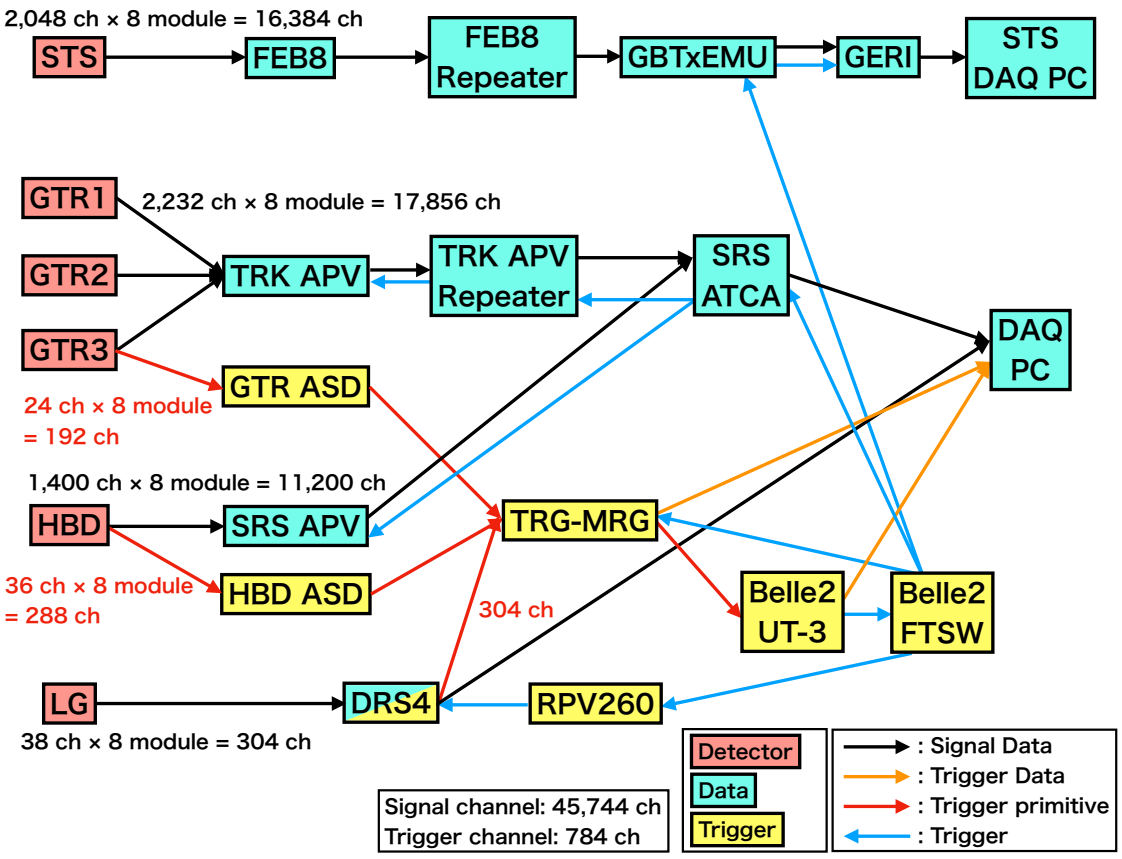

Figure 2.21: Schematic diagram of the E16 DAQ system. Data flow including trigger system are shown. Number of channels shown are for the eight module configuration.

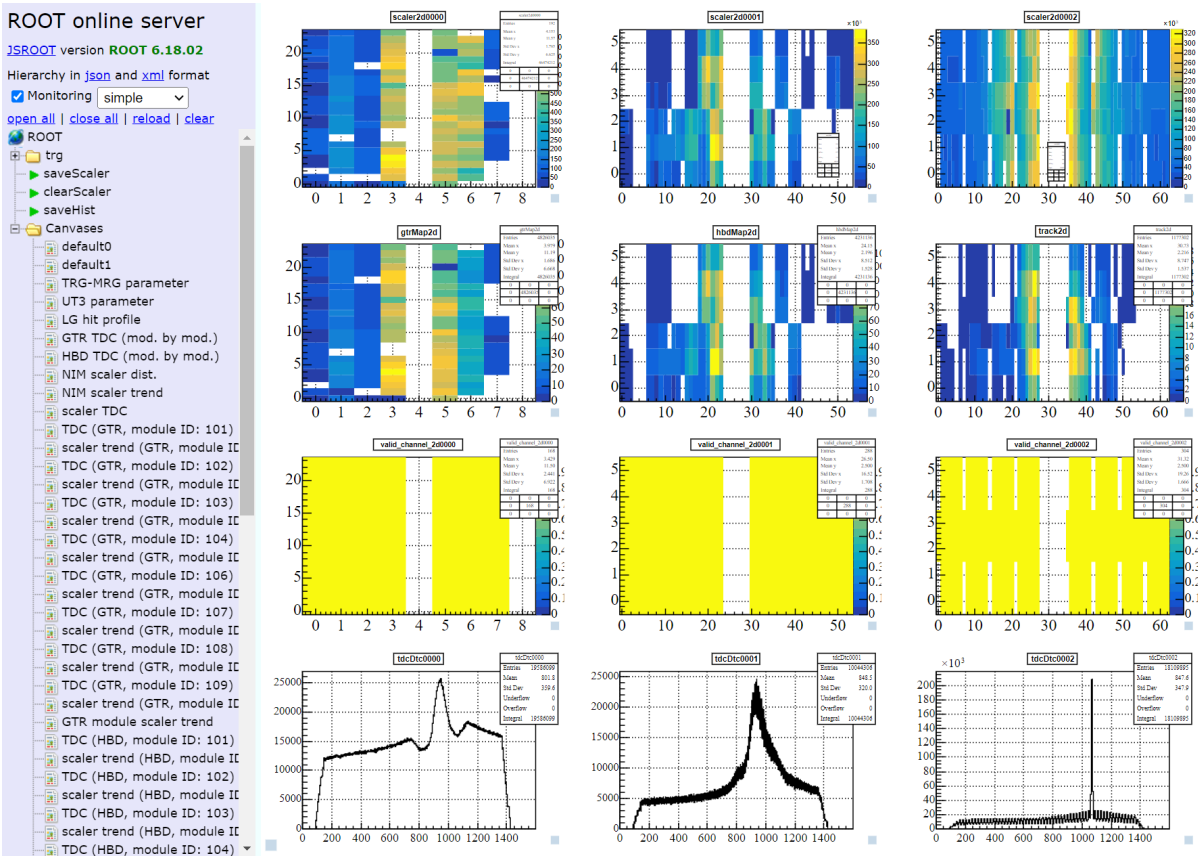

Figure 2.22: The online monitor of the TRG-DAQ system is shown. The columns, from left to right, correspond to the GTR, HBD, and LG. The rows, from top to bottom, display the hit profile per spill, the hit profile participating trigger in the run, the alive channels, and the TDC distributions.

Chapter 3

Analysis

3.1 Analysis Overview and Notations

Analysis overview is summarized in this section. First, Sec. 3.2 describes the available detector regions used in this analysis. Next, Sec. 3.3 explains the calibration method of each detector, and Sec. 3.4 explains the procedure of track reconstruction using the calibrated signals. The evaluation of all efficiencies required for the cross-section measurement is summarized in Sec. 3.5. Finally, Sec. 3.6 evaluates the number of beam protons related to the obtained data used in this analysis.

In the analysis, in addition to the position information in the laboratory coordinate system ("global position"), the position information on each detection plane ("local position") is used, especially for tracking. In the local coordinate system, the y-axis is defined vertically, the x-axis horizontally, and the z-axis perpendicular to the detection plane. These axes is shown in Fig. 3.1.

As explained in the next section, only a limited detector acceptance is used in this measurement. Figure 3.1 also shows the module names and their positions.

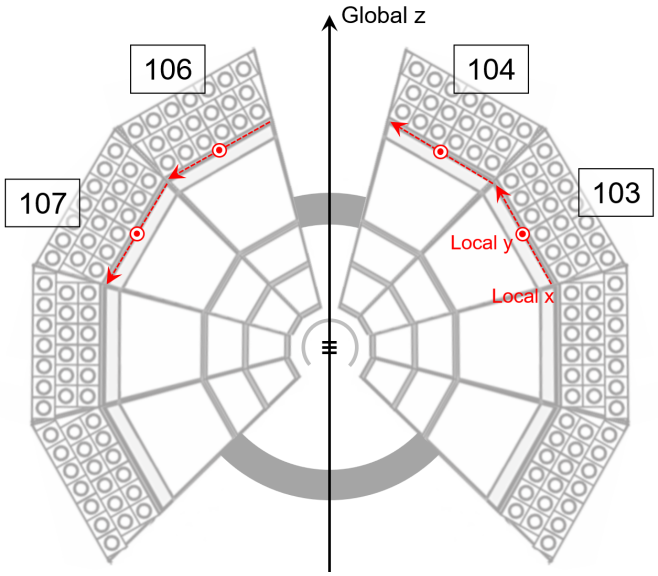

Figure 3.1: The black arrow indicates the global coordinate system, and the red dashed arrow indicates the local coordinate system. Correspondence between module ID and detector position is also shown.

3.2 Acceptance Applied in the Analysis

Although the eight modules were constructed in the E16 spectrometer, the four forward modules, where most of the produced ϕ mesons are detected, were used in this analysis. With the direction of the magnet field used in this measurement, positively charged particles bend to the left from the top view and negatively charged particles bend to the right.

Since the produced particles are Lorentz-boosted in the laboratory frame, positively charged particles predominantly enter the detector acceptance on the left side of the beam direction, while negatively charged particles enter the right side. In this analysis, in order to reduce systematic uncertainties in the calibration, the cross-section evaluation was performed only for events in which positrons enter the detector acceptance on the left side of the beam direction and electrons enter on the right side. According to the simulation described in Sec. 3.5.2.5, 87% of the ϕ mesons detected at the constructed acceptance satisfy this condition, so the impact of this requirement on statistics is small.

In addition, some parts of the detectors were not functioning properly. The major dead regions are as follows:

- The STS module 103 was unusable due to control issues.
- At the GTR 300 layer, module 107 could not be operated with sufficient high voltage because many GEM strips had electrical shorts between the top and bottom electrodes of the GEM.
- In the HBD, one–quarter of module 104 and half of modules 103 and 107 could not be operated with sufficient high voltage due to the electrical shorts, as summarized in Fig. 3.2.

Among these, GTR–300 and the HBD were used as trigger detectors. Since the trigger efficiency in the above regions was extremely low, they were excluded from this analysis.

As mentioned earlier, only positively charged tracks are used on the left-side detector acceptance (modules 106 and 107). For module 107, excluding the GTR300 layer results in very few tracks entering the other tracking detectors (STS, GTR100, GTR200), therefore module 107 is not used for the tracking in this analysis, whereas tracks that enter GTR300 of module 106 and then enter the HBD of module 107 are included. The issue of the missing STS module 103 was handled by not requiring STS hits for track reconstruction near module 103 in the offline analysis.

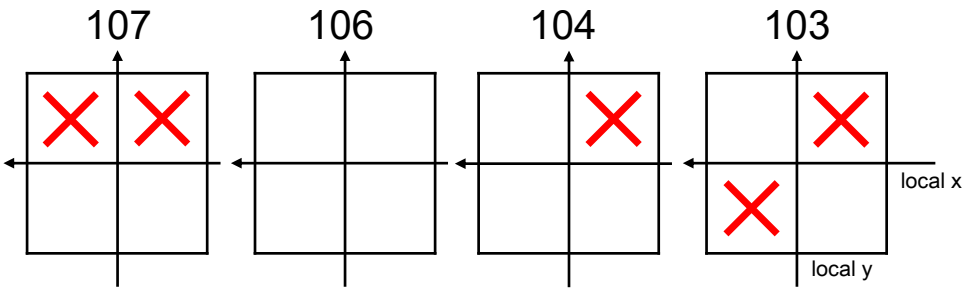

Figure 3.2: Dead region of the HBD on each module. Cross mark means the dead region due to the dead GEM stack.

3.3 Calibration

The waveform information of the GTR, HBD, and LG are recorded, while the ADC and TDC information of the STS are recorded. The hit position information from the STS and GTR is used to determine particle trajectories and momenta (tracking). In addition, the hit position and pulse height information from the LG and HBD are used for electron track selection. In this section, the procedure for converting the recorded waveform, ADC, and TDC information of each detector into the hit position, pulse height, and timing information is described.

3.3.1 STS

In the STS, each module has 1024 strips along the local x-axis with a pitch of 58 μm. Each strip records 320 MHz TDC samples (1 tick = 3.125 ns) and charge information from 0–14 fC using a 5-bit ADC. In this detector, typical track makes a few strip hits, not a single strip hit, depending on the incident angle of the track. These hits were clustered under the conditions that the hits occur on adjacent strips and that the timing difference between hits is within 60 ticks (=187.5 ns). Figure 3.3 shows the hit and cluster timings of the STS. The applied range of cluster timing, $-110 < t < -75$ tick, is also shown as the dotted lines. The cluster position is determined as the ADC-weighted average of the strip hit positions. The total cluster charge is obtained as the sum of the ADC values of the strip hits.

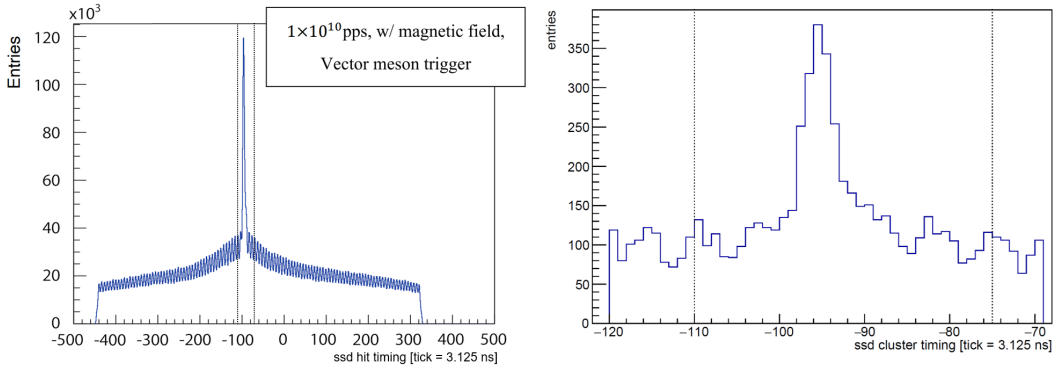

Figure 3.3: Left panel shows the timing distribution of the STS hit, and right panel shows that of the STS cluster. The vertical lines indicate the range of cluster timings used in the analysis.

3.3.2 GTR

Each of the three GTR layers has readout strips with pitches of 350 μm in the local x direction and 1.4 mm in the local y direction. The signals from the six layers (GTR100x, GTR100y, GTR200x, GTR200y, GTR300x, GTR300y) are processed by the ASIC APV25. Fifteen waveform samples, corresponding to a total duration of 480 ns, are recorded at a sampling rate of 31.25 MHz, which gives 32 ns per sample. In GTR, typical tracks make a few strip-hits, not a single strip hit, depending on the incident angle. Clustering is performed for each of the six layers. Figure 3.4(a) shows a typical GTR signal (waveform spanning multiple adjacent strips).

The baseline offset in ADC has already been subtracted in the figure. The baseline is determined by averaging 0th, 1st and 2nd samples out of the 15 samples of waveform for each strip by APV25 chip, described in Sec. 2.4.3. The cluster position on each plane is determined by the center of gravity (COG) of pulse heights for strips in the cluster. The cluster timing is defined as the time when the summed waveform of all strips in the cluster reaches half of its maximum value.

Although Fig. 3.4(a) shows a typical GTR cluster response, in the realistic data, cases where two clusters overlap, as shown in Fig. 3.4(b), were also observed. Therefore, pulse-shape fitting is applied to determine the timing of overlapping clusters.

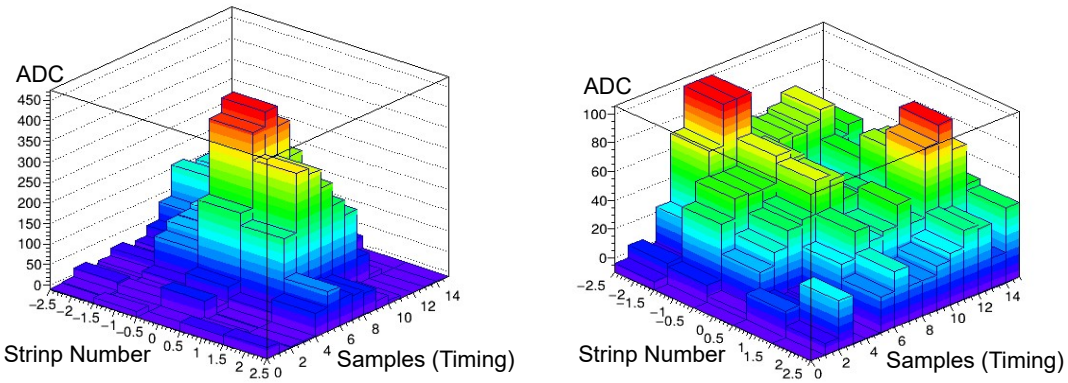

Figure 3.4: (a) Typical cluster waveform detected by the GTR. (b) Waveform where two clusters overlap.

The COG cluster positions correspond to the positions on the strip plane. However, to achieve good mass resolution, the drift of ionization electrons must be taken into account. Figure 3.5 illustrates the process until the signal is detected on the strip. The incident charged particle produces ionization electrons in the region between the mesh electrode and the top GEM electrode (the "drift gap"). These electrons drift toward the GEM due to the electric field applied in the drift gap, are amplified, and are then detected on the strips. During this process, the electrons experience Lorentz force due to the magnetic field applied in the spectrometer. The center of the drift gap is defined as the detection plane, and the cross point of the incident electron track on this plane is defined as the "cluster position" in the GTR. The cluster position x is expressed using the COG position x' on the strip plane as

$$\begin{aligned} x &= x' + \Delta x_{tr} + \Delta x_L + l_{const} && (3.1)\\ &= x' + \Delta z \tan\theta_{in} + \Delta z \tan\theta_L + l_{const} && (3.2)\\ &= x' + v_d(t - t_0)\tan\theta_{in} + v_d(t - t_0)\tan\theta_L + l_{const}. && (3.3) \end{aligned}$$

Here, v_d is the drift velocity of ionization electrons in the drift gap, t_0 is the cluster timing when ionization electrons are generated just on the detection plane, l_{const} is the drift distance in the local x direction by the Lorentz force, θ_L is the Lorentz angle, and θ_{in} is the incident angle of the particle relative to the detection plane. To determine the position x on the detection plane, the strip-plane position x' (the COG cluster position) must be corrected using the four parameters v_d, θ_L, t_0, and l_{const}.

In principle, v_d is determined by the electric field and the type of gas in the drift gap, θ_L and l_{const} by the GTR chamber structure and magnetic field, and t_0 by the chamber structure and circuit latency. However, in the present measurement, the mechanical support of the GTR was not robust to reduce material budget, resulting in distortions of the chamber. These distortions significantly affect this corrections depending on the local x and y positions. Therefore, for l_{const} and t_0, corrections depending on module, layer, and local x and y positions are introduced. The parameters v_d and θ_L are determined for each module and layer.

The GTR calibration procedure includes geometry correction and determination of these four parameters. First, straight tracks are reconstructed using data taken without magnetic field, and the chamber geometry is corrected accordingly. The correction considers shifts in local x, y, z directions and rotations around the local x, y, z axes for each GTR chamber (three

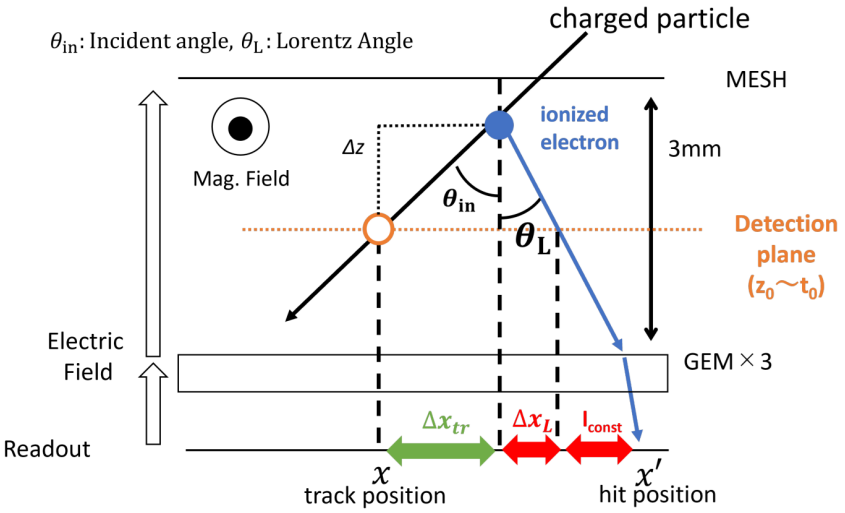

Figure 3.5: Detection principle of the GTR. The relation between the position observed on the GTR strip plane (x') and the position on the detection plane (x) is shown.

modules, three layers). Dedicated data were taken for the geometry correction: the proton beam was directed not at the experimental target but at the wire shown in Fig. 3.6. The tungsten wire has a diameter of 100 µm, allowing the reaction point to be localized. Straight tracks are reconstructed using the wire and the innermost tracker STS. The chamber positions are corrected so that the COG residuals of the GTR layers from each of the four wires show no position dependence. The relative alignment accuracy between the wire and STS is better than the GTR installation accuracy, but it still contributes to the final uncertainty. The impact of this uncertainty on the reconstructed mass spectrum is discussed in Sec. 4.1.3.

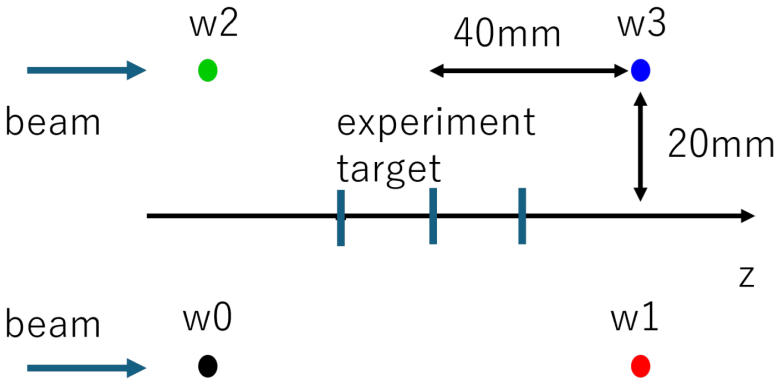

Figure 3.6: Global positions of the experimental target and the wire target.

For track reconstruction without magnetic field, Eq. 3.1 is modified as

$$x = x' + v_d(t - t_0)\tan\theta_{in}. \tag{3.4}$$

The correction $\Delta x = x - x'$ corresponds to the residual between the COG cluster position and the projection point of the reconstructed track using the other three layers. Using the residual, the cluster timing and incident angle of the track, v_d can be determined. Although drift velocity can be estimated from gas properties and applied voltage, in this analysis the realistic v_d obtained from this method is used.

The Lorentz parameters are determined using data taken with normal and inverse magnetic fields. From Eq. 3.1, the time-dependent factor of the correction $\Delta x = x - x'$ under magnetic field is

$$\Delta x = v_d(t - t_0)(\tan\theta_{in} + \tan\theta_L). \tag{3.5}$$

When the magnetic field direction is reversed, only the sign of θ_L changes. Therefore, by determining this coefficient for both field directions, θ_L can be extracted.

The parameters l_{const} and t_0 are determined with local position dependence. The calibrated layer is divided into 10 segments in local x and 10 segments in local y, and Δx is evaluated in each segment. After applying the previous corrections, the only remaining difference between normal and inverse magnetic field data is l_{const}, so

$$\Delta x(\text{normal-field}) - \Delta x(\text{inverse-field}) = 2 \times l_{const}. \tag{3.6}$$

From this, l_{const} is determined as a function of local x and local y. The dependence of t_0 appears through θ_{in}. Since the sign of θ_{in} correlates with the particle charge, t_0 is determined by requiring $\Delta x = 0$ for both positively and negatively charged tracks. In summary, l_{const} and t_0 are determined using the following four types of tracks, with dependence on local x and local y:

- Positively charged particles under normal magnetic field
- Negatively charged particles under normal magnetic field
- Positively charged particles under inverse magnetic field
- Negatively charged particles under inverse magnetic field

Figure 3.7 shows the calibration status after applying the position-dependent correction on the GTR detection plane. As an example, the results for module 104 of the GTR200 layer are presented. Successful calibration performs across a wide region, except near the edges where chamber deformation is likely to occur. The variations of the residual mean within each layer were examined for all layers. The standard deviations were found to be 50 μm for the GTR100 layer, 75 μm for the GTR200 layer, and 150 μm for the GTR300 layer, for the 104 and 106 modules. The larger variations observed in the outer layers arise from the reduced accuracy of the track extrapolation, which becomes particularly pronounced in the outermost layer.

3.3.3 HBD

The waveform information of the HBD is recorded by the same frontend module as the GTR, with 31.25 MHz sampling and 15 samples. The baseline is determined as the average of samples 0–2. The waveform is fitted using the following function with a circuit time constant τ:

$$f(t) = A\frac{t - (T_{\text{peak}} - \tau)}{\tau}\exp\left[1 - \frac{t - (T_{\text{peak}} - \tau)}{\tau}\right], \tag{3.7}$$

where A represents the pulse height and T_{peak} corresponds to the timing at which the waveform reaches its maximum. The time constant τ is fixed at 52 ns in the fit. The parameters obtained from the fit are used as the ADC value and timing of the HBD hit. If two peaks are found within the 15 samples, the waveform is fitted with a two-pulse function. Here, a "peak" is defined as a local maximum, where the ADC value increases from one sample to the next and then decreases in the following sample. The efficiency of this waveform analysis was evaluated using an eye-scan and confirmed to be above 99%.

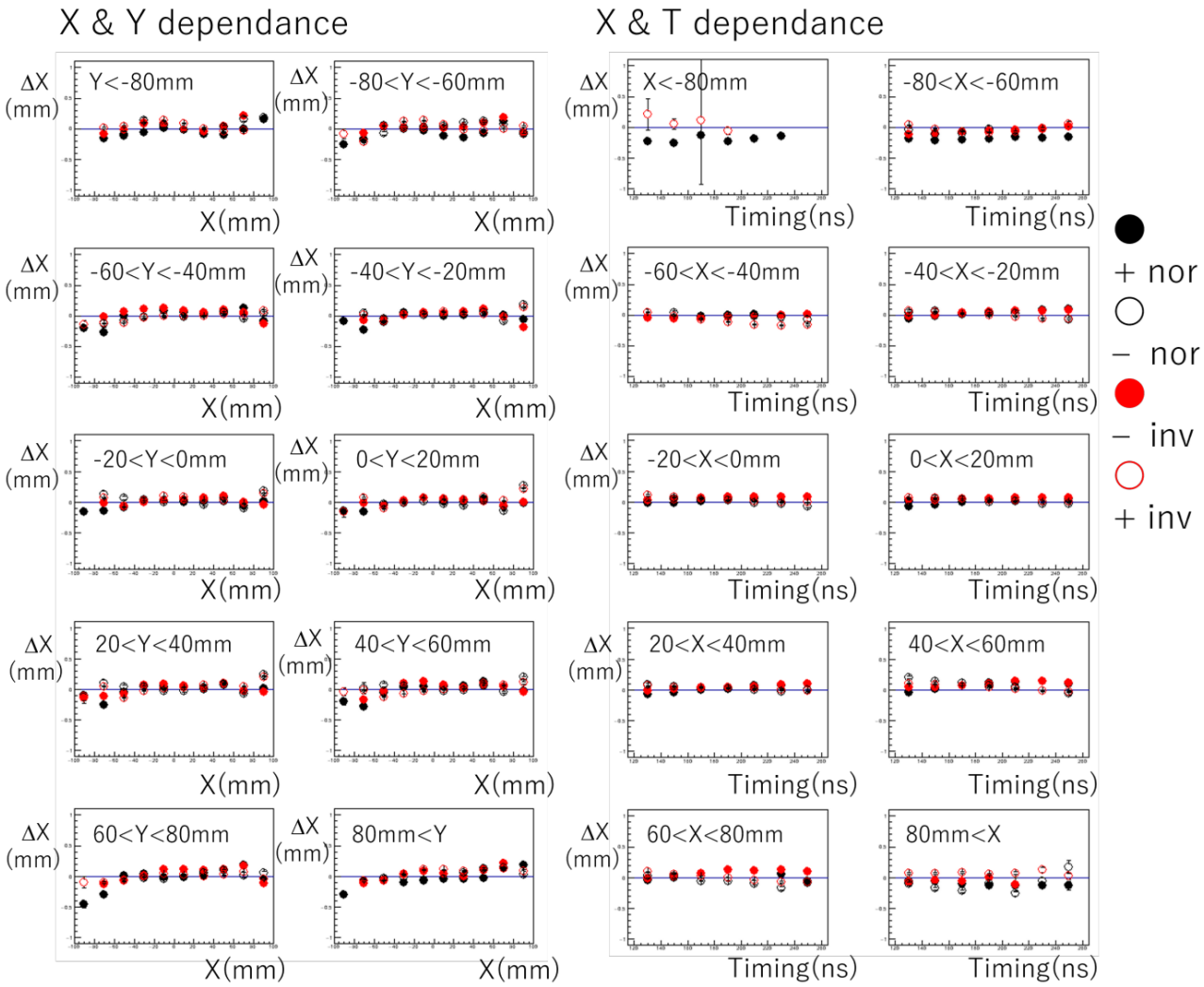

Figure 3.7: Calibration status after applying the position-dependent correction. Results for the GTR200 layer of module 104 are shown. Each panel shows the mean residual: the left ten panels as a function of local x for each local y bin, and the right ten panels as a function of cluster timing for each local x bin. Filled black, open black, filled red, and open red points represent positive/negative charges in the normal field and negative/positive charges in the inverse field, respectively.

The obtained ADC values were converted into the number of detected Cherenkov photons. The number of electrons amplified by the GEM is known to follow the Polya distribution:

$$P(q) = C\frac{(1+\theta)^{(1+\theta)}}{\Gamma(1+\theta)}\left(\frac{q}{\bar{q}}\right)^{\theta}\exp\left[-(1+\theta)\frac{q}{\bar{q}}\right], \tag{3.8}$$

where q is the gain, $\bar{q}$ is the mean gain, and θ is the Polya parameter. This implies that the exponential term dominates in the low-ADC region. Assuming that this low-ADC region corresponds to single-photon detection ($1/q \sim 1$), the mean gain $\bar{q}$ is obtained from the inverse slope S^{-1} of the exponential component:

$$\bar{q} = S^{-1}(1+\theta). \tag{3.9}$$

The source of these single photons is considered to be scintillation light emitted by charged particles traveling through CF_4 [44].

Figure 3.8(b) shows a typical HBD hit profile in this measurement, using module 104 as an example. The left side of the figure corresponds to the forward direction, and the right side

to the backward direction. In a typical fixed-target experiment, more particles are expected to enter the forward acceptance due to Lorentz boost. However, the hit profile in Fig. 3.8(b) shows a different trend, which is attributed to non-uniformity in the GEM gain. Typical ADC distributions for high-rate and low-rate channels are shown in Fig. 3.8(a). The red histogram shows the ADC distribution of the HBD, while the blue histogram shows the pedestal distribution. The data was obtained when the HBD signals were not included in the trigger conditions. Following Eq. 3.9, the low-ADC region is fitted with an exponential function, and the gain is extracted from the inverse slope. The Polya parameter θ is set to $\theta = 0.37$, based on previous studies [44][50]. The uncertainty of this parameter affects only the absolute gain calibration and does not influence the accuracy of the relative gain correction used later for efficiency evaluation.

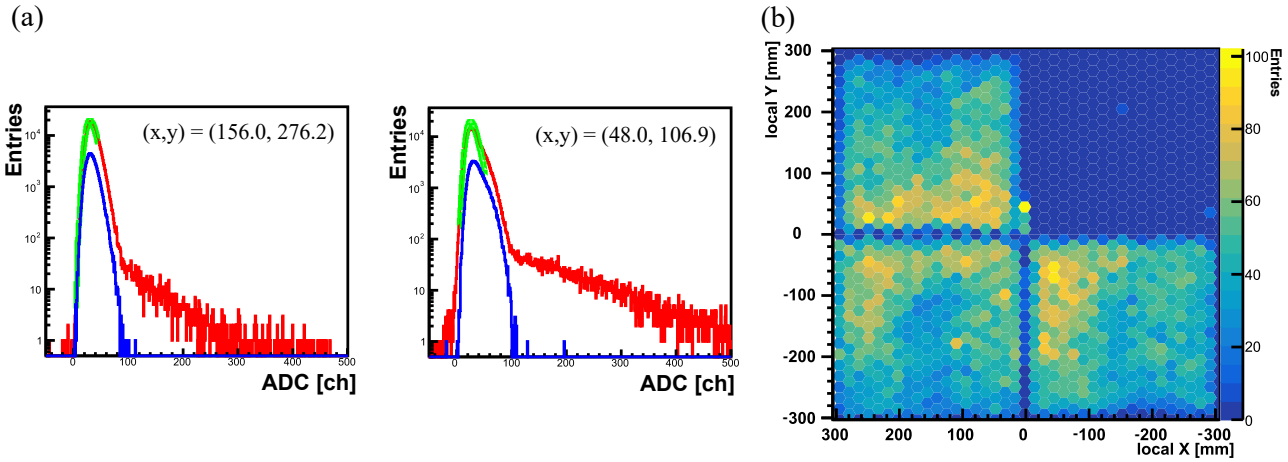

Figure 3.8: (a) Typical ADC distribution of the HBD. (b) Typical hit profile of module 104 of the HBD.

The corrected signals from each channel are clustered by grouping hits on adjacent pads. The cluster ADC value and the cluster size are used for electron identification (see Sec. 2.4.4). The ADC distribution after gain correction (the distribution of the number of detected Cherenkov photons) is discussed in Sec. 3.5, where the efficiency evaluation is performed, including its channel and run dependence.

3.3.4 LG

The LG signals are amplified by PMTs, and the waveforms are recorded with 960 MHz sampling and 200 samples. Figure 3.9 shows a typical LG waveform. Peak searching is performed within a time window of ±40 ns around the trigger timing. If only one pulse is found, the baseline is calculated using the average of samples 10–60 before the peak. If multiple pulses are detected in the recorded region, template fitting with the corresponding number of pulses is applied to extract the pulse height. Although the efficiency of this waveform analysis decreases for low pulse heights, it exceeds 99% for electrons with energies of 0.3 GeV, ensuring no issue for electron detection in this analysis.

LG clustering is not performed solely from LG hit information. Instead, tracks reconstructed by other detectors are extrapolated to the LG detection plane, and close hits of the extrapolated cross point are grouped into a cluster. Considering the thickness of the lead-glass block, channels within ±21 mm around the reconstructed track are selected as cluster candidates. As a timing requirement, only hits within ±5 ns of the timing of the channel with the highest ADC value in the cluster are included.

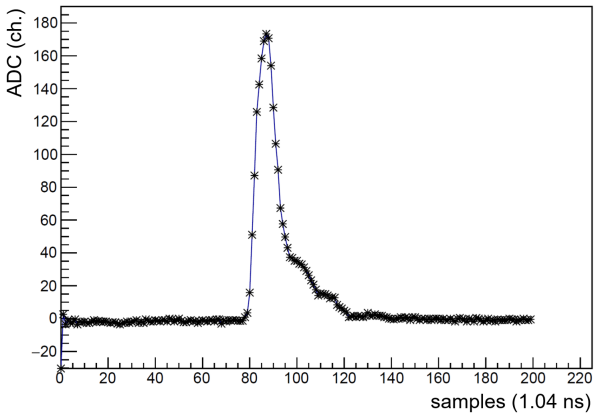

Figure 3.9: Typical LG waveform recorded with DRS4QDC module.

Gain calibration for each LG channel was performed twice: once before data taking and once after. The pre-run gain calibration is important for determining the trigger threshold for electron selection. However, due to time constraints during the beam time, detailed evaluation using tracks reconstructed by GTR and STS could not be performed. Therefore, a simplified gain correction was applied by adjusting the PMT operation voltage so that the mean ADC values of the LG channels are uniform across channels using minimum-bias trigger data.

For the post-run gain calibration, the response of each LG channel to charged particles was examined. Since lead glass has a refractive index of $n = 1.8$, charged particles other than electrons also produce Cherenkov photons, generating signals. Figure 3.10 shows a typical LG response to charged particles. This distribution was obtained using a coincidence trigger from plastic scintillators sandwiching the forward LG channels. The number of Cherenkov photons produced is approximately constant for a given LG thickness, forming a peak as seen in Fig. 3.10.

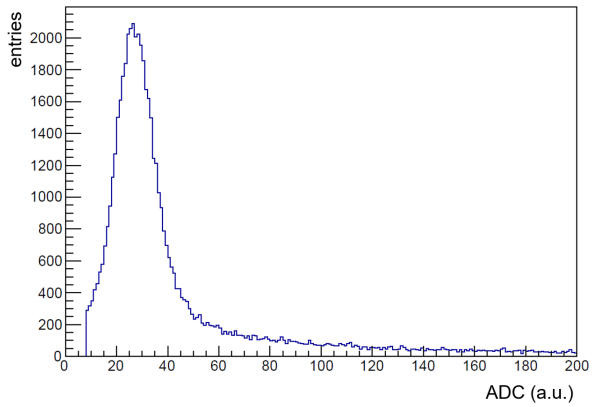

Figure 3.10: LG response to charged particles triggered by two scintillation counters sandwiching the LG block.

Using reconstructed tracks, the LG response to charged particles was examined channel by channel, as shown in Fig. 3.11. Only the results for the right arm (modules 104 and 103) are shown here. The trend of this "pion peak" for each channel is summarized in Fig. 3.12. It was found that the pre-run gain correction had systematic deviations of up to a factor of two. The impact of this on the trigger threshold and trigger efficiency is evaluated in Sec. 3.5.

Finally, a detailed gain calibration was performed using electron samples selected by the HBD. Since the LG is a calorimeter, the pulse height depends on the energy of the incident particle. Test experiments confirmed that the LG response is linear for electrons up to 4 GeV/c. Therefore, dividing the LG ADC value by the momentum of the incident particle

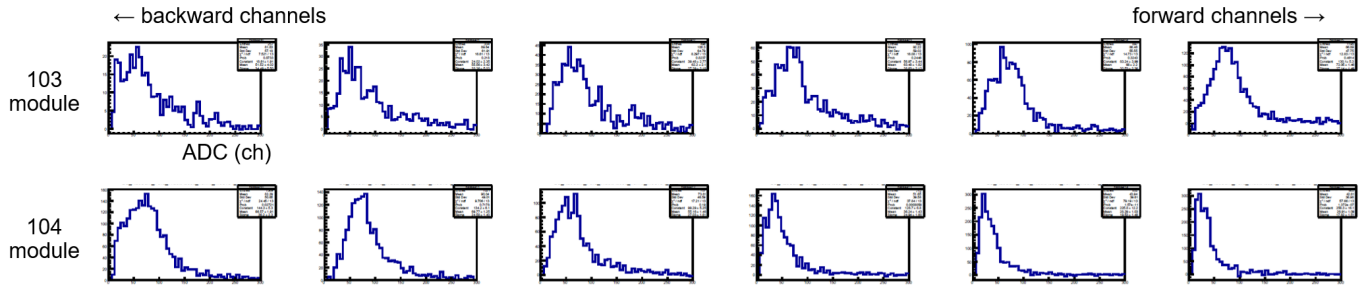

Figure 3.11: LG response to charged particles detected by the GTR and STS. The distribution is the sum of six vertically aligned channels.

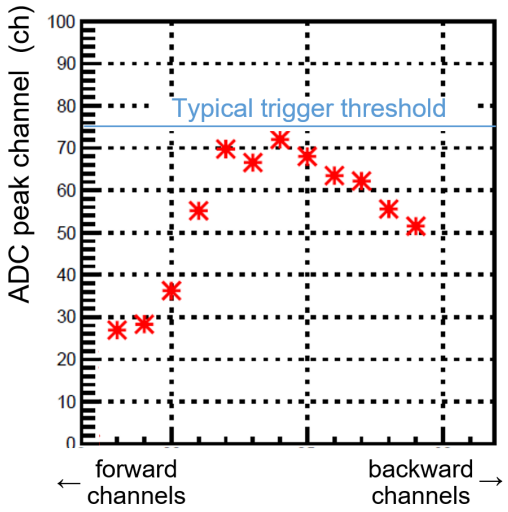

Figure 3.12: Mean values obtained by Gaussian fits to the distribution in Fig. 3.11, shown for each channel. The blue line indicates a typical trigger threshold.

(Energy-over-momentum, E/p) yields a distribution centered around a constant value, with a width determined by the energy resolution. Figure 3.13 shows the E/p distributions for each LG channel. The black histogram represents electron samples selected by the HBD, while the red histogram represents charged particles without HBD selection. The clustering method described earlier is applied. The conversion factor from ADC to energy is determined so that the E/p peak becomes 1 for each channel.

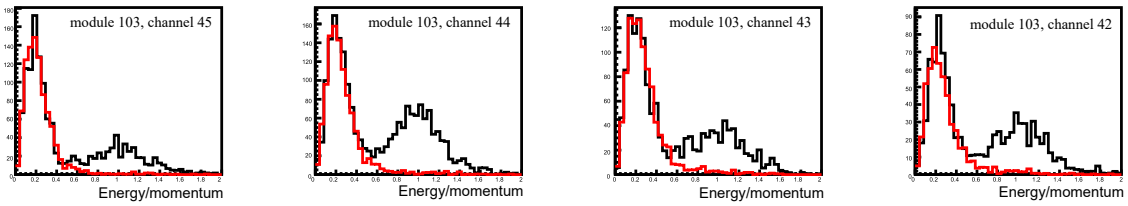

Figure 3.13: E/p distributions for each LG channel. Black: electron samples selected by HBD. Misidentified pions are seen with electrons. Red: charged particles detected by GTR and STS without HBD selection.

Figure 3.14 shows the corrected E/p distribution for all LG channels used in this analysis. The dashed line indicates the cut range adopted for electron identification. Events above this threshold are identified as electrons.

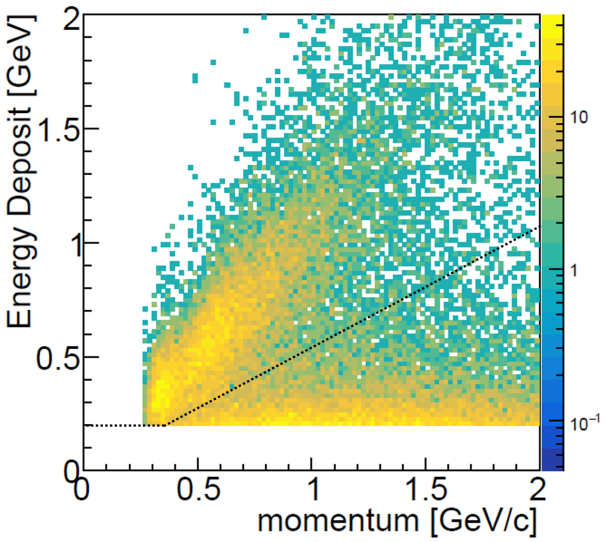

Figure 3.14: Corrected energy–momentum correlation (E/p) for all LG channels used in this analysis.

3.4 Event Reconstruction

In this section, the procedure for selecting electron–positron tracks and reconstructing the invariant mass using the information obtained in Sec. 3.3 is described. The procedure is divided into the following four steps, which are explained in detail in each subsection.

1. Reconstruct single tracks by applying the Runge–Kutta fitting method to the hit positions of the tracking detectors (STS and GTR).

2. Require matching between the reconstructed tracks from step 1 and the signals from the electron identification detectors. This selects electron candidates and positron candidates.

3. Form all possible combinations of electron and positron candidates selected in step 2, and perform Runge–Kutta fitting again under the requirement that the two tracks originate from the same vertex. Based on the reconstructed vertex position, determine which of the three targets the pA reaction occurred in.

4. Perform Runge–Kutta fitting again under the requirement that the two tracks originate from the target position determined in step 3, and determine the momenta of the two tracks and the invariant mass derived from them.

3.4.1 Selection of Track Candidate

Tracking is performed using information from seven layers: the x strips of the STS, GTR100, GTR200, and GTR300, and y strips of GTR100, GTR200, and GTR300. First, using the cluster information from the four layers in the local x direction (STS, GTR100, GTR200, GTR300), all combinations of clusters belonging to the same module or adjacent modules are taken to form "x track candidates." As mentioned in Sec. 3.2, STS module 103 was not used in this analysis, so x track candidates passing through GTR100 module 103, GTR200 modules 104 and 103, and GTR300 modules 104 and 103 are also constructed. For the local y direction, "y track candidates" are constructed using cluster information from GTR100, GTR200, and GTR300. As shown in Sec. 3.5.2.2, some y strips had low detection efficiency due to noise, so even if one of the three GTR layers does not have a cluster, the candidate is still kept as a y track candidate.

For these track candidates, a quadratic fit is applied to the global coordinates of the x track candidates, and a linear fit is applied to the y track candidates. Candidates that do not satisfy the fit conditions are discarded (rough track selection). The target position is included in the fit. For each x track candidate, fitting is performed three times, once for each of the three targets, and each fit is evaluated. For the remaining track candidates, the tracks are extrapolated to the HBD detection plane, and only those with an HBD cluster near the extrapolated position are kept. At this stage, the extrapolation accuracy in the local x direction is not high, so the association requirement is loose: the residual between the projection point and the HBD cluster must be within 95 mm in x and within 20 mm in y.

For the remaining track candidates, combinations of x and y candidates are formed, and Runge–Kutta fitting is applied to reconstruct three-dimensional tracks. As in rough track selection, the target position is also taken into account in the Runge–Kutta fitting. The global z position of the target is fixed to the three experimental target positions ($z = +20, 0, -20$ mm), respectively. Finally, only tracks with a reduced χ^2 less than 6 in the Runge–Kutta fitting are kept for the next step.

If the number of x/y track candidates is large, the number of Runge–Kutta fits becomes enormous and exceeds realistic CPU time. Therefore, for events with too many candidates, the cluster selection conditions are tightened to reduce the number of candidates. Specifically, if more than 150 track candidates include a particular STS cluster, the rough track selection conditions are tightened. If more than 150 candidates still remain, the ADC threshold for all GTR layers is raised, and candidates that lose two or more clusters due to this threshold increase are removed. If more than 150 candidates still remain, the waveform selection conditions for GTR clusters are tightened. If more than 150 candidates still remain, the HBD association window is narrowed. If more than 150 candidates still remain, candidates that lose even one GTR cluster when the ADC threshold is raised are removed. For track candidates passing through module 103, where STS clusters are unavailable, the same procedure is applied using GTR100 clusters. By gradually tightening the conditions in this way, track candidates can be selected while minimizing loss of detection efficiency and keeping the CPU time reasonable. The track reconstruction efficiency in this process is evaluated using the embedding method in Sec. 3.5.3.

3.4.2 EID Association

Next, the reconstructed tracks are required to be associated with signals from the electron identification detectors. For the HBD, the track must correspond to a cluster with at least 6 photoelectrons and a cluster size of at least 2. For the LG, clustering is performed using the method described in Sec. 3.3, and the energy deposit must be at least 0.2 GeV and satisfy $E/p > 0.53$.

Figure 3.15 shows the residual distribution between the projection point of reconstructed tracks (from low-intensity beam data) and the HBD cluster position. The distributions for particles with different momenta in modules 104 are shown. The shift of the residual mean from 0 mm and its momentum dependence are attributed to installation accuracy of the HBD. To account for this, a momentum-dependent correction function is introduced for each module. Figure 3.16 shows the correction functions applied to modules 103–107. As mentioned in Sec. 3.2, only negatively charged particles are considered for modules 103 and 104, and only positively charged particles for modules 106 and 107. After correcting the residual mean, the association window is determined as 3.1 sigma in the local x direction and 2.8 sigma in the local y direction, based on Gaussian fits to the residual distributions. These values were chosen considering the signal-to-noise ratio of mass spectrum.

LG association is performed by searching for hits near the cross point of the reconstructed

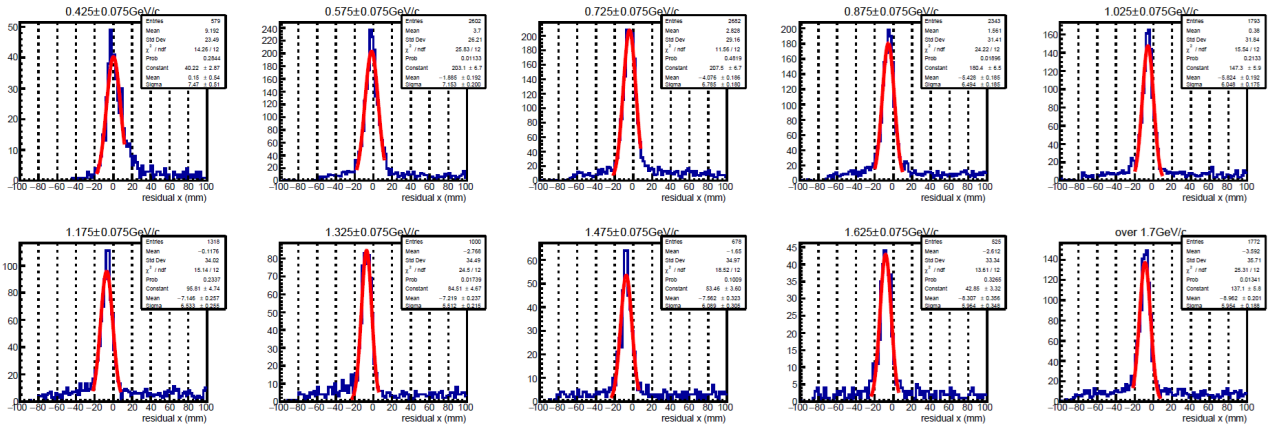

Figure 3.15: Residual distribution in x (horizontal)-direction for HBD module 104.

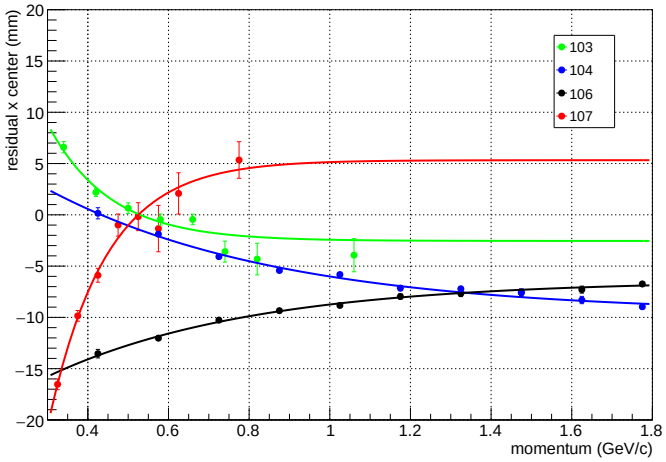

Figure 3.16: Momentum-dependent correction functions for the residual mean for each HBD module. The points show the mean and error obtained from Gaussian fits to the residual distributions for each momentum. The solid lines show the correction functions by exponential function empirically determined to reproduce the data points.

track with the LG detection plane, as described in Sec. 3.3.4, and applying the EID selection to the resulting cluster. The search window is also determined considering the signal-to-noise ratio. Figure 3.17 shows the residual distribution between the LG hit position and the projection point of the track (blue line). The magenta line shows the residual distribution from random associations obtained by event mixing. The green line shows the residual distribution for hits that satisfy the cluster selection criteria. The difference between the blue and magenta histograms (hits correlated with the track) is almost entirely included in the selected clusters. The clustering efficiency is evaluated as an "analysis cut" in Sec. 3.5.3.

For tracks associated with both HBD and LG, cases occur where multiple reconstructed tracks correspond to a single HBD cluster within the same event. Since the probability that two different electrons (or positrons) overlap within one cluster region is extremely low, such cases are interpreted as single-particle tracks that appear as multiple tracks due to accidental combinations with clusters. In this analysis, when multiple tracks are associated with a single HBD cluster, only the track with the smallest chi-square value in the single-track Runge–Kutta fit is kept ("duplicate cut"). However, if the STS clusters used in the single track differ, the tracks are considered to originate from different particles and both are kept. This duplicate cut is applied separately for each of the three targets, and duplicate removal between tracks from

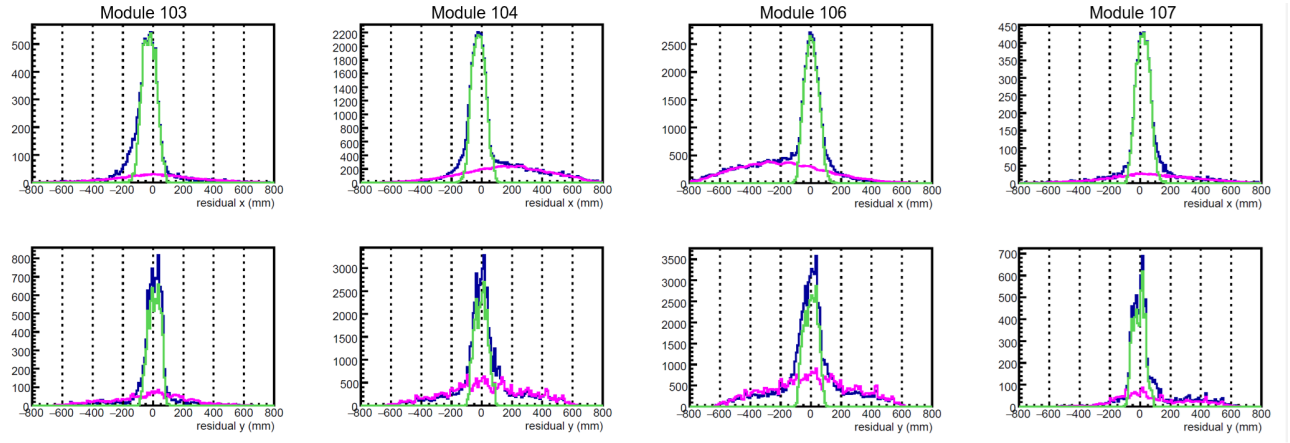

Figure 3.17: Residual distributions for LG modules. The upper panels show the local x direction, and the lower panels show the local y direction.

different targets is not performed at this stage.

Finally, only events in which at least one minus-charge candidate and one plus-charge candidate remain are kept for the next step.

3.4.3 Vertex Determination

All combinations of minus-charge and plus-charge candidates prepared in the previous step are treated as pair candidates. For each pair candidate, a Runge–Kutta fitting is performed under the requirement that the two tracks share a common vertex (pair fitting).

Runge–Kutta fitting is performed by minimizing the following χ^2:

$$\chi^2 = \sum_{N_{\text{layers}}} \left(\frac{r_i^2}{\sigma_i^2} \right) + \frac{(r_x^{\text{target}})^2}{(\sigma_x^{\text{target}})^2} + \frac{(r_y^{\text{target}})^2}{(\sigma_y^{\text{target}})^2}. \tag{3.10}$$

Here, N_{layers} denotes the number of layers used for pair tracking, up to a maximum of 14 ($= 7 + 7$). r_i and σ_i represent the residual and the resolution of the i-th layer, respectively. The global z position of the experimental targets is treated as a free parameter, while the global x and y positions are constrained to the estimated beam center $(x, y) = (-0.5, -0.4)$ with the corresponding weights $(\sigma_x^{\text{target}}, \sigma_y^{\text{target}}) = (2.5, 0.9)$.

Figure 3.18 demonstrates the separation of the three targets. Here, the same chi-square cut of the pair fitting as that applied to the copper targets in the ϕ-meson mass reconstruction is used (the procedure for determining the cut condition is described in Sec. 3.5.3). The distribution of the reconstructed vertex position along the global z direction is shown in Fig. 3.18(a). Figure 3.18(b) shows the correlation between the global z and global x positions. The entries of the histogram shown by the blue line in Fig. 3.18(a) correspond to all entries in Fig. 3.18(b), while the entries of the red histogram in Fig. 3.18(a) correspond to the entries within the inner red-line region in Fig. 3.18(b). By excluding the contamination from pairs obviously originating from different targets, it is confirmed that the three target positions can be separately reconstructed.

The production points of the charged particles are localized around the experimental targets, indicating that the influence of other materials is minimal. The setup around experimental targets is designed to minimize the amount of material: the experimental targets are placed inside a chamber filled with helium and the window of chamber is made by Mylar foils. The window of the beam pipe is located at $z < -230$ mm (outside the range of Fig. 3.18), sufficiently far from the targets.

The production target is determined based on the global z distribution in Fig. 3.18(a): if $z < -10$ mm, the upstream copper target; if -10 mm $\leq z \leq +10$ mm, the carbon target; and if $z > +10$ mm, the downstream copper target. If the fit is performed with an incorrect target position, namely 20 mm away from the correct one, the reconstructed momenta and opening angle change significantly, and the events no longer reconstructed within the ϕ-mass region.This trend is confirmed in simulation: a displacement of 20 mm in the vertex position along the global-z direction corresponds to a shift of more than 400 MeV/c^2 in the mass peak position. Therefore, incorrect determination of the production target does not lead to an incorrect evaluation of the ϕ-meson yield on the carbon and copper targets. The reconstruction efficiency is evaluated in Sec. 3.5.3.

As a remark, the selection criteria for the pair candidates shown in Fig. 3.18 are stricter than those used in the ϕ-meson mass reconstruction. Specifically, the single-track selection criteria (the chi-square cut of the single-track Runge–Kutta fitting and the timing match cut the LG hits for the two tracks) are tightened here. This is solely to demonstrate the vertex-determination performance of the pair fitting by removing fake single tracks and fake pairs as much as possible. In the ϕ-meson mass reconstruction, these conditions are loosened to maximize the yield.

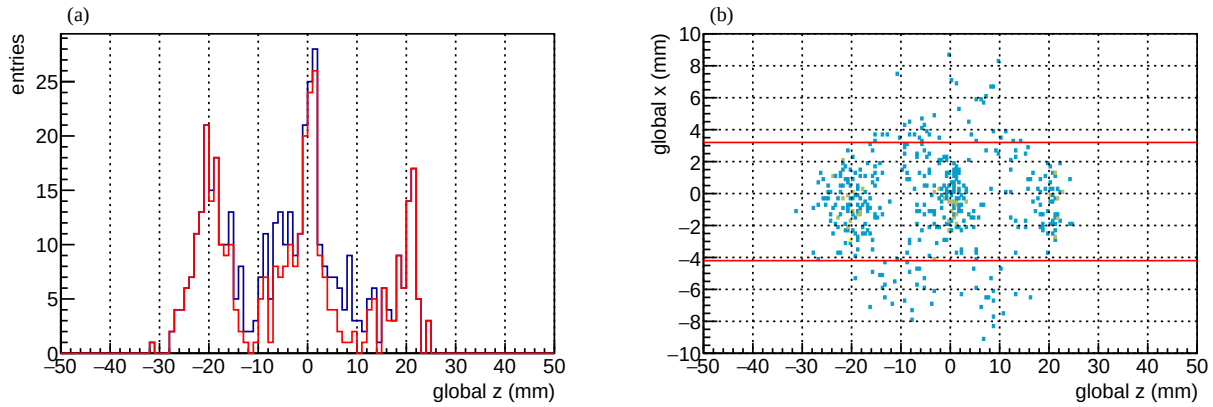

Figure 3.18: (a) the reconstructed vertex position along the global z direction. The entries in the blue histogram correspond to all entries in (b), while the entries in the red histogram correspond to those within the region enclosed by the red lines in (b). (b) the correlation between the global z and global x positions of the reconstructed vertex.

3.5 Efficiency Evaluation

For the cross-section evaluation, the detection efficiency of the ϕ meson in this measurement and its systematic uncertainties are evaluated.

3.5.1 Trigger Efficiency

As mentioned in Sec. 2.5.1, the trigger signals from GTR300, HBD, and LG were used to collect electron–positron decays of vector mesons at the trigger level. The trigger required that at least two "online tracks" (see Sec. 2.5.1), defined by triple coincidence among the three detector layers, exist simultaneously. Furthermore, the global positions of the two tracks had to be sufficiently separated, meaning that the opening angle between the two charged particles had to be large (approximately greater than 45 degrees at the LG channel positions). In addition, to reduce fake triggers generated by collision-overlapped events (multiple pA collisions occurring

simultaneously), a veto was applied: if the multiplicity of trigger hits in GTR300 exceeded a certain threshold, no trigger was requested.

The efficiency for produced ϕ mesons to satisfy these conditions is considered in Secs. 3.5.2.5 and 3.6. The former evaluates (1) whether the electron–positron tracks satisfy the online track condition, and (2) whether the two online tracks satisfy the opening-angle requirement. The latter evaluates the effect of veto, which is correlated with instantaneous beam intensity. The efficiency for generating trigger signals in each detector is evaluated in Sec. 3.5.2.

In this subsection, the efficiency for generating a trigger after the electron pair from a ϕ meson satisfies the above conditions is evaluated. As described in Sec. 2.5.2, signals from each detector are transferred to the trigger decision module (UT3) via the merger module (MRG). Due to transfer protocol limitations, at most 8 trigger signals per 64 channels can be transferred within 64 ns. Figure 3.19 shows the number of trigger hits per 64 channels for each detector during physics data taking. Even when more than 8 hits occur, they are filled into the bin at 8 on the horizontal axis. Because the multiplicity veto was applied during data taking, the impact of this transfer limitation on the trigger detection efficiency is relatively small.Here we estimate the transfer efficiency by taking the average of an overestimate and an underestimate. The fraction of events with 8 or more hits is at most 0.30%. Assuming all of these contribute to the trigger gives an overestimate. Assuming only one of the 8 (or more) hits contributes (0.30%/8 = 0.04%) gives an underestimate. Thus, the trigger efficiency is evaluated as 99.70–99.96%. For the cross-section evaluation, 99.83±0.13% is used. Since this is the efficiency for a single hit, it must be squared when evaluating the ϕ meson yield.

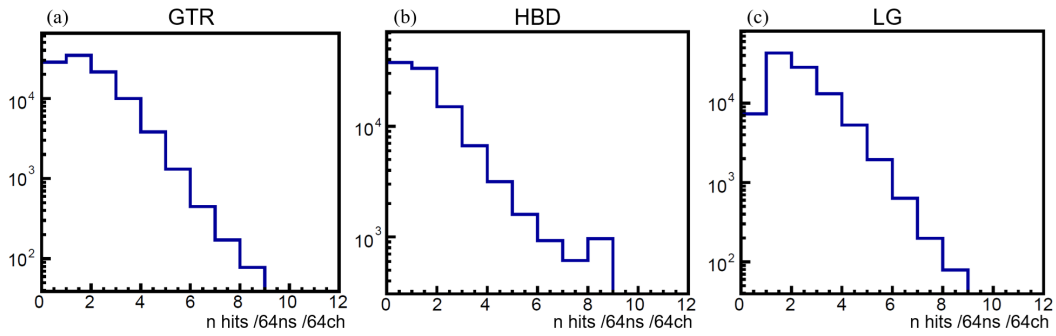

Figure 3.19: Distribution of the number of hits transferred per optical fiber from the MRG to UT3 (up to 8 hits per 64 channels within 64 ns). (a) GTR, (b) HBD, (c) LG, showing the fibers with the highest average hit multiplicity.

Next, the efficiency due to timing matching among the trigger signals of each detector is evaluated. The event timing is determined from the LG trigger signal, which has the highest time resolution among the three detectors. Relative to the LG timing, both GTR and HBD have a coincidence window of 320 ns. The timing offsets are determined from the TDC distributions. Figure 3.20 shows the TDC distributions of the LG, HBD, and GTR300 trigger signals obtained using the triple coincidence (IM3) of scintillation counters outside the spectrometer. Around the narrow peaks corresponding to correlated timing, broad peaks are observed due to accidental coincidences caused by instantaneous high beam intensity with time structure. In addition, the LG TDC distribution shows a 21 ns time structure corresponding to the transverse RF frequency applied during slow extraction from the MR. The coincidence window required during physics data taking is indicated by the black lines.

The coincidence efficiencies for GTR and HBD are evaluated by applying Gaussian fits to the narrow peaks in these TDC distributions and calculating the fraction of the Gaussian distribution within the coincidence window. The fits use a double-Gaussian and linear function to account for the broad background peak. The time widths of the trigger responses are found

to be 42.8±0.4 ns for GTR and 50.3±0.5 ns for HBD. The resulting coincidence efficiencies are 99.9±0.02% for GTR and 99.9±0.1% for HBD. Since these are single-track coincidence efficiencies, they must be squared when evaluating the ϕ meson yield. For the timing match between the two online tracks, the LG timing difference must be within 10 ns. This efficiency is evaluated by applying a ±10 ns window to the distribution of LG timing differences and is found to be 99.88±0.01%.

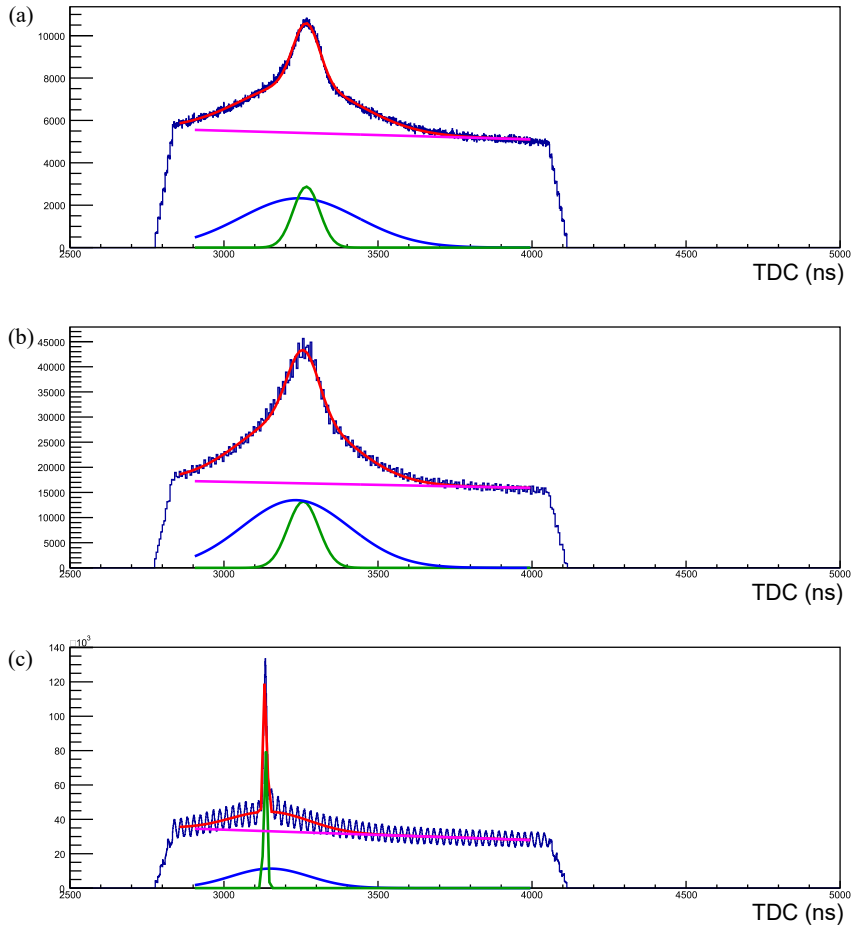

Figure 3.20: TDC distributions for (a) GTR, (b) HBD, and (c) LG. Black lines indicate the coincidence windows relative to the LG timing. Red lines show the fit results using a double-Gaussian + linear function. The narrow Gaussian (detector timing response) is shown in blue, the broad Gaussian (beam structure) in green, and the linear component in magenta.

As an exceptional trigger-signal handling measure, a 100 ns veto was introduced after receiving a GTR trigger signal, due to the presence of double pulses in the GTR trigger signals. This does not directly reduce efficiency, but if a ϕ-origin electron arrives during the veto period caused by a fake hit, its timing may be shifted earlier by up to 100 ns, effectively shortening the coincidence window. The probability of two GTR trigger hits occurring within 100 ns in the same channel during physics data taking is at most 6% for the busiest channels. The coincidence efficiency may decrease from 99.9% to as low as 92% due to the narrowed window. Taking this into account, the GTR coincidence efficiency is corrected to $0.999 \times (1 - 0.06) + 0.92 \times 0.06 = 99.5 \pm 0.6\%$.

Finally, summing all efficiencies evaluated in this subsection, the total trigger efficiency is 98.0±0.9%.

3.5.2 Detector Efficiency

3.5.2.1 STS

The detection efficiency of the STS was evaluated using a 3 GeV/c electron beam at the KEK PF-AR test beamline in November 2023, and was re-evaluated using calibration data taken at the J-PARC high-momentum beamline in May 2024, prior to the physics data-taking for this analysis. At the KEK PF-AR test beamline, the efficiency was evaluated by counting the number of incident particles using a coincidence of scintillation counters placed upstream and downstream of the STS sensor, and determining the fraction of events in which the STS recorded a hit. A detection efficiency of more than 98.5% was confirmed. At the J-PARC high-momentum beamline, using low-intensity beam data, a detection efficiency of at least 94% was confirmed, and the remaining inefficiency was attributed to the purity of the track sample. Details of these evaluations can be found in [51]. In the present cross-section evaluation, the STS detection efficiency is taken to be 98.5%, as measured at the test beamline.

In addition, to reduce the number of track candidates and save computation time by removing particles with large energy loss such as protons, an ADC cut was applied requiring the STS-measured ADC value to be below a certain threshold. The efficiency of this ADC cut was evaluated from the ADC distribution of STS clusters used in tracking and was found to be 93%. Considering gain-calibration differences among modules, the uncertainty is taken to be 4% in absolute value. Combining these, the overall STS detection efficiency is evaluated as 92%±4%.

As mentioned in Sec. 3.2, module 103 of the STS is not used in this analysis. Therefore, in the acceptance evaluation in Sec. 3.5.2.5, tracks passing through STS module 103 are treated as having 100% efficiency.

3.5.2.2 GTR

The detection efficiency of the GTR was evaluated by reconstructing tracks excluding the layer under evaluation, extrapolating (or interpolating) the track to the target layer, and determining the fraction of tracks with a cluster that existed at the extrapolated (or interpolated) position.

To evaluate high detection efficiency, the track sample used must be of sufficiently high purity, since contamination from fake tracks formed by accidental coincidences leads to an underestimation of the efficiency. Therefore, data taken with a beam intensity one-tenth of that used during physics data-taking (1×10^9 proton/spill) were used for this evaluation. The purity of the track sample was confirmed by verifying that tightening the track-selection conditions did not change the evaluated efficiency.

Table 3.1 summarizes the detection efficiencies of the x and y strips in GTR100, 200, and 300. The 200-layer chamber of module 106 shows lower efficiency than other chambers because the GEM gain during operation was insufficient. The 300-layer chamber of module 104 shows low efficiency in the y strip due to a noisy response. Module 107 is not used in this analysis.

Table 3.1: Detection efficiency of each GTR layer. The uncertainty is evaluated as 1% for all entries.

module	layer	efficiency (x strip)	efficiency (y strip)
104	100	0.98	0.97
104	200	0.96	0.95
104	300	0.91	0.69
106	100	0.98	0.96
106	200	0.92	0.90
106	300	0.96	0.95

Module 103 cannot be evaluated using the above method because the STS is absent. The ADC

distributions of the 100/200/300 layers of module 103 were compared with those of modules 104 and 106, and no significant gain degradation was observed. Therefore, in this analysis, the efficiency of module 103 is assumed to be the same as that of module 104. The impact of chamber-to-chamber performance variations on the cross-section evaluation is treated as a systematic uncertainty in Sec. 3.5.2.6.

As described in Sec. 3.4, track candidates are constructed not only from combinations requiring clusters in all tracker layers, but also from candidates missing one of the y layers (100, 200, or 300). Taking this into account, the tracker detection efficiency is given by

$$E = E_{100x} \cdot E_{200x} \cdot E_{300x} \cdot \{(E_{100y} \cdot E_{200y} \cdot E_{300y}) + (1 - E_{100y}) \cdot E_{200y} \cdot E_{300y} + E_{100y} \cdot (1 - E_{200y}) \cdot E_{300y} + E_{100y} \cdot E_{200y} \cdot (1 - E_{300y})\}. \quad (3.11)$$

Here, $E_{100x}, E_{200x}, E_{300x}$ denote the detection efficiencies of the x-strips in GTR100, GTR200, and GTR300, respectively, while $E_{100y}, E_{200y}, E_{300y}$ denote the corresponding efficiencies of the y-strips. From the efficiencies derived so far, two additional factors must be considered to obtain the actual detection efficiency during physics data-taking. First, cluster detection under high-background conditions must be considered. The physics data were taken with a beam intensity ten times higher than that used for the efficiency evaluation, and the trigger required at least two electron tracks, resulting in high cluster multiplicity per event. This effect is evaluated using the embedding method in Sec. 3.5.3.

Second, the efficiency for generating trigger signals in the GTR300 layer must be considered. The trigger efficiency was evaluated by checking whether a trigger hit corresponding to the reconstructed offline cluster had been produced. Figure 3.21 shows the ADC-dependent trigger turn-on curve for the GTR300 layer in each module, representing the fraction of cases in which a trigger signal is generated when a cluster exists. This curve was derived using only signals from modules not used in the trigger (i.e., without trigger bias). As seen in the figure, the curve is gradual due to the noise referred in Sec. 2.5.2. The overall trigger efficiency in the entire ADC range is typically found to be around 50%, and the exact values are listed in Table 3.2 efficiency (1).

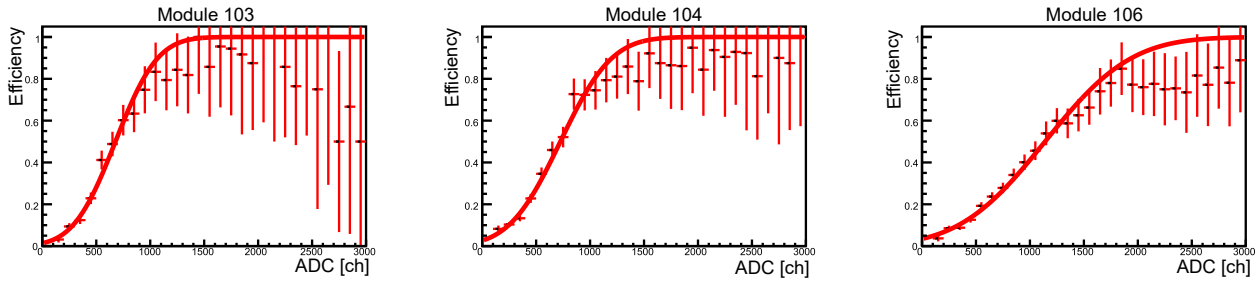

Figure 3.21: Trigger turn-on curve of the GTR-ASD.

For the cross-section evaluation, only electron pairs selected by the trigger can be used for the ϕ meson yield evaluation. To confirm the correspondence between clusters used in tracking and trigger signals, the residual between the cluster position and the trigger-signal position was plotted. Figure 3.22(b) shows the residuals (blue histogram) between clusters used in tracks reconstructed in the ω/ϕ mass region (using the method in Sec. 3.4) and all trigger signals in the same module. For comparison, the residuals for HBD and LG (y direction only) are also shown. The region affected by trigger bias is indicated by red lines. The red lines correspond to the sum of the trigger-channel width and the typical signal-spread width: 12.5 mm for GTR, 70 mm for HBD, and 90 mm for LG. If all tracks in the vector-meson mass region were selected by the trigger, the number of entries inside the red lines should match the number of tracks. Entries inside the red lines for all detectors are shown in magenta in the upper panel of

Fig. 3.22(b). For the GTR, however, the residual distribution shows a much broader tail than expected from the 12.5 mm trigger-channel width, unlike the other detectors.

To investigate the cause of this broad tail, calibration data taken with low-intensity beam (without trigger bias) were used to produce the same residual distribution. This distribution is shown in blue in Fig. 3.22(a). The green histogram shows the residuals obtained by event mixing, representing accidental coincidences between tracks and trigger hits from different events. The difference between the blue and green histograms represents the true trigger-hit response without bias. Although a small tail beyond 12.5 mm exists, the large tail seen in Fig. 3.22(b) is absent. This indicates that the large tail in Fig. 3.22(b) originates from accidental coincidences: when the true trigger channel is inefficient due to noise, a neighboring channel accidentally coincides with other detectors and produces a trigger signal.

The GTR trigger signal is divided into 24 channels in the y direction per module due to GEM detector capacitance, whereas the HBD and LG are divided into 6 channels. Thus, one trigger channel of HBD/LG corresponds to four GTR trigger channels. The red dashed line in Fig. 3.22(b) indicates the 12.5 mm width. The broadening of the GTR residual corresponds to approximately four channels, consistent with accidental-coincidence enhancement.

Based on these considerations, the GTR trigger detection efficiency in this analysis is defined as the sum of: (1) the probability that a trigger signal is generated when an offline cluster exists, and (2) the probability that the corresponding trigger channel is inefficient but one of the four neighboring channels accidentally coincides with other detectors. Due to this second contribution, the trigger-bias region indicated in magenta in the upper panel of Fig. 3.22(b) is corrected. The corrected residual distribution is shown in the lower panel. Most entries reconstructed in the vector-meson mass region are then consistent with being selected by the trigger.

Table 3.2 summarizes the GTR trigger detection efficiencies derived using this definition. The uncertainties are statistical, based on the sample size used for the evaluation.

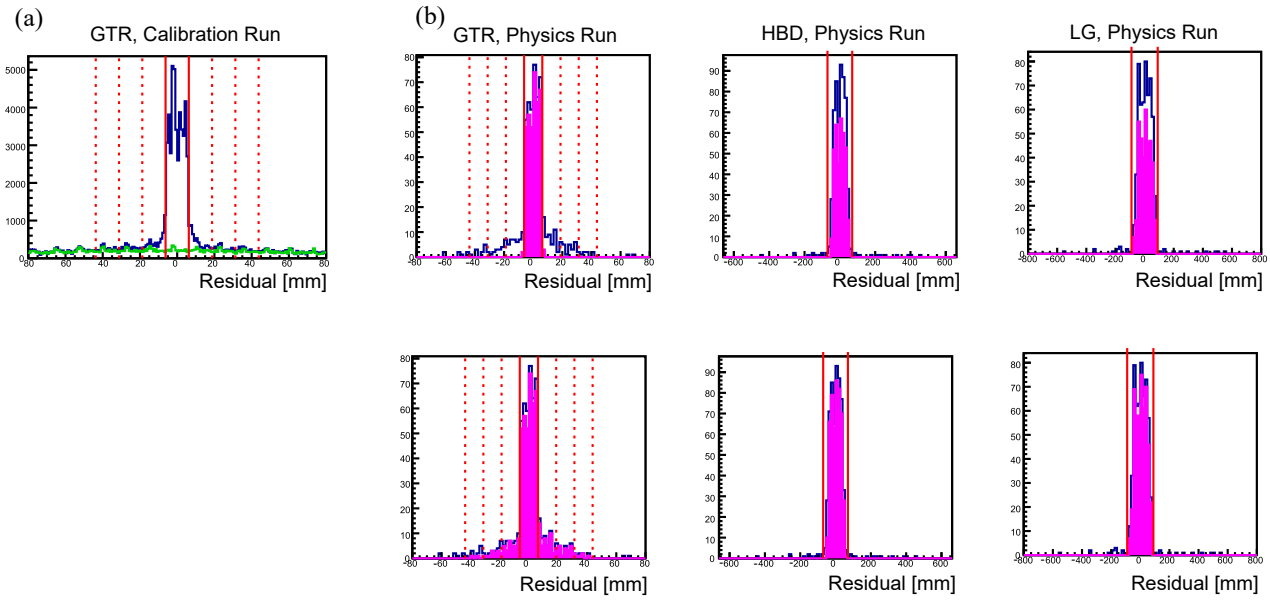

Figure 3.22: (a) Residuals between GTR cluster positions and trigger-signal positions for a track sample without trigger bias (blue histogram). The green histogram shows residuals from event mixing.
(b) Residuals between GTR/HBD/LG cluster (or hit) positions and trigger-signal positions for tracks reconstructed in the vector-meson mass region (blue histogram). The upper and lower blue histograms are identical. The meaning of the magenta histogram and red lines is described in the text.

Table 3.2: Trigger detection efficiency of the GTR.

module	efficiency (1)	efficiency (2)	efficiency (1)+(2)
103	0.440 ±0.013	0.070 ±0.005	0.510 ±0.014
104	0.538 ±0.012	0.088 ±0.004	0.626 ±0.012
106	0.464 ±0.009	0.088 ±0.003	0.552 ±0.009

3.5.2.3 HBD

The response of the HBD to electrons was evaluated by examining the HBD response to tracks identified as electrons by the LG. As the track sample, tracks reconstructed from physics data that were free from trigger bias (i.e., tracks that did not pass through the module whose trigger hits contributed to the event trigger) were used. Because the signal-to-noise ratio for electrons produced in proton–nucleus collisions is extremely poor, it is not possible to select a sufficiently pure electron sample using electron identification based solely on the LG detector. Therefore, unlike the GTR, it is difficult to evaluate the HBD response using a method in which tracks reconstructed by other detectors are used as the reference.

The HBD used in this experiment is a gas Cherenkov detector capable of detecting an average of 11 photoelectrons. The typical HBD response to electrons (ADC distribution) is a convolution of three distributions: a Poisson distribution for the number of detected Cherenkov photoelectrons, a Polya distribution for the number of electrons amplified by the GEM, and a Gaussian distribution representing noise. In this evaluation, for each module, the electron response (ADC distribution) was first extracted, and the trigger turn-on curve was applied to this distribution to determine the detection efficiency.

To extract the electron response (ADC distribution), tracks free from trigger bias were extrapolated to both the HBD and LG detection planes, and events were selected in which an HBD cluster and an LG hit existed near the extrapolated intersection point. Although both HBD and LG are detectors that select electrons by requiring large pulse heights and suppress background, in this evaluation the association thresholds were intentionally set low to avoid losing electron efficiency. Specifically, the HBD required at least 2 photoelectrons (whereas 6 photoelectrons are required in normal electron identification), and the LG required at least 0.04 GeV (whereas 0.2 GeV and $E/p > 0.53$ are required in normal identification). The LG E/p distributions for the selected sample are shown in Fig. 3.23(a), and the corresponding HBD ADC distributions are shown in Fig. 3.23(b) as blue histograms for each module. These blue histograms contain a mixture of electrons and pions.

Although the HBD has high rejection power, the ADC distributions of background pions and electrons overlap significantly, making it difficult to determine the contamination level directly. In contrast, the LG, despite having lower rejection power than the HBD, detects a large amount of photons for electrons and exhibits energy dependence in its response. As a result, the electron peak in the LG E/p distribution is sharply localized near 1 and does not leak significantly into the low-E/p region. Therefore, the number of background pions contained in the blue histograms of Figs. 3.23(a)(b) was estimated by assuming that the peak in the low-E/p region of Fig. 3.23(a) originates entirely from pions.

The red histogram in Fig. 3.23(a) represents a sample with enhanced pion content, obtained by removing the HBD association requirement from the blue sample and normalizing the distribution to match the number of entries in the 0–0.4 region. To first approximation, the normalized red histogram gives the number of pions in the blue sample. In reality, the red sample contains a small number of electrons because it is a subset of the blue sample. The upper limit of this electron contamination was estimated from the difference between the blue histogram and the normalized red histogram.

Similarly, the HBD ADC distribution without LG association (a pion sample) is shown as the red histogram in Fig. 3.23(b). The normalization was chosen so that the number of pions matched the estimate from the LG E/p distribution. The good agreement between the red and blue histograms in the low-ADC region confirms the validity of the normalization.

Finally, subtracting the red histogram from the blue histogram in Fig. 3.23(b) yields the HBD electron response (ADC distribution). This result is shown in Fig. 3.23(c). The red curve represents a fit using a convolution of Poisson, Polya, and Gaussian distributions. The fitted mean number of photoelectrons is shown in the legend. All modules exhibit distributions with mean values around 11 photoelectrons, with differences at the 10% level. The differences may originate from the accuracy of the conversion to the number of photons performed in Sec. 3.3.3, or from variations in the photocathode coating quality, or from differences in the gas-chamber conditions between modules 104/103 and 106/107.

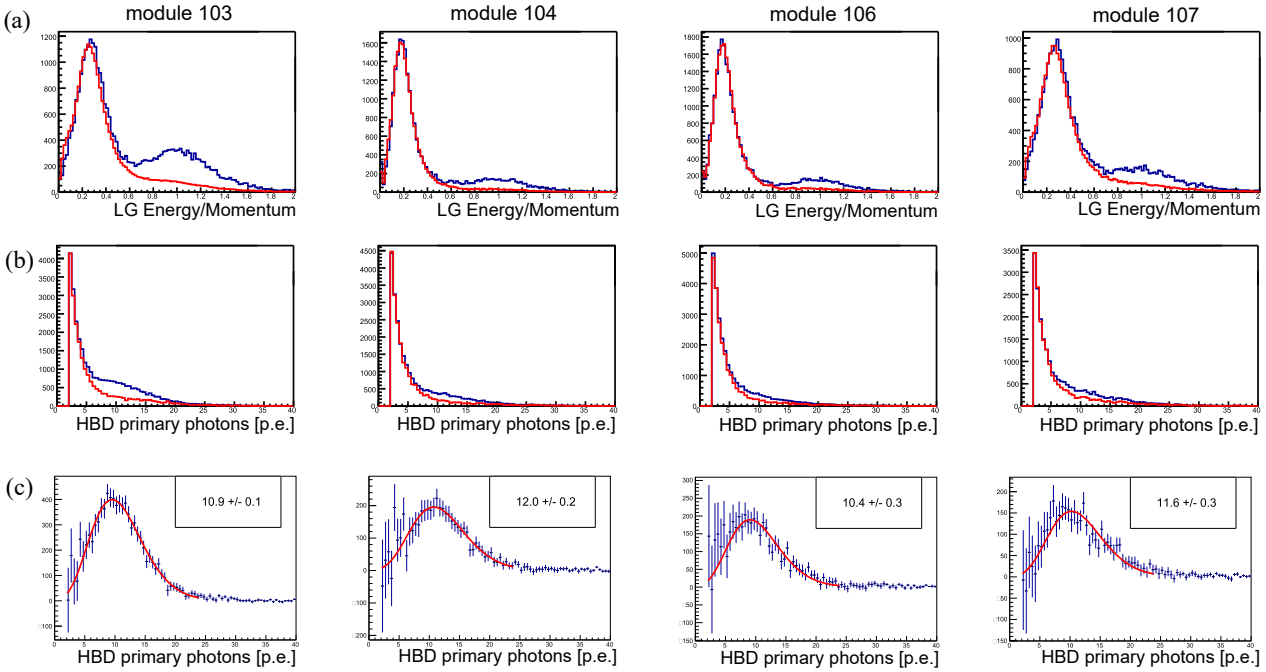

Figure 3.23: (a) LG E/p distributions for each module. Blue: mixed sample of electrons and pions. Red: pion-enhanced sample.
(b) HBD ADC distributions for each module. ADC values are converted to the number of photons before GEM amplification using the method in Sec. 3.3. Blue: mixed sample; red: pion sample.
(c) Electron response obtained by subtracting the red histogram from the blue histogram in (b). The red curve is the fit described in the text.

Next, the response of each HBD trigger channel was evaluated. The trigger turn-on curve, defined as the fraction of events in which a trigger signal was generated when an HBD cluster existed, was extracted as a function of cluster ADC value. A typical turn-on curve is shown as the red line in Fig. 3.24(a). As in the GTR, noise affecting only the trigger-signal path causes the curve to be gradual. Figures 3.24(a)(b) also show the electron ADC response (blue curve) obtained earlier. This function is a convolution of Poisson, Polya, and Gaussian distributions, with the Poisson mean set to the extracted mean number of photoelectrons. The magenta curve in Fig. 3.24(b) represents the product of the electron-response function and the turn-on curve.

The HBD detection efficiency for each trigger channel is defined as the ratio of the integral of the magenta curve (entries above threshold) to the integral of the blue curve (total electron response). The efficiencies for all trigger channels are summarized in Fig. 3.25. Regions without

values correspond to channels that were non-operational due to GEM or ASD-board issues. The uncertainty due to the determination of the mean number of photoelectrons is about 1% in absolute efficiency. Channel-dependent differences in detector response are evaluated together with other detectors in Sec. 3.5.2.6. Long-term stability is discussed at the end of this subsection.

The resulting efficiencies show significant channel dependence, which arises from applying a uniform trigger threshold to all channels despite gain variations in the GEM stack during operation (see Sec. 3.3.3).

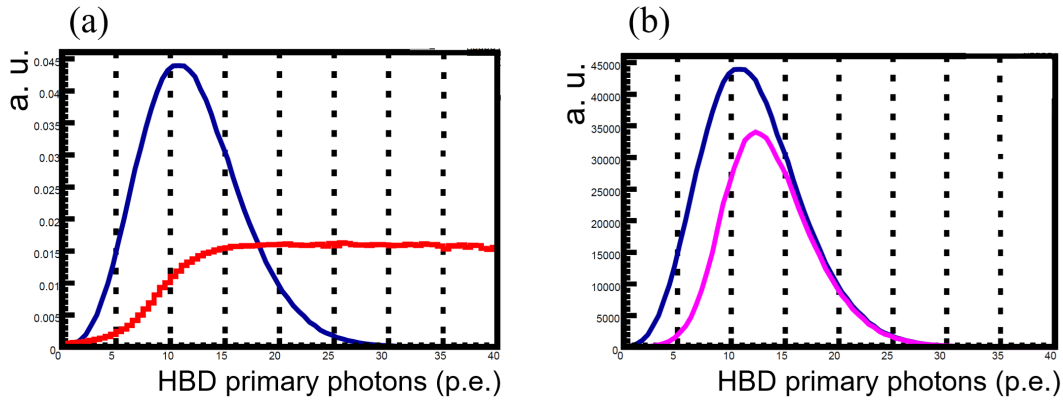

Figure 3.24: (a) Electron-response function (blue) and HBD trigger turn-on curve (red) for module 104. Vertical scale is arbitrary.
(b) Electron-response function (blue) same as in (a). Magenta: product of the electron-response function and the turn-on curve.

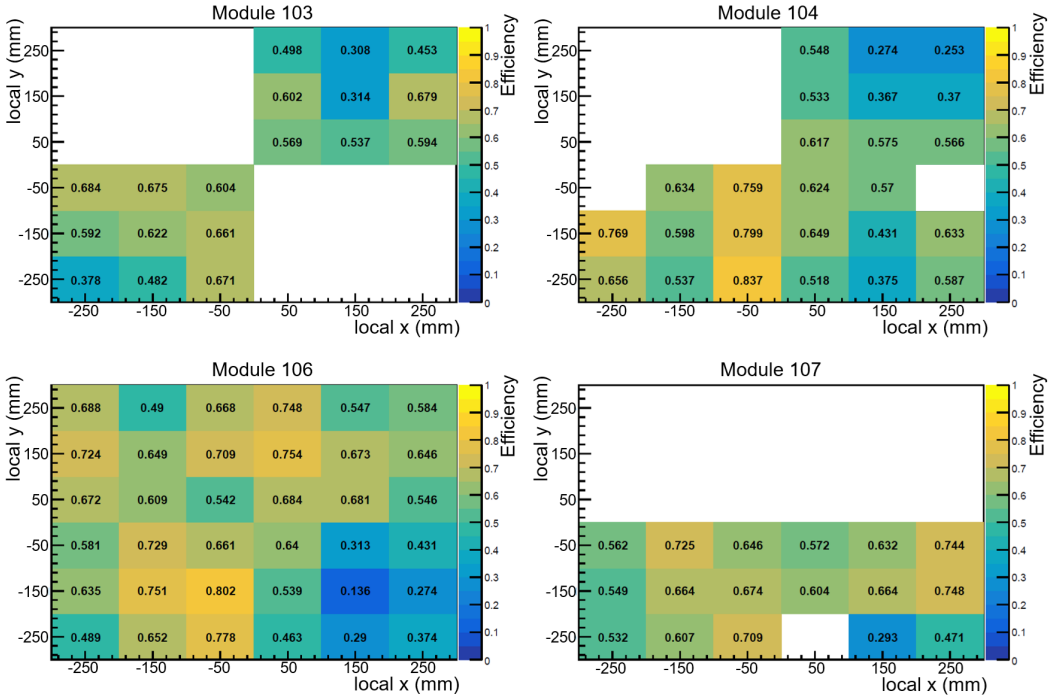

Figure 3.25: HBD detection efficiency for each trigger channel. The uncertainty due to the determination of the mean number of photoelectrons is about 1% in absolute efficiency.

Up to this point, the HBD detection efficiency at the trigger level has been evaluated. In the offline analysis, an additional requirement is imposed to reduce pion contamination: the cluster size must be at least 2. Because cluster size may correlate with ADC value, this cut must be

evaluated while considering its correlation with the trigger efficiency. The number of electrons in the LG E/p distribution (Fig. 3.23(a)) was counted with and without the cluster-size cut, and the ratio was taken as the efficiency of the cluster-size requirement. The efficiency was found to be 95%, with a systematic uncertainty of 3% due to normalization uncertainty in the pion distribution.

Finally, the long-term stability of the HBD was evaluated. During physics data taking, calibration data were acquired approximately every 6 hours to correct channel-dependent gain variations using the method described in Sec. 3.3. The long-term gain variation over 6-hour intervals corresponded to at most 1 photoelectron, equivalent to a 5% change in detection efficiency. In addition, short-term gain variations of up to 2 photoelectrons were observed over periods of 15–30 minutes after beam resumption following accelerator downtime. Figure 3.26(a) shows the scaler counts of HBD trigger signals during physics data taking. Vertical lines show the restart timing of beam delivery to the experimental target. Just after the restart, increasing of scaler counts are observed.

Figure 3.26(b) shows the ADC distributions during these periods. The black histogram corresponds to immediately before beam stop, the red to immediately after beam resumption, and the blue to one hour after resumption. The ADC variations correlate with the scaler variations, indicating that the effect originates from GEM gain changes rather than noise. The cause is still unknown, but it is considered related to the charge-up effect in GEM due to the charged particle flux through the GEM.

These rapid gain variations occurred during 12% of the total physics data-taking time. Applying the gain calibration method of Sec. 3.3 to data taken immediately after beam resumption showed gain differences of up to 2 photoelectrons, corresponding to a 10% change in detection efficiency. The impact on the ϕ-meson yield, considering that 12% of the data had a 10% efficiency variation, is 4%. This 4% is included as a systematic uncertainty in the cross-section evaluation.

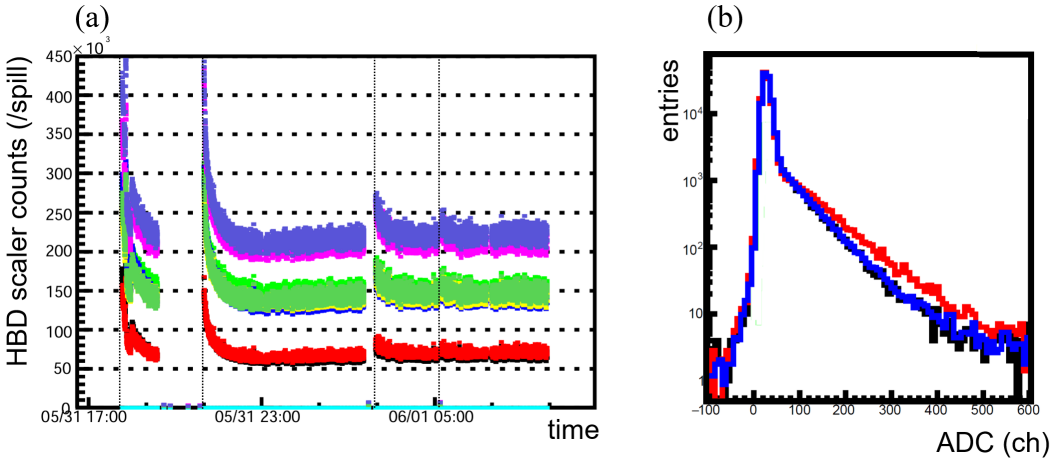

Figure 3.26: (a) Time drift of scaler count of HBD trigger per beam spill. Values for nine trigger channels in module 106 are shown by different colors. Vertical lines show the restart timing of beam delivery.
(b) HBD ADC distributions before and after beam interruption. Black: just before beam stop; red: just after beam resumption; blue: one hour after resumption.

3.5.2.4 LG

The LG detection efficiency in this analysis can be obtained by applying the electron-selection cut of $E/p > 0.53$ to the electron E/p distribution. Figure 3.27 shows the energy–momentum correlation and the E/p distribution. A Gaussian fit to the electron peak near $E/p = 1$ yields

a sigma of 0.27. The cut at $E/p > 0.53$ corresponds to 1.7 sigma, giving a detection efficiency of 96%.

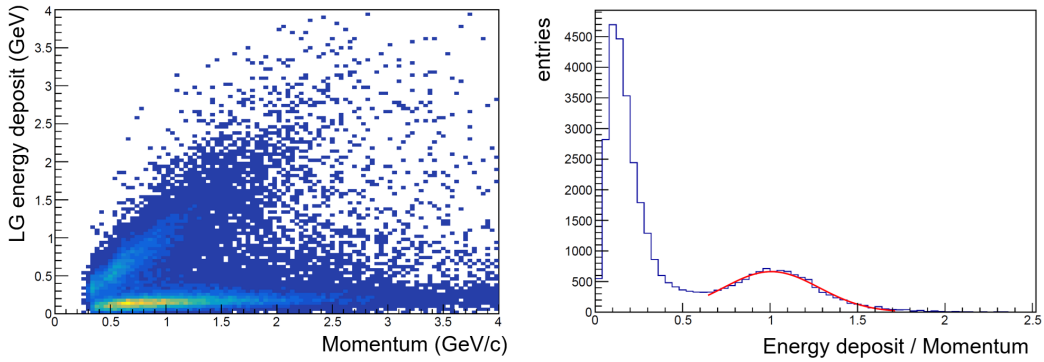

Figure 3.27: (a) Energy–momentum correlation observed in the LG. The diagonal component corresponds to electrons. The flat component less than 0.2 GeV in energy corresponds to background pions.
(b) E/p distribution for the sample in (a). The red curve shows a Gaussian fit to the electron peak.

However, as shown in Sec. 3.3, the trigger thresholds for the forward LG channels were set high (up to ∼1 GeV) in this measurement. Therefore, the trigger-level detection efficiency may be lower than the above estimate. Furthermore, at the trigger level, the LG threshold is applied to hits before clustering. Thus, inefficiency may arise when the LG signal from an incident electron is shared across two adjacent channels.

To account for these effects, a simulation was performed using the ϕ-meson kinematics obtained from the simulation described in Sec. 3.5.2.5, together with detailed LG detector-response measured at the KEK PF-AR test beamline in November 2022. The simulation proceeded as follows:

1. Simulate electron–positron tracks from ϕ-meson decay using the method described in Sec. 3.5.2.5.
2. Obtain the incident positions and angles of electrons and positrons on each LG channel.
3. Determine the energy deposit using the position- and angle-dependent response measured in the test-beam experiment.
4. If the particle trajectory crosses two channels considering the depth of the lead glass, share the energy deposit between the two channels according to the path length.
5. Apply the trigger thresholds and offline thresholds for each channel, and evaluate the fraction of simulated ϕ mesons that survive as the detection efficiency.

As a result, the LG detection efficiency considering only the trigger threshold was 98% for single tracks and 96% for track pairs. After applying the offline cuts of $E > 0.2$ GeV and $E/p > 0.53$, the efficiencies became 95% for single tracks and 91% for track pairs. Here, the single-track efficiency is the square root of the pair efficiency. These values include a 2% absolute uncertainty due to the reproducibility of the LG response in the simulation.

Ultimately, these efficiencies are consistent with the simple estimate at the beginning of this subsection, indicating that no significant inefficiency was introduced by the trigger thresholds in this measurement. The reason is that electrons originating from ϕ mesons tend to enter the forward acceptance region with higher momentum, and the applied trigger threshold also tended to be higher in the forward region. Consequently, this high threshold did not result in a significant efficiency loss.

3.5.2.5 Overall Detector Acceptance

Using the detection efficiencies of the four detectors evaluated so far, the overall spectrometer acceptance for this analysis is determined. As mentioned again in Sec. 4.2, the acceptance of this measurement corresponds to a very limited kinematic region of the ϕ meson. Therefore, in order to derive the total cross section from the yield of detected ϕ mesons, the kinematics of ϕ mesons produced in proton–nucleus reactions are assumed based on the event generator JAM [14]. Consequently, the acceptance evaluation in this measurement is performed using the ϕ momentum distribution obtained from JAM, following the steps below.

1. For each ϕ meson generated by JAM, record its laboratory-frame momentum immediately before the decay routine is applied. This momentum distribution is used as the input for the following steps.

2. Apply isotropic e^+e^- decay in the center-of-mass frame to the ϕ mesons from step 1.

3. Apply QED corrections (internal radiative corrections) to the electrons and positrons from step 2.

4. Evaluate the energy loss of the electrons and positrons in the laboratory frame due to the material budget of the target and detectors using Geant4.

5. Evaluate the fraction of electrons and positrons from step 4 that enter the spectrometer acceptance. As mentioned in Sec. 3.2, only cases in which the positron enters the left arm and the electron enters the right arm are considered. Furthermore, as described in Sec. 3.5.1, the tracks must satisfy the geometrical trigger conditions.

6. Apply the detection efficiencies of the six detector layers (STS, GTR100, GTR200, GTR300, HBD, LG) traversed by the electrons and positrons from step 5. The position dependence of the detection efficiency (module-level for STS and GTR, trigger-channel-level for HBD and LG) is also taken into account.

The momentum distribution of the generated ϕ mesons is shown in Sec. 4.2. Here, Fig. 3.28 shows the kinematics of ϕ mesons whose decay electrons and positrons enter the detector acceptance after applying steps 5 and 6.

Although steps 5 and 6 include the detection efficiencies of each detector, the resulting ϕ kinematics change very little. Therefore, when evaluating the track reconstruction efficiency in Sec. 3.5.3, the embedding method is applied using simulated tracks processed only up to step 5. The inefficiency between steps 5 and 6 and the track reconstruction efficiency evaluated by the embedding method are assumed to be uncorrelated and are treated simply as a product.

3.5.2.6 Systematic errors of detector acceptance

Finally, the systematic uncertainties of the acceptance evaluated in the previous subsection are determined.

To confirm how well the overall detection efficiency evaluated earlier reproduces the actual position dependence of the detector response, the acceptance in real data and simulation is compared as follows. First, for the "data acceptance," electron tracks are reconstructed from events that contain at least one track identified as an electron at the trigger level. The profiles of the cross points between these tracks and each detection plane are prepared. Next, for the "simulation acceptance," sample of e^+ and e^- are prepared as follows. Using JAM, π^0 sample is generated in 30 GeV p+Cu reactions and fed into the E16 detector simulation using Geant4. The $\pi^0 \to 2\gamma$ and $\pi^0 \to e^+e^-\gamma$ (Dalitz decay) were performed by Geant4. $\gamma \to e^+e^-$ conversion

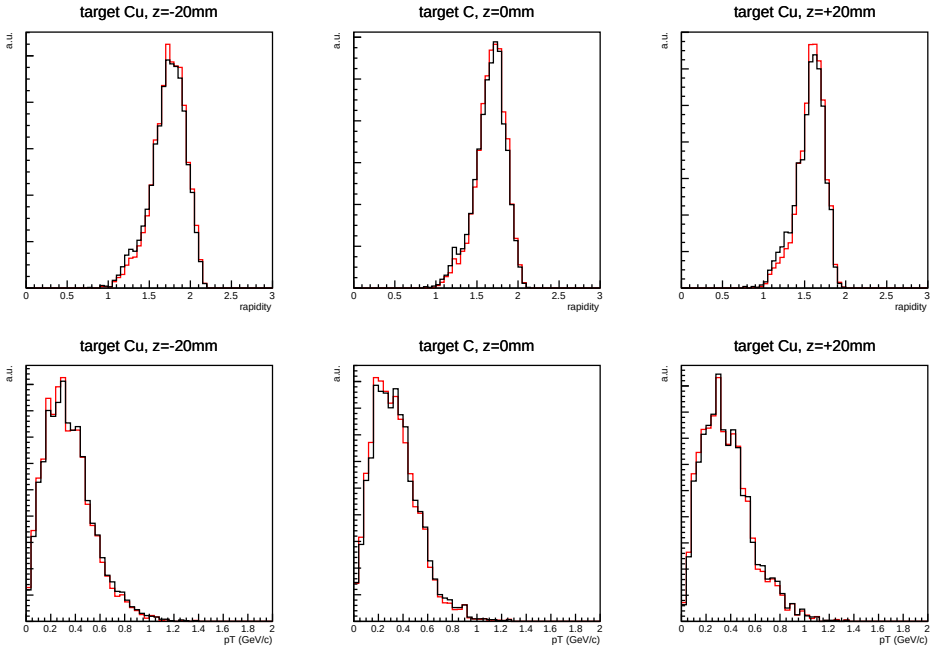

Figure 3.28: Kinematic distributions of ϕ mesons detectable in this measurement after applying acceptance up to step 5 (black histogram), for each target position in the present measurement. The upper panel shows the rapidity distribution, and the lower panel shows the transverse-momentum distribution. The red histogram shows the kinematics after additionally applying the position-dependent detection efficiencies of each detector (step 6). Both histograms are normalized to have the same number of entries.

and energy loss, multiple scattering for e^+/e^- in the target and detector materials are also taking account by Geant4. For electrons and positrons that enter the detector acceptance defined in Sec. 3.5.2.5, the profiles of their cross points with each detection plane are prepared and compared with those from real data.

To reduce the effect of kinematic differences on the profiles, the samples are decimated therefore the absolute momentum distributions match. The resulting momentum distribution, adjusted to match that of electrons from simulated ϕ decays, is shown in Fig. 3.29.

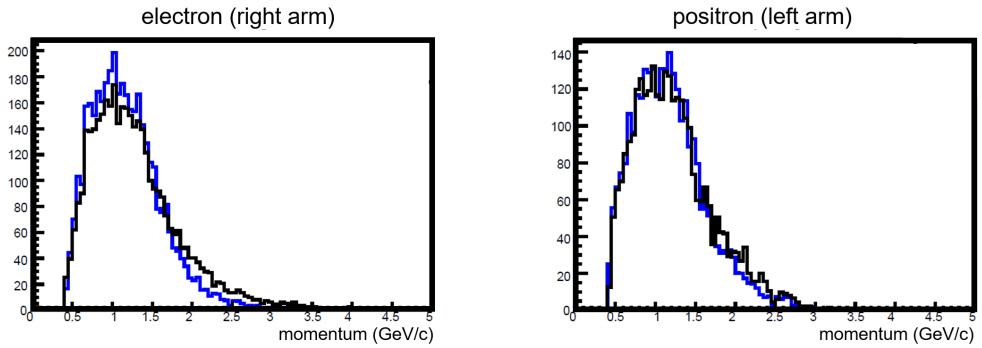

Figure 3.29: Correction of simulated e^+e^- momentum distribution. Black: single-electron tracks from data. Blue: simulation.

Figure 3.30 shows the profiles in the local x and local y directions at each detection plane. Normalization is based on Fig. 3.29. While the overall trends agree, some discrepancies are observed. In particular, to investigate the deviation seen in the y-profile of module 104, the channel dependence of the GTR trigger efficiency, which is previously not included, was addi-

tionally considered, as shown in Fig. 3.31. Including this dependence improves the agreement, suggesting it is one source of the discrepancy.

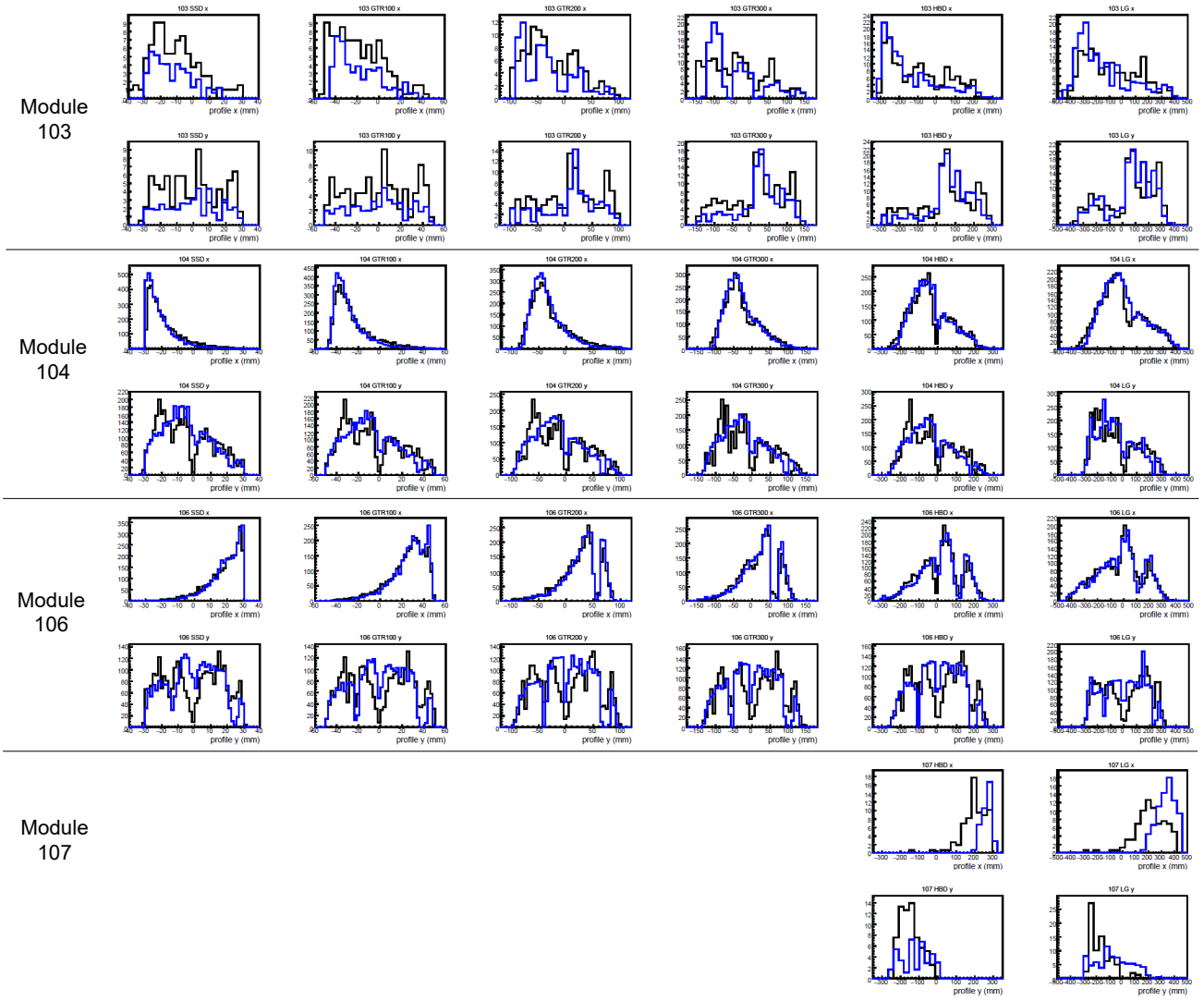

Figure 3.30: Profiles of single-electron tracks at each detector layer. Black: data. Blue: simulation. For each module, the upper panel shows the local x distribution and the lower panel shows the local y distribution. From left to right: STS, GTR100, GTR200, GTR300, HBD, and LG.

To evaluate how these acceptance discrepancies affect the ϕ-meson yield, the acceptance profiles in Fig. 3.30 were applied to the electron and positron distributions obtained in step 5 of Sec. 3.5.2.5, and the remaining number of ϕ mesons was compared between data and simulation. Since the profiles at each detector layer include the effect from all layers of detection efficiency and dead regions, the acceptance evaluation should ideally obtain consistent results regardless of which layer is used. However, in this evaluation, a relative uncertainty of 10% arises between the used layers.

Comparing the acceptances from data and simulation shows a relative difference of 13%. Therefore, this 13% is taken as the systematic uncertainty associated with the reproducibility of the acceptance simulation. For reference, when the channel dependence of the GTR trigger efficiency as shown in Fig. 3.31 is included, the difference becomes 10%. Since this does not significantly improve the accuracy of the acceptance evaluation for the current cross-section measurement, it is not included in the final evaluation.

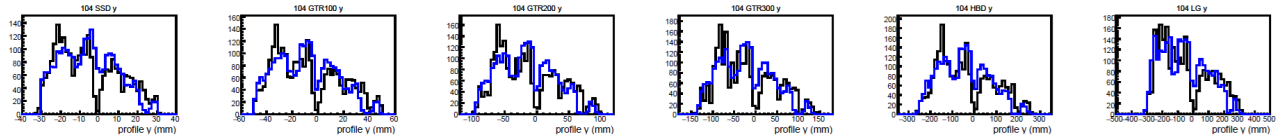

Figure 3.31: Same as the local y-profile of module 104 in Fig. 3.30, but including the channel dependence of the GTR trigger efficiency.

3.5.3 Analysis Efficiency

In this section, the efficiency associated with the offline analysis using the recorded data (analysis efficiency) is evaluated. The analysis efficiency is defined as the product of the Track reconstruction efficiency and the efficiency from Analysis cuts, where each includes the following considerations:

- Track reconstruction efficiency
  - Loss of GTR clusters due to merging with background hits (see Sec. 3.5.2.2)
  - Cut on the chi-square value obtained from the Runge–Kutta fitting applied to single-track candidates (see Sec. 3.4.1)
  - Cut on the vertex distribution and chi-square value obtained from the Runge–Kutta fitting applied to pair candidates (see Sec. 3.4.3)
- Analysis cut
  - Efficiency loss due to the residual cuts in the HBD/LG association (see Sec. 3.4.2)

The track reconstruction efficiency was evaluated using the embedding method described below. The analysis-cut efficiency was evaluated using real data, since incorporating the trends shown in Sec. 3.4.2 into simulation would be complicated.

Procedure of the Embedding Method

First, a "cluster sample" (waveform information from multiple hit strips) is prepared as GTR response function using real data. It is obtained by reconstructing tracks from low-intensity beam data and collecting the clusters used in those tracks. A cluster sample is prepared for each GTR layer (100, 200, 300) of each module. Waveforms in which two clusters overlap, such as those shown in Fig. 3.4(b), are not used.

This cluster sample is then embedded into real experimental data, which contain the actual background environment (i.e., the waveforms of the cluster sample are added to the waveforms of real data). Although real data include ϕ mesons enhanced by the trigger, their number is extremely small (the fraction of events containing a detected ϕ meson is about 5×10^{-7}), therefore their impact is negligible. For each point where the simulated electron or positron (processed up to step 5 in Sec. 3.5.2.5) passes through a GTR layer, a cluster sample is embedded. The local position of the simulated cluster is smeared so that the width of the residual distribution matches that observed in real data taken using the low-intensity beam. For each experimental target position, 20,000 events are prepared, each containing one embedded e^+e^- pair from a ϕ meson. The same selection procedure described in Sec. 3.4.1 is then applied to the embedded data.

Next, the procedure in Sec. 3.4.2 is considered. In the simulation, the association window is set to the same width as in Sec. 3.4.2 (3.1 sigma in local x direction and 2.8 sigma in local y direction), and the same duplicate-cut procedure is applied. As a remark, the efficiency of

the EID association is evaluated separately from the embedding method, which is treated as an analysis cut.

Single Track Reconstruction Efficiency

The validity of the embedding method is demonstrated as follows. First, it is confirmed that embedded data without background reproduce the low-intensity data. Figure 3.32 shows the GTR residual distributions from low-intensity real data (labeled as "data") and from embedded data with smearing applied to match the same width (labeled as "simulation"). Figure 3.33 compares the chi-square distributions of reconstructed single tracks under the same conditions. The chi-square distribution for 4 degrees of freedom is shown as a red dashed line. The embedding method reproduces the low-background data well. Figure 3.34 shows the chi-square distribution when embedding is applied to real physics data. Because cluster positions shift when merged with background hits, the chi-square distribution is distorted. The duplicate cut also affects the shape by preferentially selecting tracks with smaller chi-square values. Since real physics data contain many fake tracks, it is not currently possible to extract such a distribution directly from data. The cut condition used in this analysis is also shown in Fig. 3.34. The threshold is chosen so that efficiency is not significantly lost even with the distortion.

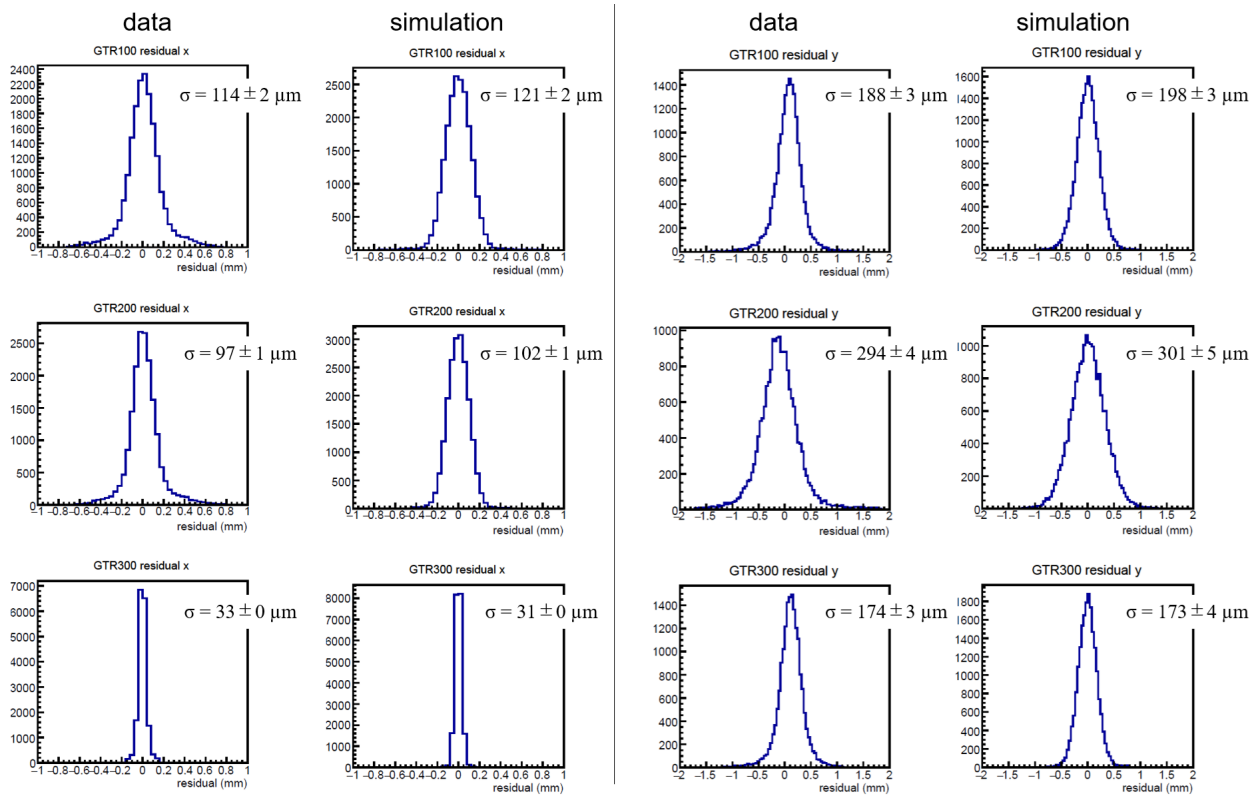

Figure 3.32: GTR residual distributions from single-track data with low-intensity beam labeled as data, compared with those from embedded tracks without background labeled as simulation. Left: local x residuals; right: local y residuals. From top to bottom: GTR100, 200, 300 layers.

Next, the inefficiency caused by cluster merging with background is examined. For embedded data using real background, the fraction of embedded clusters (containing the embedded strip) that are successfully detected is evaluated. Cluster loss due to merging is expected to increase with multiplicity. Furthermore, as described in Sec. 3.4.1, stricter cuts are applied to clusters when multiplicity is high (i.e., when many track candidates exist), which also reduces efficiency. Figure 3.35 shows the multiplicity dependence of this efficiency for the x strips (a)

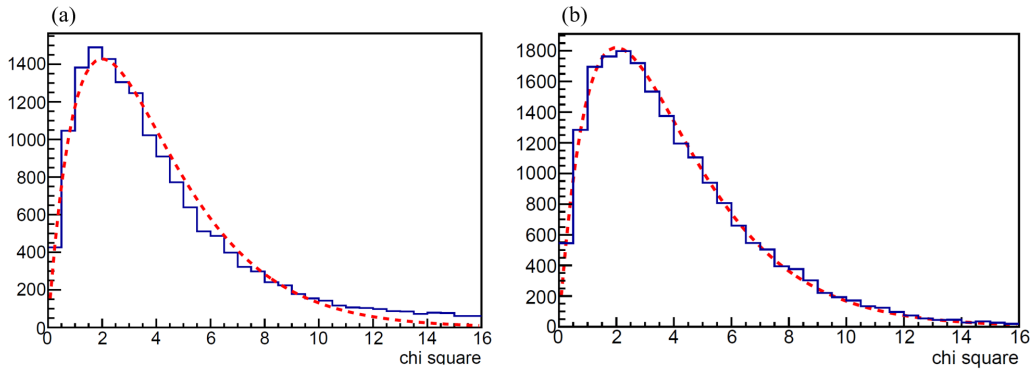

Figure 3.33: (a) Chi-square distribution of reconstructed tracks from low-intensity data. (b) Same distribution from embedded data without background. χ^2-distribution for 4 degrees of freedom is overlaid as a red dashed line.

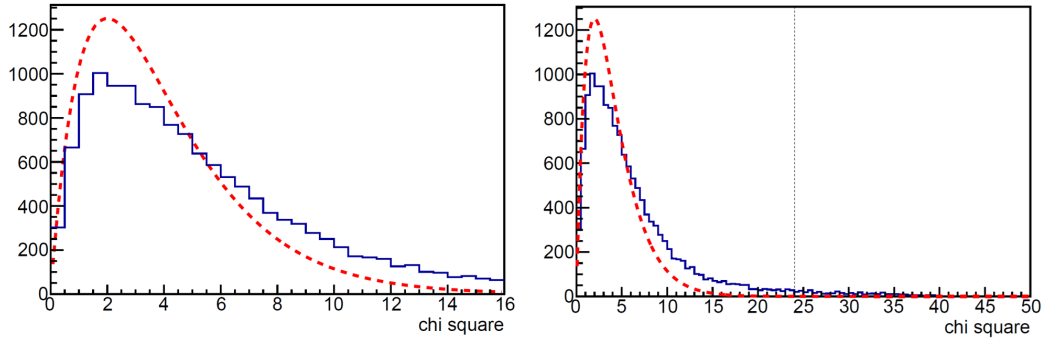

Figure 3.34: Chi-square distribution from embedded data using real physics data as background. Left: same range as Fig. 3.33. Right: wider range. The dotted line indicates the cut condition $\chi^2/\mathrm{ndf} < 6$ used in the analysis.

and y strips (b) of the GTR100 layer. Here, multiplicity is counted as a sum of clusters in three forward modules (103, 104, and 106) for each event. The red points show the efficiency for detecting clusters in all GTR layers (100, 200, 300). The blue points show the efficiency for those clusters to satisfy the track-candidate conditions (Sec. 3.4.1). A decreasing trend with multiplicity is observed. Figure 3.35(c) shows the efficiency for both x and y track candidates to exist. The magenta points require both conditions shown in Figs. 3.35(a)(b), and the green points additionally require timing matching between x and y clusters. Cluster merging affects not only position information but also timing information.

Pair Track Reconstruction Efficiency

For the embedded data, as described in Sec. 3.4.3, plus-charge and minus-charge tracks are paired, and Runge–Kutta fitting is performed under the requirement that the two tracks share a common vertex position. The resulting chi-square distribution of the fit is shown in Fig. 3.36(a). For comparison, Fig. 3.36(b) shows the distribution obtained from data. The vertex distribution from simulation is shown in Fig. 3.37. In Figs. 3.36(a) and 3.37, the blue histograms represent all pairs that survived the previous selection steps, while the red histograms represent only those pairs composed exclusively of clusters containing the embedded strips. The vertex distribution shown in red in Fig. 3.37 exhibits good separation between the experimental targets, indicating that the $z = \pm 10$ mm cut introduced in Sec. 3.4.3 contributes negligibly to the efficiency. On the other hand, there is a large difference in the number of entries between the blue and red histograms. This difference corresponds to events in which the embedded clusters were not detected due to merging with background hits, and instead a background cluster produced a

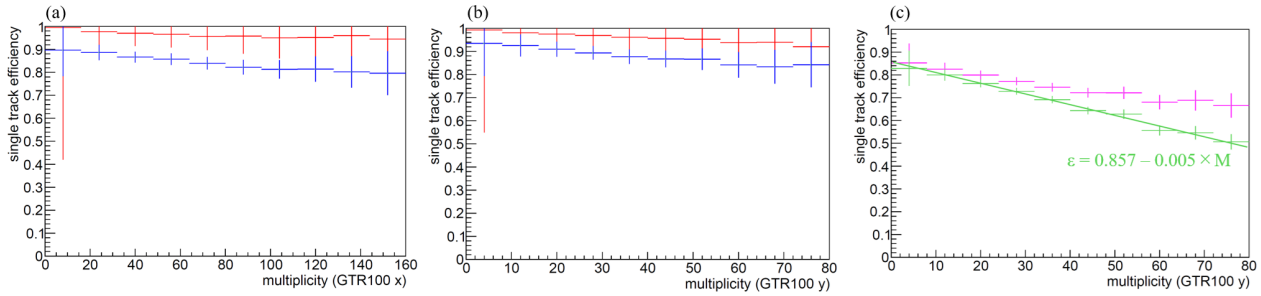

Figure 3.35: Multiplicity dependence of the single-track reconstruction efficiency evaluated using the embedding method. (a) Cluster multiplicity of x-strip in GTR100; (b)(c) Cluster multiplicity of y-strip. (a) shows the reconstruction efficiency for x track candidates; (b) for y track candidates. (c) shows the efficiency for both x and y track candidates to be detected. The meaning of each color is described in the text.

single track, or events in which a background cluster produced a single track with a smaller chi-square value than the embedded one. Although such events do not originate from the intended ϕ mesons, if they appear near the ϕ-meson mass region after mass reconstruction, they cannot be distinguished from true ϕ mesons. In practice, they contribute to a broadening of the mass spectrum. Therefore, these pairs are retained when evaluating the reconstruction efficiency.

The cut conditions applied to the chi-square distribution are indicated by dashed lines in Fig. 3.36. These conditions were chosen to maximize the signal-to-noise ratio of the mass spectrum reconstructed from data (see Sec. 4.1.1 for the definition of S/N). As a result, different conditions are applied for the carbon and copper targets. In particular, for the carbon target, a relatively strict chi-square cut is required to observe the ϕ-meson peak. The difference in the shapes of the distributions in Figs. 3.36(a) and (b) is attributed to the fact that the data sample contains many pairs of tracks that do not originate from the same target.

As the final step of mass reconstruction, the vertex position is fixed to the location of each experimental target ($z = -20, 0, +20$ mm), and pair fitting is performed. The invariant mass is reconstructed from the resulting electron and positron momenta. A chi-square cut is also applied here, but because the vertex cut is already strict, the efficiency loss from this cut is small. The resulting mass spectrum is shown in Fig. 3.38. Here, only the target at $z = 0$ (carbon target) is shown as an example. The blue and red histograms correspond to the same conditions as in Fig. 3.37. The green histogram shows the mass distribution obtained without applying the embedding method, using simulation up to step 3 of Sec. 3.5.2.5. As shown, the mass spectrum of the ϕ meson is broadened due to the effects of cluster merging with background hits (red histogram) and mis-association with background clusters (blue histogram), as expected from simulation.

Using the results described above, the track reconstruction efficiency is evaluated. In this evaluation, events in which the ϕ meson remains in the sample represented by the blue histogram in Fig. 3.38 are considered efficient. The efficiency is defined as the ratio of the number of reconstructed ϕ mesons in the mass region to the number of embedded ϕ events (20,000). As shown in Fig. 3.35, the single-track reconstruction efficiency has a clear dependence on multiplicity (M). Furthermore, the efficiency is expected to depend on the ϕ-meson kinematics (rapidity y and transverse momentum p_T). Therefore, the dependence of the reconstruction efficiency on y, p_T, and M is evaluated. Figure 3.39 shows the y and p_T dependence of the reconstruction efficiency at overall multiplicity, evaluated separately for the three targets. For each (y, p_T) region, the multiplicity dependence of the efficiency is shown in Fig. 3.40(a). Here, the multiplicity is defined as the number of clusters in the y strips of the GTR100 layer, whose distribution is shown in Fig. 3.41. The efficiency decreases approximately linearly with

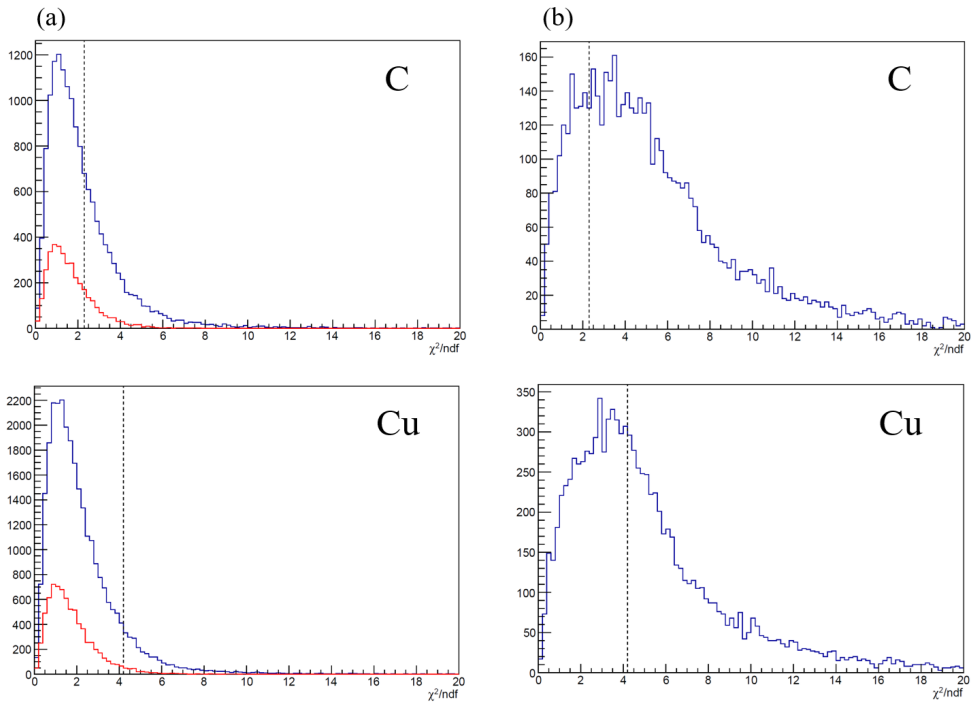

Figure 3.36: Chi-square distributions obtained by performing Runge–Kutta fitting under the requirement that plus-charge and minus-charge tracks share a common vertex. (a) Simulation; (b) Data. Distributions for the copper and carbon targets are shown separately. Dashed lines indicate the cut thresholds. See the text for the description of the red histogram.

multiplicity. Figure 3.40(b) shows the efficiencies scaled so that the efficiency becomes 1 in the most frequent multiplicity range ($25 \leqq M \leqq 32$). After scaling, the distributions are consistent with each other. Therefore, the track reconstruction efficiency $\epsilon_{\text{reconst}}$ is expressed as

$$\epsilon_{\text{reconst}}(y, p_T, M) = \epsilon(y, p_T, 25 \leqq M \leqq 32) \cdot f(M) \tag{3.12}$$

where the first term depends on (y, p_T) and the second term depends on multiplicity. A linear fit to Fig. 3.40(b) yields $f(M) = 1 - 0.01(M - 28)$. The systematic uncertainty of this correction term, obtained from the variation of the fit results across different (y, p_T) regions, is 12.3%.

This multiplicity-dependent correction factor $f(M)$ is applied to all events used in the analysis: the multiplicity is scanned for all data, and the correction factor $f(M)$ corresponding to the spill-by-spill average multiplicity is applied to the number of protons determined spill by spill. The results are described in Sec. 3.6. The term $\epsilon(y, p_T, 25 \leqq M \leqq 32)$ is obtained by applying the embedding method only to background events with multiplicity in this range. The same binning and integration region as in the data (see Sec. 4.1.1) are applied to the simulated mass spectrum. The analysis efficiency is defined as the fraction of embedded ϕ mesons that remain in the mass region.

The systematic uncertainty of the pair-reconstruction efficiency was evaluated by considering the impact of the chi-square cut shown in Fig. 3.36. The variation in the yield-to-efficiency ratio observed when the chi-square cut is slightly modified is treated as systematic uncertainty. The chi-square cut condition was scanned within the range where the yield could be evaluated (i.e., where the ϕ-meson spectrum is observed with a good signal-to-noise ratio): 2.0–2.3 for the carbon target and 4.2–7.2 for the copper target. As a result, the systematic uncertainty was evaluated to be 5% for both targets.

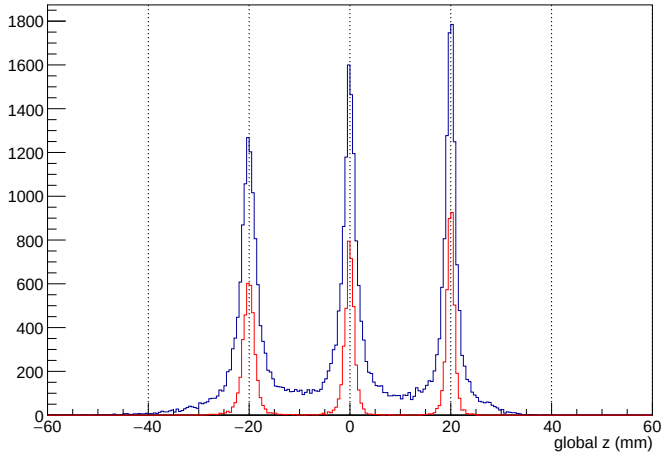

Figure 3.37: Vertex distribution obtained from simulation. The blue histogram includes tracks reconstructed using background clusters in addition to embedded clusters. The red histogram includes tracks reconstructed from only embedded clusters.

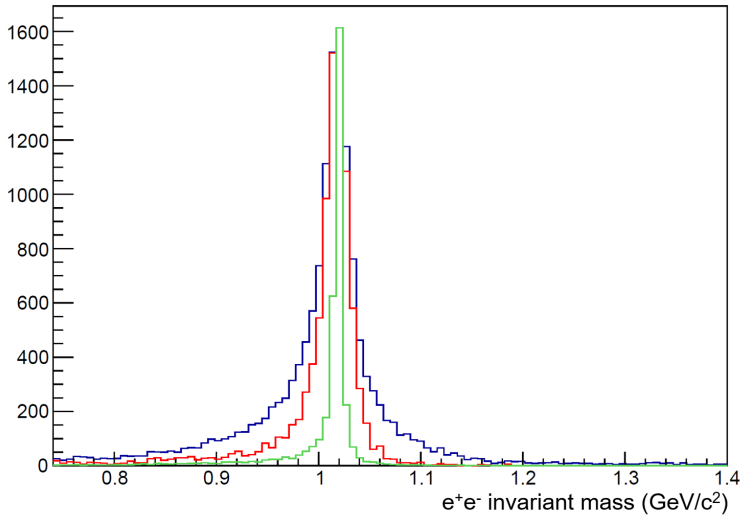

Figure 3.38: Mass spectrum obtained from simulation. The meaning of each histogram is described in the text. All histograms are normalized so that the bin with the largest number of entries has the same height.

Analysis Cut

The association efficiency on the HBD detection plane is evaluated to be 99.4%, based simply on the applied Gaussian sigma. As described in Sec. 3.4.2, the residual mean is corrected with momentum dependence, but the remaining imperfection corresponds to 0.47 sigma in local x and 0.45 sigma in local y. The resulting uncertainty in the efficiency is evaluated to be 0.6%.

The LG association efficiency is evaluated by determining whether a "track with a correlated hit" is accepted by the current clustering method. A "track with a correlated hit" is decided using the residual distribution of Fig. 3.17. The numbers of tracks are obtained after removing accidental associations using event mixing. The detection efficiency is 96% on average across modules, and the 4% variation among modules is taken as a systematic uncertainty.

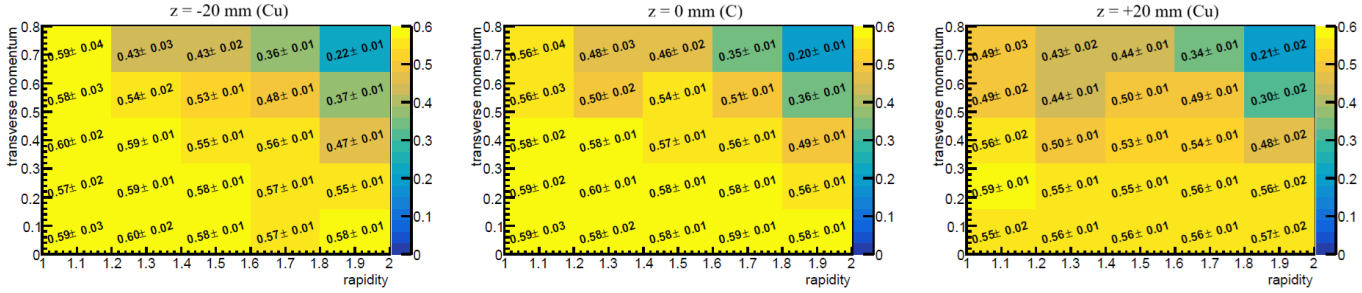

Figure 3.39: y and p_T dependence of the track reconstruction efficiency for ϕ mesons evaluated using the embedding method, shown separately for each target.

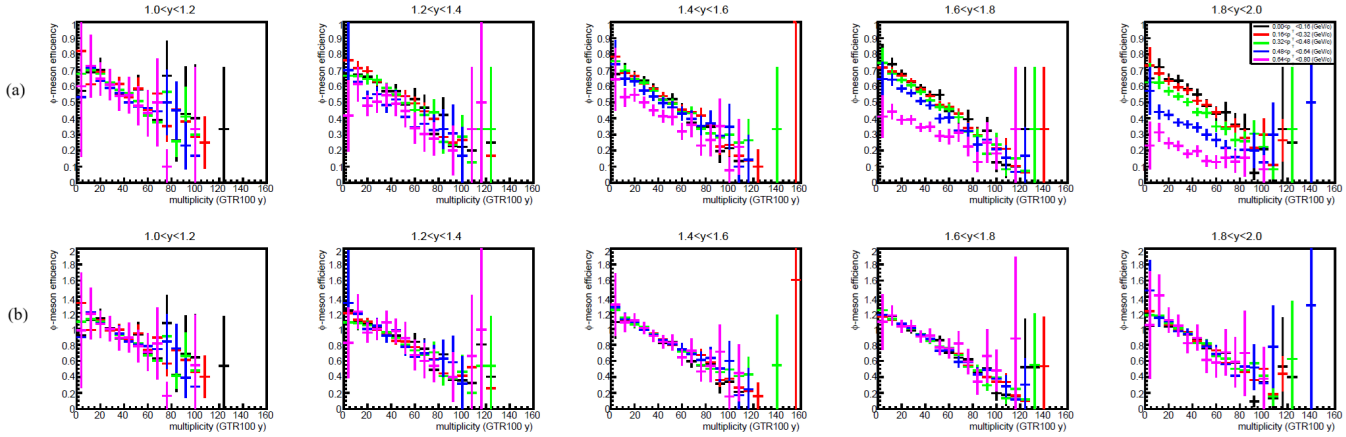

Figure 3.40: (a) Cluster multiplicity (GTR100y) dependence of the track reconstruction efficiency for the carbon target shown in Fig. 3.39. (b) Scaled efficiencies such that the efficiency becomes 1 in the most frequent multiplicity range ($25 \leqq M \leqq 32$). See text for details.

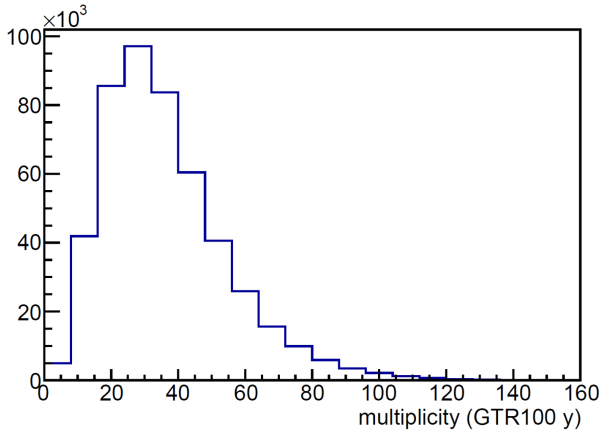

Figure 3.41: Cluster multiplicity distribution of the y strips in the GTR100 layer. The distribution shows the sum of clusters in the three forward modules for each event.

3.5.4 Summary of Efficiency

Finally, Table 3.3 summarizes the efficiencies evaluated in this section and the corresponding subsections.

Table 3.3: Summary of evaluated efficiencies.

	Cu (%) ($z = -20$ mm)	C (%) ($z = 0$ mm)	Cu (%) ($z = +20$ mm)	Referred section
Trigger efficiency	98.0	(same as left)	(same as left)	3.5.1
Detector efficiency and Acceptance	2.00×10^{-2}	1.73×10^{-2}	1.30×10^{-2}	3.5.2
Analysis efficiency	30.6	22.9	30.5	3.5.3
Total	5.99×10^{-3}	3.87×10^{-3}	3.89×10^{-3}	-

3.6 The Number of Protons

3.6.1 The number of protons together with DAQ efficiency and trigger veto

In this section, the number of protons that contributed to the production of ϕ mesons is evaluated. The number of protons irradiating the experimental targets was measured by an ion chamber. However, as mentioned in Sec. 3.5.1, to reduce fake triggers caused by collision-overlap events, a veto condition was applied such that no trigger was generated during periods when the multiplicity of trigger hits in the GTR300 layer was over 15. Therefore, protons entering during these veto periods do not contribute to the recorded data and must be excluded.

The veto periods and the LG trigger signals were recorded using a streaming TDC (HUL) [52], which preserves the time structure within each spill. It has been confirmed that the number of LG trigger hits per spill is proportional to the number of protons measured by the ion chamber [36, 37]. Thus, the time structure of the LG trigger signals is considered proportional to the beam-intensity time structure.

For the time structure of LG trigger signals obtained by the streaming TDC, the fraction of hits remaining after excluding the veto periods is defined as the veto rate. The number of protons measured by the ion chamber multiplied by (1−veto rate) is referred to as the "effective number of protons."

A similar evaluation must be applied to the DAQ efficiency. The trigger request and trigger accept signals were also recorded with the streaming TDC. The time structure is binned in 100 ms intervals, and for each bin, the effective number of protons is divided by the DAQ efficiency (trigger accept divided by trigger request). The integral of this quantity over the entire spill is defined as the "recorded number of protons."

In this measurement, the total recorded number of protons over all runs was 1.21×10^{14}. The uncertainty due to the time-structure binning is 2%, which is taken as a systematic error.

Applying the multiplicity-dependent correction factor of the track reconstruction efficiency (derived in Sec. 3.5.3) to the recorded number of protons for each spill obtains a total of 1.16×10^{14} protons over all runs. Here, all events within a spill are treated with equal weight, and the correction factor for each spill is taken as the simple average of the event-by-event correction factors.

3.6.2 Unexpected Behavior of Trigger Veto

During the data taking, an unexpected behavior occurred in the GTR multiplicity veto due to a firmware malfunction in the electronics (UT3) for determining the trigger logic. Figure 3.42 shows the GTR multiplicity distributions for runs without and with the malfunction. The normal case is shown by the blue histogram, where the distribution is cut off at the configured multiplicity limit of 15. The wrong case is shown by the red histogram.

The malfunction caused certain channels to be double-counted with some probability when a hit occurred, resulting in the veto being issued even when the actual multiplicity had not reached the limit of 15. This behavior is visible in the red histogram of Fig. 3.42.

When the malfunction was active, the trigger request rate decreased by approximately 40% compared to normal operation, the veto rate introduced in the previous subsection increased by 20%, and the DAQ efficiency increased due to the reduced request rate. As a result, the "recorded number of protons" defined earlier tended to increase. This malfunction was active in approximately 60–70% of all data used in this analysis.

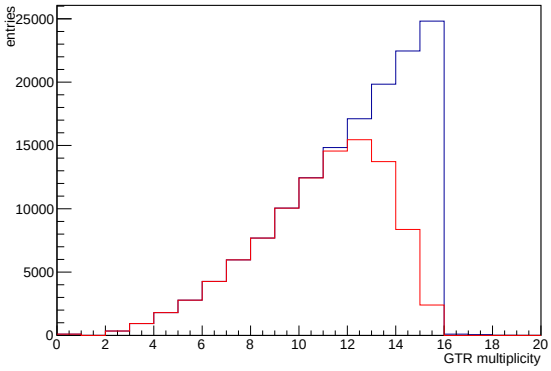

Figure 3.42: Multiplicity distribution of GTR trigger signals at trigger timing. The blue histogram corresponds to normal runs, and the red histogram corresponds to runs affected by the electronics malfunction (see text).

Although the veto condition behaved differently from the intended logic due to this malfunction, the basic behavior is not affected. Namely, no trigger is generated during veto periods even in buggy runs. Therefore, in principle, the recorded number of protons can still be calculated using the method described in the previous subsection. In this subsection, we verify that no unexpected decrease or increase in trigger efficiency was caused by the malfunction.

First, for the run sets with and without the malfunction, the number of protons corrected for the track reconstruction efficiency (derived in the previous subsection) was evaluated. The normal runs yielded 2.97×10^{13} protons, while the runs when the bug was active yielded 8.63×10^{13} protons, which is 2.9 times larger.

Next, the ω-meson mass spectra were reconstructed separately for each run set. Here, three-targets contribution is summed. Since the run dependence of the detection efficiency is corrected, the number of reconstructed ω mesons should be proportional to the recorded number of protons if no unexpected trigger-efficiency variation occurred.

Figure 3.43 shows the reconstructed spectra: (a) all runs, (b) normal runs, (c) buggy runs. The upper panels show the spectra, and the lower panels show fits using a Gaussian (signal) plus a quadratic function (background). The yield is obtained by integrating the histogram in the 0.7–0.8 GeV/c^2 region and subtracting the background contribution.

The yields are: (b) 33.6±14.4, (c) 93.2±21.5, which reproduce well the proton-number ratio of 2.9 between the two run sets. Although differences within the uncertainties cannot be

evaluated with this method, it is confirmed that there is no reduction in detection efficiency corresponding to the reduced trigger-request rate (about 60% of normal run).

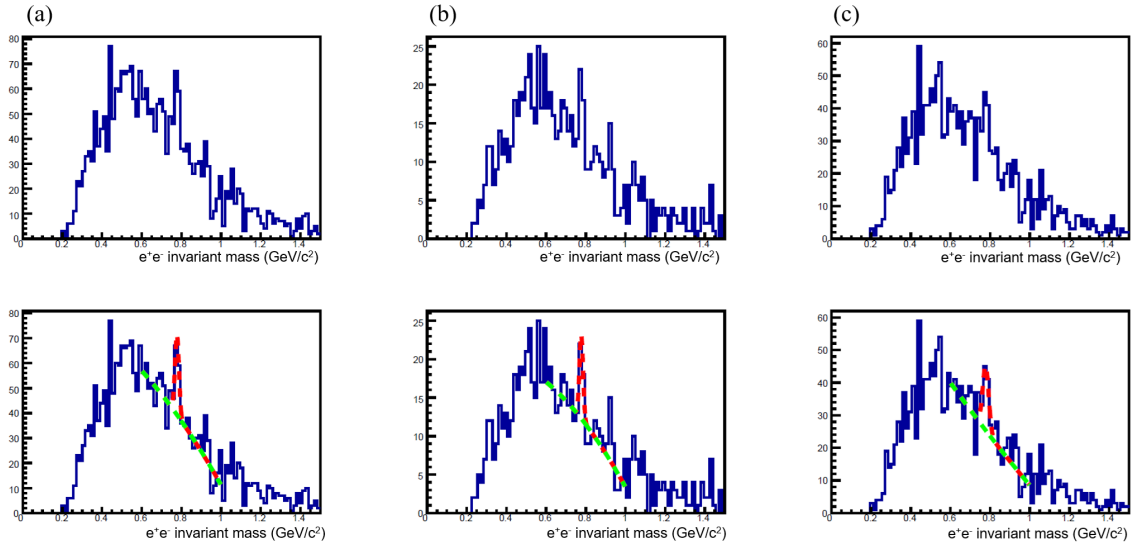

Figure 3.43: Invariant mass distributions reconstructed from electron-pair momenta. (a) All data, (b) runs with normal trigger veto operation, (c) runs affected by the trigger-veto malfunction. The lower panels show fits used to determine the ω yield (see text).

Chapter 4

Result and Discussion

4.1 Invariant Mass Spectrum

4.1.1 Evaluation of Yield

The obtained mass spectra are shown in Fig. 4.1. Here, the spectra for the copper target ($z = -20, +20$ mm) are summed. The acceptance is not corrected. A clear peak corresponding to the ϕ meson mass is observed.

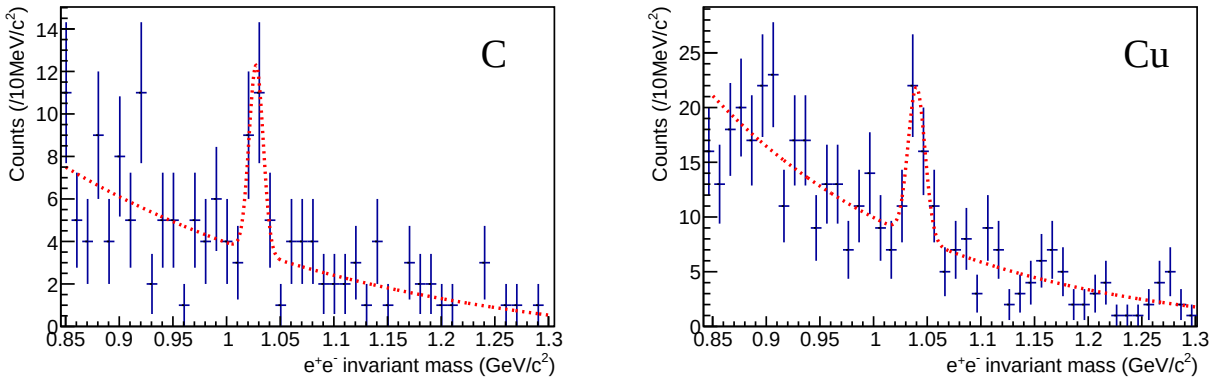

Figure 4.1: Invariant mass spectra on carbon and copper experimental targets. Red dashed lines show the fitting results. Fitting function is explained in the text.

The yield of ϕ mesons is determined by integrating the histogram and subtracting the contribution of the background. The integration range is set to ± 22 MeV/c^2 around the peak of the Gaussian fit. To determine the background distribution, the fitting was performed. The red dashed line in Fig. 4.1 shows the fitting result using a Gaussian function for the signal and an exponential function plus a constant term for the background. Six parameters were floated in this fit: the amplitude, mean and sigma of the Gaussian function; the amplitude and slope parameter of the exponential function; and the constant term. In Table 4.1, the number of signals plus backgrounds ($S + B$), backgrounds (B), and yield (S) are summarized. The qualities of the fitting, the chi-square value, and fitting probability are also presented. To show the significance of the signal, the values of $S/\sqrt{B}$ are calculated for the carbon data, the copper data, and the sum of their statistics. The $S/\sqrt{B}$ value of the sum is 4.4, supporting the conclusion that ϕ mesons are produced in 30 GeV proton-nucleus reactions.

Table 4.1: Obtained yields on carbon and copper experimental targets.

Target	$S+B$	B	$S/\sqrt{B}$	Yield (S)	χ^2/ndf	p value
C	29 ± 5.4	17.1 ± 1.5	2.9	11.9 ± 5.6	40.5/39	0.40
Cu	72 ± 8.5	48.4 ± 5.6	3.4	23.6 ± 10.2	37.8/39	0.53
C+Cu	101 ± 13.9	65.5 ± 7.1	4.4	-	-	-

Mass Spectra on Cu Targets

In the present analysis, the spectra from the two copper targets were summed in order to evaluate the yields with better signal-to-noise ratios. Figure 4.2 shows the reconstructed spectra on each experimental target located at $z = -20$ mm and $z = +20$ mm. The yields extracted from these spectra are summarized in Table 4.2, together with the efficiencies listed in Table 3.3. The sum of these yields reasonably matches the added copper yield in Table 4.1. Because the acceptance and reconstruction efficiency differ between data for two copper targets, the raw yields do not agree with each other. Table 4.2 also lists the yields divided by the efficiencies. These efficiency-corrected yields are quantitatively consistent within uncertainties, indicating that the difference in the raw yields between the two copper targets is reasonable.

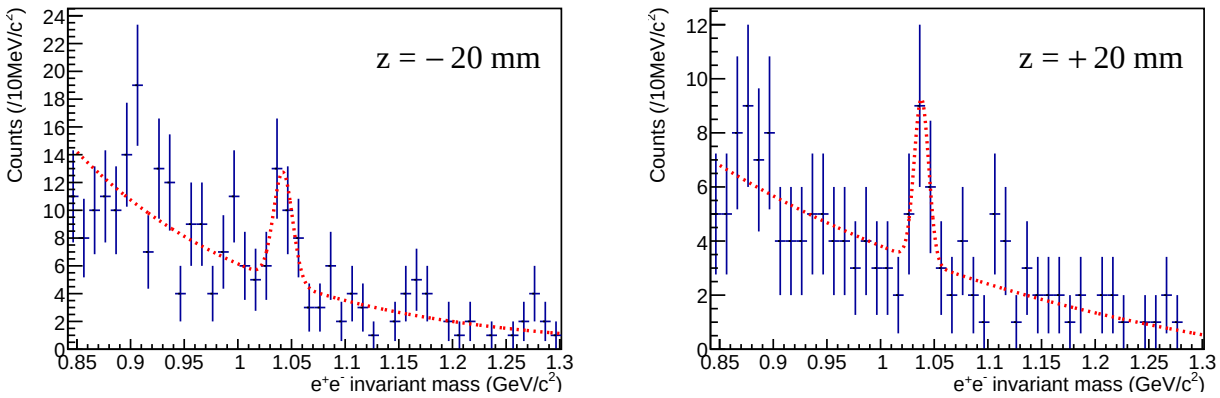

Figure 4.2: Mass spectra on two copper targets located at $z = -20$ mm and $z = +20$ mm.

Table 4.2: Obtained yields on two different copper targets are summarized. Efficiency is previously shown in Fig .3.3, and presented again here.

Target	$S+B$	B	$S/\sqrt{B}$	Yield (S)	Efficiency (%)	Yield/Efficiency
$z = -20$ mm	45 ± 6.7	29.4 ± 2.8	2.9	15.6 ± 7.3	5.99×10^{-3}	$(2.6 \pm 1.2) \times 10^5$
$z = +20$ mm	27 ± 5.2	19.2 ± 1.7	1.8	7.8 ± 5.5	3.89×10^{-3}	$(2.0 \pm 1.4) \times 10^5$

4.1.2 Systematic Errors of Yield

In this section, the uncertainties of the obtained yield are evaluated by considering the following three points:

- Effect of binning on the yield
- Effect of the background function on the yield
- Effect of the signal extraction method

First, the yield is extracted using the same method as in Sec. 4.1.1 for histograms obtained by shifting the center of each mass histogram bin by 1 MeV/c^2. If the fit probability is smaller than 5%, the fitting is regarded as inappropriate to describe the data and is excluded from the error evaluation. The systematic error is taken as the maximum deviation from the yield evaluated in Sec. 4.1.1. Figure 4.3 shows the mass distributions for the copper target when shifting the bin centers. The bins contributing to the integration are filled in light blue. The results of the systematic error evaluation are summarized in Table 4.3 at the end of this section.

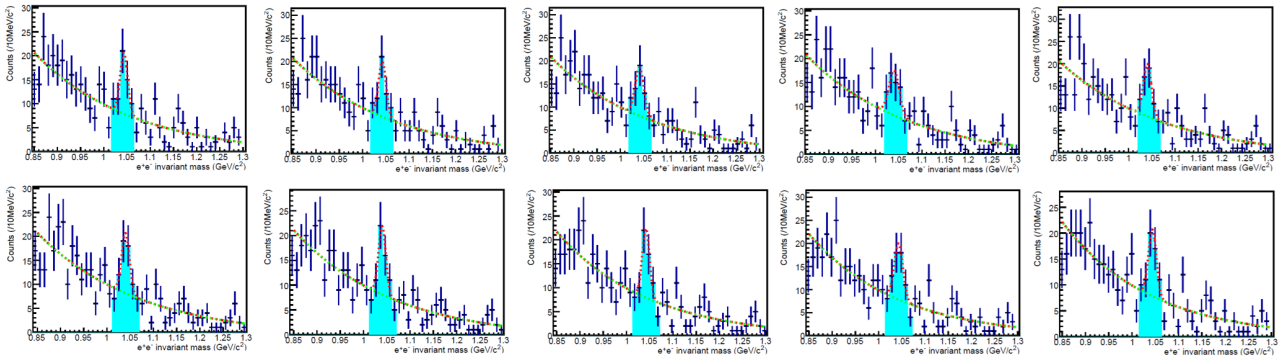

Figure 4.3: Mass spectra reconstructed for the copper target. Ten histograms obtained by shifting the bin center by 1 MeV/c^2 are shown. The bins contributing to the yield evaluation are filled in light blue.

Next, the contribution of the background distribution is examined. The distributions obtained by applying a quadratic function as the background function and by using the event mixing method are shown in Fig. 4.4. A Gaussian distribution is used as the signal distribution as before. The event mixing is performed using all tracks in the mass region used in this analysis. In the mixing, the pairs reconstructed in the ϕ mass region are scaled down according to the signal-to-noise ratio evaluated from the data. As the systematic error due to the background shape, the difference in yield between the cases using the above two background distributions and the exponential function is adopted. This contribution is smaller than the binning error.

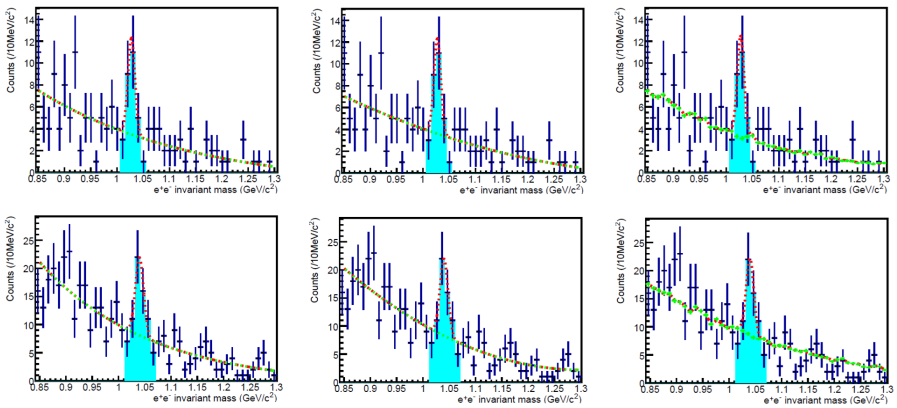

Figure 4.4: Fitting results using three different background distributions for the spectra obtained for the carbon and copper targets. The upper panels show the spectra for the carbon target, and the lower panels show those for the copper target. The left panels show the case using an exponential function as the background, the middle panels show the case using a quadratic function, and the right panels show the case using the distribution created by the event mixing method.

Up to this point, the yield has been derived by subtracting the background contribution from the obtained mass histogram. Next, a more realistic spectral shape of the ϕ meson

is introduced to evaluate the yield. In the simulation introduced in Secs. 3.5.2.5 and 3.5.3, the spectral shape is obtained by considering the internal radiative correction, energy loss in the target and detectors, and the effect of cluster merging under high background conditions for ϕ mesons generated based on the momentum distribution from the event generator JAM. The resulting spectrum is shown by the blue line in Fig. 3.38. The fitting results using this spectral shape for the experimental data are shown in Fig. 4.5. As the background distribution, exponential function is applied. The yield evaluated by this fitting method is compared with

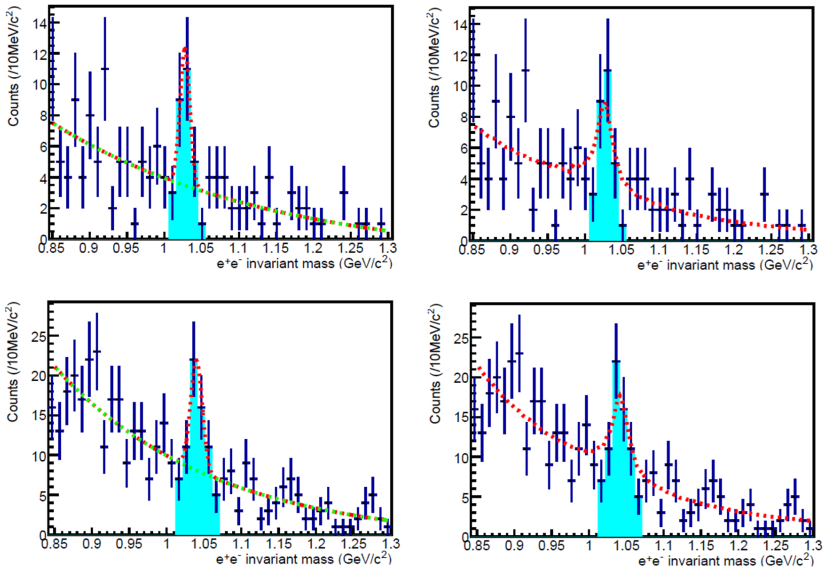

Figure 4.5: Fitting results using different signal distributions for the spectra obtained for the carbon and copper targets. The upper panels show the spectra for the carbon target, and the lower panels show those for the copper target. The left panels show the case using a Gaussian as the signal distribution, and the right panels show the case using the distribution obtained from the simulation with the embedding method.

the yield derived in Sec. 4.1.1. In the method of Sec. 4.1.1, a specific mass region is applied as the integration range. For the simulation spectral shape, the histogram with the same binning and integration region as the data yield evaluation is shown in Fig. 4.6 with the region filled in light blue. In this figure, the mass values on the horizontal axis are shifted so that the peak position of the Gaussian fit of the data matches that of the simulation (see Sec. 4.1.3 for details). The yield derived in Sec. 4.1.1 corresponds to the entries in this region. When the yield is derived using the fitting with the simulation spectral shape, the total entries of the shape are obtained as the fit result, but only the entries in the region shown in Fig. 4.6 are regarded as the yield. Using this method, the yield for the carbon target increases from 11.9 to 17.2, and that for the copper target increases from 23.6 to 32.1. The simulation shape suggests that the spectrum has a tail component arising from several effects, including internal radiative correction, energy loss, and cluster merging or mis-association of background clusters, as shown in Fig. 3.38. The Gaussian and background fitting used above may underestimate the yield because this tail component is absorbed into the background. Therefore, the yield derived by the method shown in this section is also considered as a systematic error.

The systematic errors evaluated in this section —those due to binning, background distribution, and assumed signal shape— are summarized in Table 4.3.

4.1.3 Remarks on the Mass Centroid and Width

Up to this point, the evaluation has focused on the yield of ϕ mesons. In this section, the precision of the mass reconstruction of the ϕ meson in this analysis is discussed. The results of

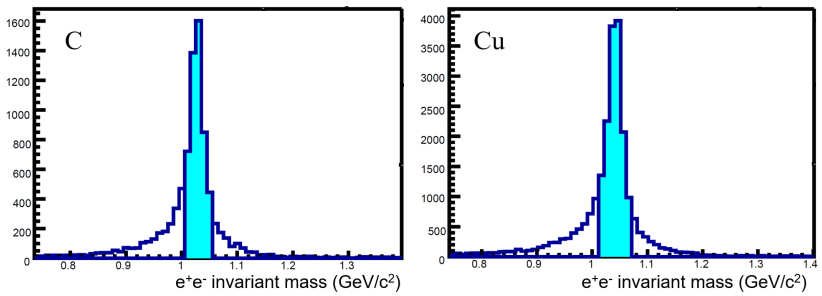

Figure 4.6: Mass spectrum reconstructed in the simulation, with the mass region contributing to the yield evaluation in Sec. 4.1.1 filled in light blue.

Table 4.3: Summary of systematic errors of the yield. For reference, the first row shows the yield.

	C	Cu
(yield)	(11.9)	(23.6)
binning	1.8	5.3
background function	0.4	1.0
signal extraction	5.2	8.5

the Gaussian fitting shown in Fig. 4.1 are summarized in Table 4.4. In addition to the fitting uncertainties shown in this table, there are uncertainties due to the inaccuracy of the geometry correction and the vertex position determination. As shown in Sec. 3.3.2, the geometry correction in this evaluation is performed only at the module level, and there remains an uncertainty of up to ±2 mrad in the relative opening angle due to the misalignment between different modules, which affects the mass reconstruction by up to 6 MeV/c^2. Furthermore, Fig. 3.18(b) shows the vertex distribution reconstructed from the data, which deviates by up to 0.7 mm from the designed target position. To evaluate the effect of the shift of the vertex position on the mass spectrum, the simulation was performed by applying the pair fitting method with a vertex position shifted from the decay point. A shift of 0.7 mm in the global z direction corresponds to a mass-offset of 21 MeV/c^2 in the mean of the Gaussian fit of the mass spectrum, therefore the current mass determination has an estimated uncertainty of about 2%. However, the effect of this vertex shift on the yield is less than 1%, as evaluated from the simulation. Since the main objective of this analysis is the evaluation of the cross section, the impact of this uncertainty of mass reconstruction on the result is small.

The sigma values in Gaussian function shown in Table 4.4 include both the natural width of the ϕ meson and the effect of the spectrometer resolution. In addition to the fitting uncertainties shown in Table 4.4, the sigma value varies by up to 3 MeV/c^2 depending on the choice of bin center, as shown in Fig. 4.3. On the other hand, applying a Gaussian fit to the mass centroid in the simulation shown in Fig. 3.38 gives a width of 13 MeV/c^2, which is slightly larger than the distribution in the data even considering the uncertainties. However, since the fitting succeeds as shown in Sec. 4.1.2, it is difficult to discuss the width precisely with the limited statistics of the present data. The effect on the yield has already been considered as a systematic error in Sec. 4.1.2.

Table 4.4: Summary of the fitting results in Fig. 4.1. The parameters of the Gaussian distribution used as the signal are shown.

	mean (MeV/c^2)	sigma (MeV/c^2)
C	1028 ± 3	7 ± 2
Cu	1040 ± 3	8 ± 3

4.2 Total Cross Section

In this section, the total production cross section of the ϕ meson is estimated using the kinematic distributions of ϕ mesons generated by the event generator JAM, which successfully describes the kinematic distribution at a nearby beam energy 12 GeV [53].

The total cross section is calculated using the following equation:

$$\sigma^{\mathrm{C/Cu}} = \frac{N_{\mathrm{yield}}^{\mathrm{C/Cu}}}{N_{\mathrm{beam}} \cdot N_{\mathrm{target}}^{\mathrm{C/Cu}} \cdot \varepsilon^{\mathrm{C/Cu}} \cdot R}. \tag{4.1}$$

The definitions of the notations and the corresponding sections are as follows:

- N_{yield}: yield (evaluated in Sec. 4.1.1)
- N_{beam}: number of recorded protons (evaluated in Sec. 3.6)
- N_{target}: number of target nuclei per unit area (described in Sec. 2.3)
- ε: detector acceptance and detection efficiency (evaluated in Sec. 3.5)
- R: e^+e^- branching ratio of the ϕ meson (taken from Ref. [15])

The quantity ε represents the fraction of JAM-generated ϕ mesons that enter the detector acceptance and are detected, taking into account the position-dependent detection efficiency. As discussed in Sec. 3.5, at the trigger level, the detection efficiency in this measurement exhibits a position dependence, which is evaluated together with the detector acceptance. For the Cu target, the yield is obtained by summing the yields from the two experimental targets. Accordingly, ε is also taken as the simple sum of the acceptances for the individual targets, as expressed below:

$$\varepsilon^{\mathrm{Cu}} = \varepsilon^{\mathrm{Cu}(z=-20\mathrm{mm})} + \varepsilon^{\mathrm{Cu}(z=+20\mathrm{mm})}. \tag{4.2}$$

The kinematics of the ϕ mesons generated by the event generator JAM are shown in Fig. 4.7. Here, as described in step 1 of Sec. 3.5.2.5, the kinematics before the decay routine of the ϕ meson is recorded. That is, ϕ mesons that react with the target nucleus inside JAM are considered undetectable, and the total cross section is calculated accordingly. The kinematic region covered by the present acceptance is shown in Fig. 3.28, which covers rapidity of about 1–2 and transverse momentum of about 0–1 GeV/c.

Assuming this kinematics, $\varepsilon^{\mathrm{C/Cu}}$ are determined and the obtained yields are converted into total cross sections following Eq. 4.1. The results are shown in Table 4.5. From the ratio of the obtained cross sections, $\alpha = 0.99 \pm 0.38$ (stat.) $\pm$ 0.34 (syst.) is evaluated. Although the uncertainties are large, the present result supports $\alpha \sim 1$, meaning that the cross section is proportional to the mass number.

Table 4.5: Estimated total cross sections on carbon and copper targets.

	Total cross section (mb)
C	2.0 $\pm$ 0.9 (stat.) $\pm$ 1.0 (syst.)
Cu	10.3 $\pm$ 4.4 (stat.) $\pm$ 4.4 (syst.)

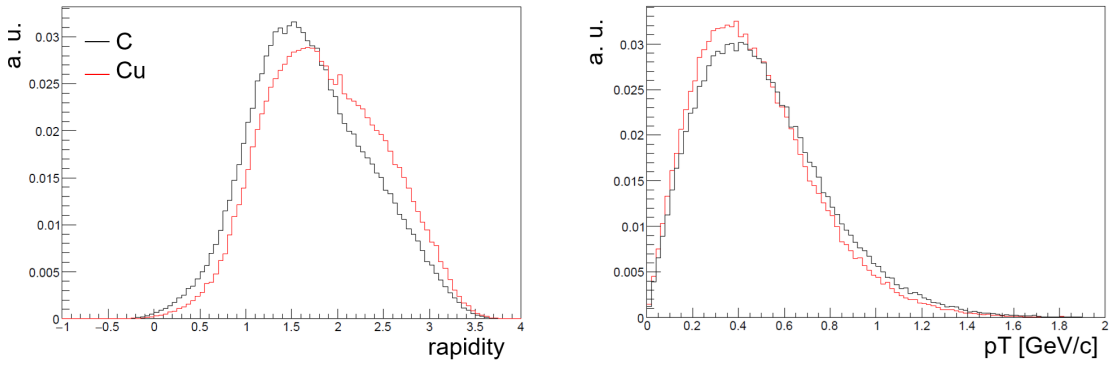

Figure 4.7: Momentum distributions of the ϕ mesons generated by JAM (see text for details). The rapidity distribution is shown on the left, and the transverse momentum distribution is shown on the right. The black line shows the distribution for the carbon target, and the red line shows that for the copper target.

4.3 Systematic Uncertainties

In this section, the systematic uncertainties of the yield, beam intensity, number of target nuclei, branching ratio, and efficiency are summarized. Table 4.6 shows the values of the systematic uncertainties and the sections where they were evaluated. For the analysis cuts, the systematic uncertainties of the association efficiency evaluated from the residual distribution of the data in Sec. 3.5.3 and the efficiency of the ADC cut in the STS are considered. The yield and target thickness are evaluated separately for the carbon and copper targets. The other items are common between the targets. For the evaluation of the cross-section ratio (α parameter), only the first two items in Table 4.6 will be considered. The total uncertainty is calculated as the square root of the sum of squares of the relative uncertainties shown in Table 4.6.

Table 4.6: Summary of systematic uncertainties for the total cross sections.

	Error for C (%)	Error for Cu (%)	Section
Yield	44	36	4.1.2
Target thickness	0.1	0.1	2.3
Branching ratio	1.1 [15]	(same as left)	-
Beam intensity	10	(same as left)	3.6
DAQ efficiency with trigger veto	2	(same as left)	3.6
Trigger efficiency	1	(same as left)	3.5.1
Track reconstruction	13	(same as left)	3.5.3
Analysis cut	6	(same as left)	3.5.3, 3.5.2.1
Electron identification	6	(same as left)	3.5.2.3, 3.5.2.4
Acceptance	13	(same as left)	3.5.2.6
Total	50	43	-

4.4 Discussions

4.4.1 Mass Number Dependence

The mass-number dependence of the obtained total cross sections is shown in Fig. 4.8. The horizontal axis shows the mass number, and the vertical axis shows the cross section. A linear

extrapolation of the two measured cross sections toward the low-mass-number region is shown by the red dashed line. Although no other data exist at the 30 GeV energy region, there are experiments using proton beams with momenta of 24 GeV/c [53] and 40 GeV/c [54] that measured ϕ-meson production in proton-proton reactions. These results are indicated by the blue triangle (24 GeV/c) and the green inverted triangle (40 GeV/c). The NA61/SHINE experiment used data in the center-of-mass energy range $\sqrt{s_{NN}} = 6.8$–52.5 GeV [8] and performed a simple linear extrapolation of the production cross section to the energy corresponding to 30 GeV ($\sqrt{s_{NN}} = 7.7$ GeV). The result is shown by the orange star. These values are summarized in Table 4.7.

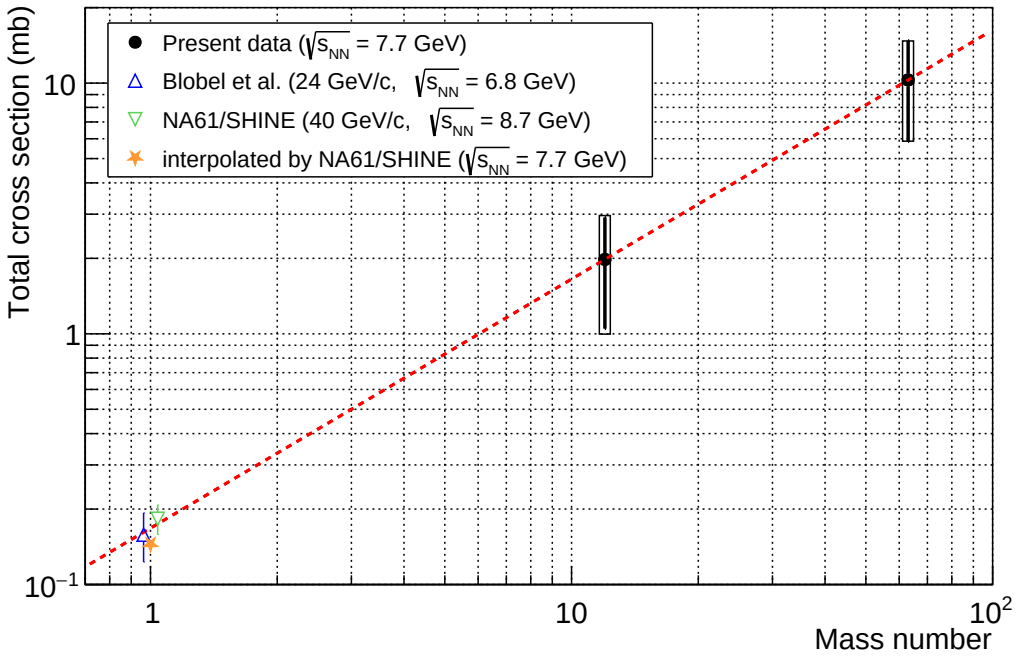

Figure 4.8: Mass-number dependence of the total ϕ-meson production cross section obtained in this measurement and estimated from the kinematics predicted by JAM. The black points show the measured results, with statistical uncertainties shown by black bars and systematic uncertainties shown by black boxes. The red dashed line shows the extrapolation toward the low-mass-number region from the two measured data points. Other symbols are described in the text.

Table 4.7: Total cross sections of the proton-proton collisions measured by other experiments.

	Total cross section (mb)
$\sqrt{s_{NN}} = 6.8$ GeV (24 GeV/c) [55]	0.158 ± 0.035
$\sqrt{s_{NN}} = 7.7$ GeV [8]	0.145
$\sqrt{s_{NN}} = 8.7$ GeV (40 GeV/c) [8]	0.183 ± 0.025

In addition, the α parameter obtained in this measurement is compared with results measured at other energies. The results are summarized in Table 4.8. Here, only data measured via the dilepton decay channel, which is free from final state interactions with the nucleus, are shown. These results both at higher and lower collision energies than the present measurement consistently support a value of $\alpha \sim 1$.

Table 4.8: Comparison of the α parameter with different production energies.

Beam energy (GeV)	α
12 [53]	$0.937 \pm 0.049 \pm 0.018$
30	$0.99 \pm 0.38 \pm 0.34$
400 [54]	$0.906 \pm 0.011 \pm 0.025$

The result of $\alpha \sim 1$ indicates that the production of ϕ mesons tends to scale proportionally with the number of nucleons. In the present measurement, the cross sections were obtained for A=12 and A=63. As shown in Fig. 4.8, the results at nearby production energies for A=1, i.e., proton-proton (pp) reactions, also follow the same tendency (the red dashed line). This suggests that the ϕ-meson production cross section in pA reactions can be described as a simple mass-number scaling of the pp production cross section. In pp reactions, unlike in pA reactions, the generated ϕ-meson does not interact with spectator nucleons in principle. The fact that the pA results follow the mass-number scaling of the pp reaction implies that, even in pA collisions, ϕ-mesons are produced according to the nuclear density distribution and that absorption effects by the spectator nucleons are small. This indicates that the suggested strong absorption of ϕ-mesons presented in Sec. 1.3.3 is less significant in the present measurement. This difference may originate from the decay channel under observation: the present measurement is based on the dilepton decay mode, whereas the COSY-ANKE experiment [11], which reported indications of absorption, measured the K^+K^- decay channel. However, the JLab CLAS measurement of the transparency ratio [25], although photon-induced, also suggested absorption through the dilepton decay channel, leaving room for further discussion. In any case, the present results suffer from large statistical and systematic uncertainties, and the extrapolation to the pp cross section also includes substantial uncertainty. Therefore, more precise measurements are essential for a quantitative discussion of absorption effects.

4.4.2 ϕ-meson Production Mechanism

In this section, the total cross sections obtained from the data are compared to the simulation results by JAM. Table 4.9 summarizes the comparison between the data and the JAM calculation. Here, as mentioned in Sec. 4.2, ϕ mesons in JAM immediately before the decay routine are recorded in this simulation. Therefore, in the simulation value shown in Table 4.9, ϕ mesons that are produced but subsequently interact with other hadrons (or are absorbed) are not counted.

Table 4.9: Comparison of the total cross-section and α parameter between the data and JAM simulation.

	Cross section for C (mb)	Cross section for Cu (mb)	α
Data	$2.0 \pm 0.9 \pm 1.0$	$10.3 \pm 4.4 \pm 4.4$	$0.99 \pm 0.38 \pm 0.34$
Simulation	1.08	6.75	1.11

In JAM, when the center-of-mass energy of the two-body system is greater than $\sqrt{s} = 7.7$ GeV, hadrons are produced through soft string excitation based on the HIJING model [56], followed by string hadronization according to the Lund string model including quark-antiquark production based on the Schwinger mechanism. Overall, the measured cross sections agree with the JAM predictions within the experimental uncertainties, supporting the production mechanism implemented in JAM. However, the data tend to be systematically larger than the model values, which may indicate the presence of an additional production component. It must be carefully considered, because an excess of strangeness production is expected to serve as

Table 4.10: Comparison of the estimated total cross section based on the two different kinematic distributions. The first uncertainty represents the statistical error, and the second represents the systematic error.

	Cross section for C (mb)	Cross section for Cu (mb)	α
JAM	$2.0 \pm 0.9 \pm 1.0$	$10.3 \pm 4.4 \pm 4.4$	$0.99 \pm 0.38 \pm 0.34$
PHSD	$2.4 \pm 1.1 \pm 1.2$	$13.2 \pm 5.7 \pm 5.7$	$1.04 \pm 0.38 \pm 0.34$

a signal of various underlying QCD physics, as referred in Sec. 1.3.2. Future high-statistic measurements will be essential for providing more precise data for a more detailed discussion of the production mechanism.

In the present measurement, we determined the production cross section of the ϕ meson, which is particularly sensitive to strangeness production from the vacuum. At the same time, the same di-electron decay channel also allows the detection of ρ/ω mesons. In this energy region, ρ/ω mesons are expected to be produced through string-based mechanisms similar to the ϕ meson; however, because u and d quarks are already present in the initial state, additional production processes obviously contribute. A future measurement of the α parameter for ρ/ω mesons would therefore be valuable for identifying the dominant production mechanisms. Furthermore, comparing the yield ratio of ρ/ω to ϕ mesons with existing model predictions may provide insight into the relative production probabilities of u, d and s quarks in string-based models.

4.4.3 Effect of Kinematic Assumptions on the Cross Section

In the present analysis, the total cross section is estimated assuming the kinematics provided by JAM. To examine the validity of this assumption, we also simulated ϕ-meson production in 30 GeV pA reactions using another transport model, Parton-Hadron-String Dynamics (PHSD) [57, 58], and derived the corresponding kinematic distributions to compare the resulting cross sections. The PHSD, which can treat off-shell particles, is considered a promising transport model for future investigations of mass modification in the J-PARC E16 experiment. In this work, however, it is used solely to discuss the model dependence of the results. The detailed simulation conditions of PHSD used in this analysis are described in Ref. [59].

The kinematic distributions obtained with PHSD are shown by the red lines in Fig. 4.9. For comparison, the JAM-based kinematic distributions shown previously in Fig. 4.7 are displayed in black. Here, the center-of-mass rapidity $y_{\mathrm{c.m.}}$ becomes zero at $y = 2.09$ in this 30 GeV collisions.

While the shapes of the p_T distributions reasonably agree, the rapidity distributions exhibit noticeable differences. These differences are discussed later. Using the PHSD-based kinematic distributions, the acceptance and detection-efficiency factor ε was evaluated, and the resulting cross sections are summarized in Table 4.10. Although the detector acceptance of the present measurement covers the rapidity region around $y \sim 1.7$ (see Fig. 3.28), which corresponds to the region where the kinematic distributions differ between the models in Fig. 4.9, the resulting model dependence of the estimated cross sections is smaller than the experimental uncertainties. The impact on the present results is not significant.

In Fig. 4.10, the PHSD-based total cross sections are overdrawn on the JAM-based total cross sections shown in Fig. 4.8. The PHSD-based results do not significantly change the previous discussion regarding the value of the α parameter and the extrapolation to the pp reaction. Although this comparison involves only two models, the uncertainty arising from the assumed kinematics is smaller than the experimental uncertainties, and the conclusions drawn in the previous subsection remain unchanged. Thus, the impact of the assumed kinematics on

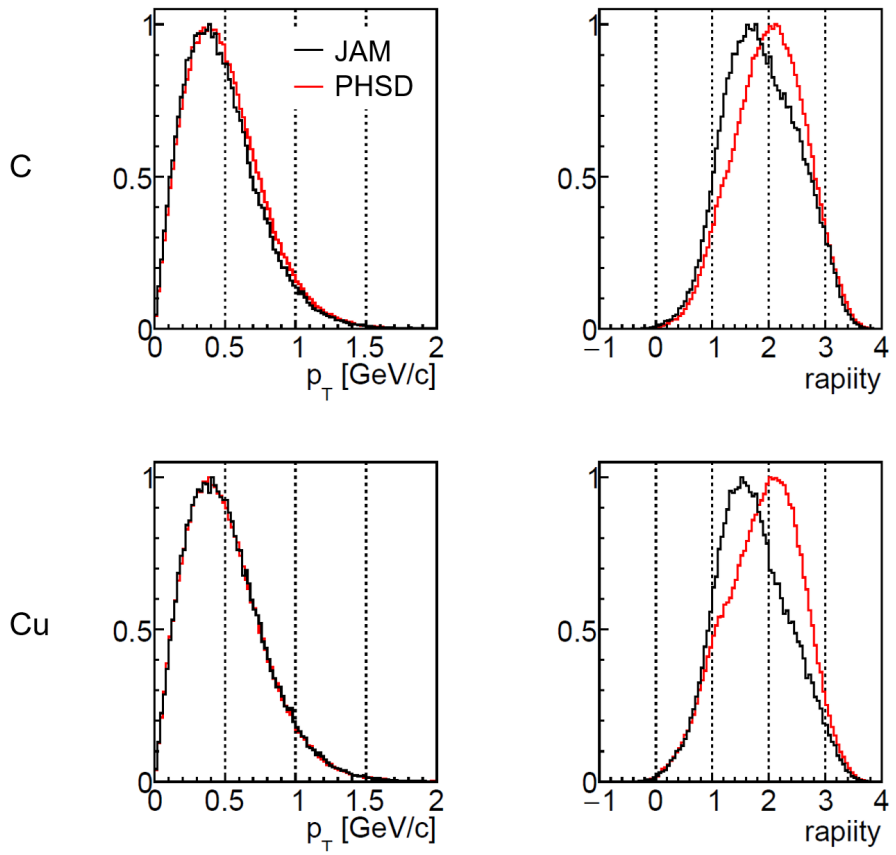

Figure 4.9: Comparison of JAM-based and PHSD-based kinematics. The upper panels show the results for the carbon target, and the lower panels show those for the copper target.

the present results is estimated to be small.

In the future, collecting higher-statistics data will allow the kinematic distributions to be derived directly from the measurements, enabling the evaluation of the differential cross section that does not depend on model assumptions.

4.4.4 Impact of the Present Study

In the present study, the first physics results obtained using the newly constructed beamline and spectrometer. The achievements are as follows:

1. Establishment of a system for detecting di-electron decays of vector mesons at the J-PARC high-momentum beamline.
    - Stable operation of detectors and electronics under high-rate and high-radiation conditions.
    - Successful operation of the di-electron trigger under huge hadronic backgrounds, enabling reconstruction of ϕ-meson mass spectrum with satisfactory signal-to-noise ratio.
    - Sufficient track reconstruction under high-multiplicity conditions.
    - Confirmation of acceptable beam operation, considering the time structure, profile, and effects of the beam halo and background particles produced by the beam loss near the spectrometer.
2. Establishment of a evaluation method of the production cross section.

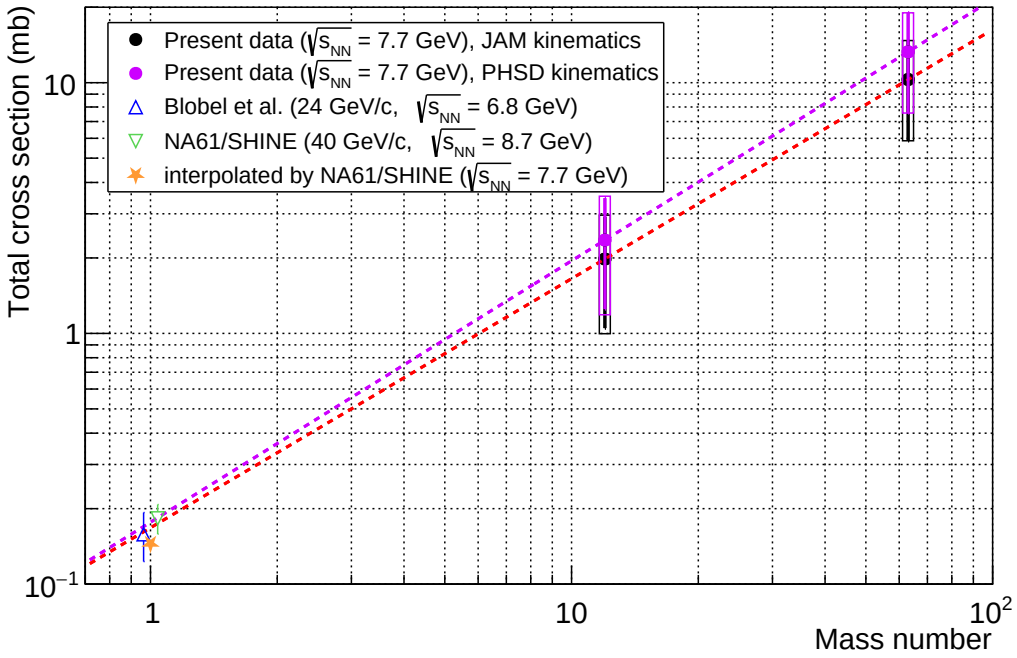

Figure 4.10: The PHSD-based total cross sections are added as purple points to Fig. 4.8. All other plots are the same as in Fig. 4.8.

The first achievement provides a demonstration of the feasibility of future experiments planned at this beamline. The capability to perform reasonable di-electron measurements under high-background conditions, which is an essential technique for the J-PARC E16 experiment, was successfully demonstrated in this study. In addition, di-electron measurements will also be a key technique for the future J-PARC HI project. Furthermore, as discussed in Sec. 2.2, the observed time structure of the beam is considered to originate from the MR power supply and the beam optics at the branching point to the high-momentum beamline, providing useful insight for the operation of future secondary beamline.

The second achievement provides new information on strange hadron production at intermediate energies. This study was performed using pilot data from the E16 experiment, while cross-section evaluation is not strictly required for the primary physics goals of E16. Deriving the cross section allows us to obtain information on the ϕ-meson production mechanism through the α parameter, and enables discussion of the production processes by comparing the measured cross sections with various model calculations. ϕ-meson production in proton-nucleus collisions is valuable both as a baseline for heavy-ion collisions and as a probe of small collision systems; however, it is not included in the ongoing intermediate-energy collision programs, and thus provides unique information. In addition, understanding the production process is important for estimating the density at which the ϕ-meson mass modification may occur in the E16 experiment.

Since November 2025, the E16 experiment has begun data taking for the physics. The precedent experiment, KEK-PS E325, collected 2400 ϕ mesons for a copper target, and the E16 experiment aims to exceed this statistics already in the first stage (Run 1). The cross section derived in the present study suffers from large statistical uncertainties and model dependence in the estimation of the momentum distribution; however, these uncertainties will be reduced as more data for the E16 experiment are accumulated. As discussed above, precise cross-section data is a promising observable, and establishing the basis for the evaluation in the present study

is of considerable significance.

Chapter 5

Conclusion

In the present study, we report the first measurement of ϕ-meson production in reactions of a 30-GeV proton beam on carbon and copper nuclear targets via the di-electron decay channel at J-PARC. The corresponding center-of-mass energy region, $\sqrt{s} = 7.7$ GeV, has recently attracted considerable interest in heavy-ion collisions due to its significance to the study of QCD matter at intermediate temperature and high baryon density. In such collisions, hadron production involving strangeness is regarded as a key signature of the QCD phase structure. Therefore, understanding the elementary production mechanisms in this energy region is essential. However, because the energy is close to the lower applicability limit of perturbative QCD, yet high enough that the resonance-production picture begins to break down, the production mechanism is nontrivial, making the experimental input particularly important.

Measurements of the mass-number dependence provide insight into the production process: the behavior of α allows one to deduce whether the production is uniform ($\alpha \sim 1$), surface-dominated ($\alpha \sim 2/3$), or of a different nature. Furthermore, in measurements of production cross sections on nuclear targets, the detected ϕ mesons are expected to have undergone interactions with the nuclear medium, making the results possibly sensitive to in-medium effects. From this perspective, the dilepton decay channel used in this work is particularly valuable, as it is free from final-state strong interactions with the nuclear medium and thus provides clean experimental information.

This measurement was performed using the newly constructed high-momentum beamline and the E16 spectrometer optimized for di-electron detection, for the first time. Many experiments are planned in this beamline, including the first program of the J-PARC E16 experiment that will perform high-statistics measurements of the ϕ-meson spectral shape in nuclei. In particular, detecting di-electron decays of vector mesons, which have small branching ratios, under the large hadronic background produced in proton-nucleus collisions is experimentally challenging. Because such dileptons carry valuable information and existing measurements are poor, establishing this technique is of significant importance.

For the present analysis, pilot data from the E16 experiment, corresponding to 2.28×10^4 spills (26.8 hours), were used. Electron identification was performed using two types of electron identification detectors at both the online and offline levels. The invariant mass of e^+e^- pairs was reconstructed using the Runge–Kutta fitting method applied to position data from the four-layer tracking system and the known target position. The beam intensity was evaluated as the integrated number of protons during periods in which triggers were generated (referred to as "effective protons"). After further accounting for the DAQ efficiency, the number of recorded protons was estimated to be 1.21×10^{14}.

As a result, the first successful reconstruction of the ϕ-meson invariant mass via the di-electron decay using the new beamline and spectrometer was achieved, as indicated by a statistical significance of $S/\sqrt{B} = 4.4$ when summing over all targets. We observed the ϕ mesons of 11.9 ± 5.6 (stat.) ± 5.2 (syst.) from the carbon target and 23.6 ± 10.2 (stat.) ± 8.5 (syst.) from the copper target. Most of the systematic uncertainty arises from uncertainties in extracting the yields from the mass spectra. The obtained yields were converted into total cross sections by assuming the kinematical distributions predicted by the event generator JAM. The resulting total cross sections are 2.0 ± 0.9 (stat.) ± 1.0 (syst.) mb for carbon and 10.3 ± 4.4 (stat.) ± 4.4 (syst.) mb for copper.

Using the parameterization α, we obtained $\alpha = 0.99 \pm 0.38$ (stat.) ± 0.34 (syst.). Although the uncertainties are large, this value is consistent with previous measurements using 12-GeV and 400-GeV proton beams. Moreover, the production cross section extrapolated to $A = 1$, i.e., proton-proton collisions, agrees well with results from other experiments at comparable energies. These results suggest that the mass-number dependence of ϕ-meson production is a scaling of the proton-proton production. This implies a picture in which ϕ mesons are produced according to the nuclear density distribution and are detected with little absorption.

The absolute values of the extracted cross sections were compared with predictions from two event generators. The results agree within uncertainties, supporting the picture implemented in the generators in which strings excited by soft valence-quark scattering hadronize via string fragmentation. At the same time, the experimental values tend to be systematically larger than the simulations, while remaining consistent within one standard deviation. Future higher-statistics measurements will enable further discussion of the possible contribution of additional production mechanisms.

Appendix A

Run List Used in the Analysis

The following runs were used in the analysis.

51271	51388	51389	51390	51391	51395	51396	51399	51430	51431
51432	51433	51434	51435	51436	51437	51438	51440	51441	51442
51445	51447	51450	51451	51454	51455	51456	51457	51467	51470
51471	51473	51479	51481	51532	51536	51537	51538	51539	51540
51541	51543	51544	51545	51550	51551	51552	51553	51554	51571
51576	51577	51578	51579	51581	51585	51586	51587	51589	51590
51594	51613	51614	51615	51616	51628	51629	51630	51636	51637
51639	51640	51647	51649	51651	51653	51654	51655	51657	51659
51660	51662	51666	51667	51668	51669	51670	51674	51675	51687
51690	51691	51692	51694	51695	51700	51703	51704	51706	51707
51709	51710	51713	51715	51717	51719	51731	51733	51734	51735
51738	51739	51740	51741	51742	51744	51745	51746	51760	51761
51768	51770	51774	51775	51777	51779	51844	51845	51847	51864
51865	51866	51869	51870	51871	51882	51883	51885	51887	51888

Acknowledgement

This research has been accomplished thanks to the support of many people, to whom I would like to express my sincere gratitude.

First and foremost, I am deeply grateful to my supervisor, Prof. Megumi Naruki, who gave me the opportunity to join the E16 experiment and has guided me from my master's program through the completion of this thesis. Although I was inexperienced in many respects, she always respected the autonomy of her students and provided an environment that allowed me to take initiative in my research. She also offered invaluable advice that helped me move my research forward. This thesis could not have been completed without her continuous support.

I would like to express my sincere appreciation to Dr. Satoshi Yokkaichi, spokesperson of the E16 experiment, for giving me the opportunity to work together on the experiment and for providing extensive support throughout the progress of my research. His careful comments and advice helped me identify many points I had overlooked and provided essential advice that enabled me to finalize this thesis.

I am also deeply indebted to Dr. Yuhei Morino, whose essential and precise guidance at every stage of the analysis made it possible for the work to proceed smoothly without encountering serious difficulties. My sincere thanks go to Dr. Kazuya Aoki for his support in all aspects of the E16 experimental site and for patiently answering my daily questions regarding the physics of E16 and related topics. He also made direct contributions to the operation and analysis of the silicon detectors. I am grateful to Prof. Kyoichiro Ozawa for his continuous encouragement, his broad perspective on the experiment, and for engaging with my immature physics discussions with great patience.

I would like to thank Dr. Hiroyuki Sako for welcoming me into the Hadron Group at JAEA from the second year of my master's program to the present. His support allowed me to conduct my research close to the experimental site. I also thank Dr. Hideto En'yo for his sharp and essential questions and advice during meetings, as well as for teaching me the mindset required for conducting research and experiments. Although I had only limited opportunities to interact with Prof. Wen-Chen Chang, I am sincerely grateful for the valuable discussions we had, especially regarding the physics accessible at the high momentum beamline, nucleon structure, and so on. Despite my poor English, he kindly answered my many questions.

The data used in this study were collected at the high momentum beamline newly constructed at J PARC in 2020. I am grateful to the MR staff and the HD beam group for their tremendous efforts in providing a stable beam and tuning it for the E16 experiment. I also thank the beam groups at KEK PFAR and the staff at Tohoku University ELPH for their support during the detector performance tests.

The evaluation of the production cross sections in this study was made possible through the contributions of many people. In particular, I would like to thank Dr. Tomoki Murakami, Mr. Shunnosuke Nagafusa, and Mr. Rento Yamada for performing evaluations directly connected to the results of this thesis. Their analyses were indispensable for completing this work. I am also grateful to Dr. Koki Kanno and Ms. Sakiko Ashikaga for completing the development of the electron identification detectors capable of operating in a high-rate environment, and for their extensive support until I became able to operate them myself. My sincere thanks go to

Dr. Tomonori Takahashi, Mr. Wataru Nakai, Dr. Masaya Ichikawa, and Dr. Ren Ejima for their essential development and support of the detectors, electronics, and DAQ systems used in this study. I also acknowledge the foundational developments by Dr. Kazuki Suzuki, Mr. Ryohei Fujii, Mr. Yudai Takaura, Mr. Takehito Kondo, Mr. Daichi Arimizu, Ms. Kanako Yamaguchi, Mr. Shuta Ochiai, Mr. Jo Kakunaga, Mr. Shunji Hashimoto, and Mr. Shogo Yanai, which formed the basis of this research. Beyond research, their presence made my life in Tokai mura enjoyable.

I would like to thank all members of the Experimental Nuclear Hadron Laboratory at Kyoto University. I am grateful to Prof. Tomofumi Nagae, Prof. Kimiko Sekiguchi, Prof. Juzo Zenihiro, Prof. Toshiyuki Gogami, Prof. Masanori Dozono, and Prof. Natsuki Tomida for their advice based on their broad expertise across various research fields. In particular, I had many fruitful discussions with Prof. Natsuki Tomida regarding the physics programs at the high momentum beamline. Although my stay in Kyoto was short, I am thankful to everyone for always welcoming me warmly.

I would like to express my gratitude to Ms. Yuri Kimura, Ms. Midori Kaji, and Ms. Mitsue Yamamoto, who supported my research activities from the administrative side.

Finally, I am deeply grateful to my family, who have allowed me to follow my own path and supported me throughout.

Bibliography

[1] W. Weise. In: *Nuclear Physics A* 553 (Mar. 1, 1993), pp. 59–72. DOI: 10.1016/0375-9474(93)90615-5.

[2] P. Koch et al. In: *Z. Physik A - Atomic Nuclei* 324.4 (Dec. 1, 1986), pp. 453–463. DOI: 10.1007/BF01290929.

[3] The NA49 Collaboration et al. In: *Phys. Rev. C* 66.5 (Nov. 27, 2002), p. 054902. DOI: 10.1103/PhysRevC.66.054902.

[4] NA49 Collaboration et al. In: *Phys. Rev. C* 77.2 (Feb. 19, 2008), p. 024903. DOI: 10.1103/PhysRevC.77.024903.

[5] HADES Collaboration et al. In: *Phys. Rev. C* 80.2 (Aug. 26, 2009), p. 025209. DOI: 10.1103/PhysRevC.80.025209.

[6] W. Y. for the STAR Collaboration. Quark Matter 2025. Accessed: 2025-02-11. 2025.

[7] NA49 Collaboration et al. In: *Phys. Rev. C* 78.4 (Oct. 27, 2008), p. 044907. DOI: 10.1103/PhysRevC.78.044907.

[8] A. Aduszkiewicz et al. In: *Eur. Phys. J. C* 80.3 (Mar. 3, 2020), p. 199. DOI: 10.1140/epjc/s10052-020-7675-6.

[9] Ł. Rozpłochowski. In: *EPJ Web Conf.* 316 (2025), p. 05003. DOI: 10.1051/epjconf/202531605003.

[10] A. Palmese et al. In: *Phys. Rev. C* 94.4 (Oct. 24, 2016), p. 044912. DOI: 10.1103/PhysRevC.94.044912.

[11] M. Hartmann et al. In: *Phys. Rev. C* 85.3 (Mar. 19, 2012), p. 035206. DOI: 10.1103/PhysRevC.85.035206.

[12] J. Adamczewski-Musch et al. In: *Phys. Rev. Lett.* 123.2 (July 9, 2019), p. 022002. DOI: 10.1103/PhysRevLett.123.022002.

[13] ALICE Collaboration et al. In: *Phys. Rev. Lett.* 127.17 (Oct. 20, 2021), p. 172301. DOI: 10.1103/PhysRevLett.127.172301.

[14] Y. Nara et al. In: *Phys. Rev. C* 61.2 (Dec. 22, 1999), p. 024901. DOI: 10.1103/PhysRevC.61.024901.

[15] S. Navas et al. In: *Phys. Rev. D* 110.3 (Aug. 1, 2024), p. 030001. DOI: 10.1103/PhysRevD.110.030001.

[16] PACS-CS Collaboration et al. In: *Phys. Rev. D* 79.3 (Feb. 5, 2009), p. 034503. DOI: 10.1103/PhysRevD.79.034503.

[17] G. S. Bali. In: *Physics Reports* 343.1 (Mar. 1, 2001), pp. 1–136. DOI: 10.1016/S0370-1573(00)00079-X.

[18] B. Andersson et al. In: *Physics Reports* 97.2 (July 1, 1983), pp. 31–145. DOI: 10.1016/0370-1573(83)90080-7.

[19] J. Geiss et al. In: *Nuclear Physics A* 644.1 (Dec. 14, 1998), pp. 107–138. DOI: 10.1016/S0375-9474(98)80011-0.

[20] PHENIX Collaboration et al. In: *Phys. Rev. D* 76.5 (Sept. 25, 2007), p. 051106. DOI: 10.1103/PhysRevD.76.051106.

[21] T. Sjöstrand. In: *Computer Physics Communications* 82.1 (Aug. 1, 1994), pp. 74–89. DOI: 10.1016/0010-4655(94)90132-5.

[22] G. Stefanek et al. In: *Proceedings of 10th International Conference on Quarks and Nuclear Physics — PoS(QNP2024)*. Vol. 465. SISSA Medialab, Mar. 25, 2025, p. 128. DOI: 10.22323/1.465.0128.

[23] L. Kluberg et al. In: *Phys. Rev. Lett.* 38.13 (Mar. 28, 1977), pp. 670–673. DOI: 10.1103/PhysRevLett.38.670.

[24] T. Ishikawa et al. In: *Physics Letters B* 608.3 (Feb. 24, 2005), pp. 215–222. DOI: 10.1016/j.physletb.2005.01.023.

[25] CLAS Collaboration et al. In: *Phys. Rev. C* 78.1 (July 8, 2008), p. 015201. DOI: 10.1103/PhysRevC.78.015201.

[26] J. Steinheimer et al. In: *J. Phys. G: Nucl. Part. Phys.* 43.1 (Feb. 2015), p. 015104. DOI: 10.1088/0954-3899/43/1/015104.

[27] T. Song et al. In: *Phys. Rev. C* 106.2 (Aug. 19, 2022), p. 024903. DOI: 10.1103/PhysRevC.106.024903.

[28] T. Hatsuda et al. In: *Phys. Rev. C* 46.1 (July 1, 1992), R34–R38. DOI: 10.1103/PhysRevC.46.R34.

[29] P. Gubler et al. In: *Phys. Rev. D* 90.9 (Nov. 4, 2014), p. 094002. DOI: 10.1103/PhysRevD.90.094002.

[30] KEK-PS E325 Collaboration et al. In: *Phys. Rev. Lett.* 98.4 (Jan. 23, 2007), p. 042501. DOI: 10.1103/PhysRevLett.98.042501.

[31] K. Aoki et al. In: *Journal of Subatomic Particles and Cosmology* 3 (June 1, 2025), p. 100019. DOI: 10.1016/j.jspc.2024.100019.

[32] I. W. Park et al. In: *Phys. Rev. D* 107.7 (Apr. 24, 2023), p. 074033. DOI: 10.1103/PhysRevD.107.074033.

[33] H. Kim et al. In: *Physics Letters B* 805 (June 10, 2020), p. 135412. DOI: 10.1016/j.physletb.2020.135412.

[34] Y. Ichikawa et al. In: *Journal of Subatomic Particles and Cosmology* 3 (June 1, 2025), p. 100040. DOI: 10.1016/j.jspc.2025.100040.

[35] H. Ohnishi et al. In: *Progress in Particle and Nuclear Physics* 113 (July 1, 2020), p. 103773. DOI: 10.1016/j.ppnp.2020.103773.

[36] J. Hudis et al. In: *Phys. Rev.* 129.1 (Jan. 1, 1963), pp. 434–437. DOI: 10.1103/PhysRev.129.434.

[37] J. B. Cumming et al. In: *Nuclear Instruments and Methods* 180.1 (Feb. 15, 1981), pp. 37–44. DOI: 10.1016/0029-554X(81)90007-0.

[38] E. Hirose et al. In: 32.6 (Sept. 2022), pp. 1–4. DOI: 10.1109/TASC.2022.3168525.

[39] https://www.3ds.com/products/simulia/opera.

[40] F. Sauli. In: *Nuclear Instruments and Methods in Physics Research Section A: Accelerators, Spectrometers, Detectors and Associated Equipment* 386.2 (Feb. 21, 1997), pp. 531–534. DOI: 10.1016/S0168-9002(96)01172-2.

[41] T. N. Murakami et al. In: *Nucl. Instrum. Methods A* 1058 (Jan. 1, 2024), p. 168817. DOI: 10.1016/j.nima.2023.168817.

[42] T. Takahashi et al. In: 68.8 (Aug. 2021), pp. 1907–1911. DOI: 10.1109/TNS.2021.3087635.

[43] Y. Giomataris et al. In: *Nuclear Instruments and Methods in Physics Research Section A: Accelerators, Spectrometers, Detectors and Associated Equipment* 310.3 (Dec. 15, 1991), pp. 589–595. DOI: 10.1016/0168-9002(91)91104-4.

[44] W. Anderson et al. In: *Nucl. Instrum. Methods A* 646.1 (Aug. 1, 2011), pp. 35–58. DOI: 10.1016/j.nima.2011.04.015.

[45] S. Nakasuga et al. In: *Nucl. Instrum. Methods A* 1082 (Feb. 1, 2026), p. 170956. DOI: 10.1016/j.nima.2025.170956.

[46] S. Kawabata et al. In: *Nuclear Instruments and Methods in Physics Research Section A: Accelerators, Spectrometers, Detectors and Associated Equipment* 270.1 (July 1, 1988), pp. 11–20. DOI: 10.1016/0168-9002(88)90004-6.

[47] S. Ashikaga. Master's thesis, in Japanese. 2018.

[48] https://www.sitcp.net/materials.html.

[49] M. Ichikawa et al. In: 66.8 (Aug. 2019), pp. 2022–2027. DOI: 10.1109/TNS.2019.2928561.

[50] K. Kanno et al. In: *Nucl. Instrum. Methods A* 819 (May 21, 2016), pp. 20–24. DOI: 10.1016/j.nima.2016.02.063.

[51] R. Yamada. Master's thesis. 2025.

[52] https://openit.kek.jp/project/HUL/public/hul/HUL.

[53] T. Tabaru et al. In: *Phys. Rev. C* 74.2 (Aug. 2, 2006), p. 025201. DOI: 10.1103/PhysRevC.74.025201.

[54] R. Arnaldi et al. In: *Eur. Phys. J. C* 79.5 (May 25, 2019), p. 443. DOI: 10.1140/epjc/s10052-019-6848-7.

[55] V. Blobel et al. In: *Physics Letters B* 59.1 (Oct. 13, 1975), pp. 88–92. DOI: 10.1016/0370-2693(75)90164-1.

[56] X.-N. Wang et al. In: *Phys. Rev. D* 44.11 (Dec. 1, 1991), pp. 3501–3516. DOI: 10.1103/PhysRevD.44.3501.

[57] W. Cassing et al. In: *Phys. Rev. C* 78.3 (Sept. 29, 2008), p. 034919. DOI: 10.1103/PhysRevC.78.034919.

[58] W. Cassing et al. In: *Nuclear Physics A* 831.3 (Dec. 15, 2009), pp. 215–242. DOI: 10.1016/j.nuclphysa.2009.09.007.

[59] M. Ichikawa et al. In: *Prog Theor Exp Phys* 2025.9 (Sept. 1, 2025), p. 093D01. DOI: 10.1093/ptep/ptaf108.